Ph.D. Dissertation

Atmospheric-Boundary-Layer Height Retrieval using Microwave Radiometer and Lidar Sensors: Algorithms and Error Estimation

A thesis submitted to the Universitat Politècnica de Catalunya
in partial fulfillment for the degree of

Doctor of Philosophy

Umar Saeed

UNIVERSITAT POLITÈCNICA
DE CATALUNYA
BARCELONATECH

Remote Sensing Laboratory
Department of Signal Theory and Communications

Doctorate program in
Signal Theory and Communications

Supervisors: Prof. Francesc Rocadenbosch Burillo
Prof. Susanne Crewell

Barcelona, June 2016

Curs acadèmic: 2015-2016

Acta de qualificació de tesi doctoral

Nom i cognoms **Umar SAEED**

Programa de doctorat **TEORIA DEL SENYAL I COMUNICACIONS**

Unitat estructural responsable del programa **DEP. TEORIA DEL SENYAL I COMUNICACIONS**

Resolució del Tribunal

Reunit el Tribunal designat a l'efecte, el doctorand / la doctoranda exposa el tema de la seva tesi doctoral titulada **Atmospheric-Boundary-Layer Height Retrieval using Microwave Radiometer and Lidar Sensors: Algorithms and Error Estimation.**

Acabada la lectura i després de donar resposta a les qüestions formulades pels membres titulars del tribunal, aquest atorga la qualificació:

☐ NO APTE ☐ APROVAT ☐ NOTABLE ☐ EXCEL·LENT

(Nom, cognoms i signatura) President/a	(Nom, cognoms i signatura) Secretari/ària

(Nom, cognoms i signatura) Vocal	(Nom, cognoms i signatura) Vocal	(Nom, cognoms i signatura) Vocal

______________________, _______ d'/de __________________ de _______________

El resultat de l'escrutini dels vots emesos pels membres titulars del tribunal, efectuat per l'Escola de Doctorat, a instància de la Comissió de Doctorat de la UPC, atorga la MENCIÓ CUM LAUDE:

☐ SÍ ☐ NO

(Nom, cognoms i signatura) President de la Comissió Permanent de l'Escola de Doctorat	(Nom, cognoms i signatura) Secretari de la Comissió Permanent de l'Escola de Doctorat

Barcelona, _______ d'/de ____________________ de _________

Atmospheric-Boundary-Layer Height Retrieval using Microwave Radiometer and Lidar Sensors: Algorithms and Error Estimation

[a] Remote Sensing Laboratory
Dept. of Signal Theory and Communications (TSC)
Universitat Politècnica de Catalunya (UPC)
08034 Barcelona, Spain

[b] Institute for Geophysics and Meteorology (IGMK)
University of Cologne
50969 Köln, Germany

Dedicated to my beautiful family...

Acknowledgments

The following institutions are gratefully acknowledged for their contribution to this work:

- *European Union*, Seventh Framework Programme (FP7/2007-2013): People, ITN Marie Curie Actions Programme (2012-2016) in the frame of ITARS project under grant agreement no. 289923.
- *Institute for Geophysics and Meteorology (IGMK)*, Department of Geoscience, University of Cologne, for hosting the author for several research stays carried-out during his Ph.D.
- *Federal Ministry of Education and Research in Germany (BMBF)* for financing the HOPE campaign through the research programme High Definition Clouds and Precipitation for Climate Prediction HD(CP)^2.
- *Generalitat de Catalunya*, (Grup de Recerca Consolidat), 2014-SGR-583.
- *EU COST Action* ES1303 TOPROF for supporting a Short Term Scientific Mission (STSM) at the University of Cologne during 21-25 March, 2016.

First of all, all credits goes to my parents, without whom I would not have been writing these lines. My mother, a pillar of strength, perseverance, and determination is, and will always be a cornerstone and inspiration of my life. She is my first teacher of life, and academics. My father who showed vision, courage, and strength at the cross-roads of life and endured tough choices. He instilled a sense of self-discipline and responsibility in my life. I also acknowledge my sisters for always being a source of cheer and joy during the testing times of my life.

My special gratitude and apologies to my wife and son for tolerating my frequent absences due to work-related travels and deadlines. They have given a new meaning and color to my life.

My sincere thanks to my Ph.D. adviser Prof. Francesc Rocadenbosch for providing continuous support, guidance, and motivation throughout the duration of this Ph.D. His role has been instrumental at every stage of this Ph.D. thesis to keep me focused and productive.

I fully acknowledge the co-adviser of my Ph.D., Prof. Susanne Crewell from the University of Cologne, for providing sound technical guidance on atmospheric and meteorology related aspects of this thesis. She hosted me on several secondments in her research group, which broadened my scientific knowledge and research skills. She has always been welcoming and accessible despite her busy schedules. My sincere gratitude to Dr. Ulrich Löhnert for his help and guidance on microwave radiometry, to Dr. Jan Schween and Dr. Anne Hirsikko for their help on ceilometers, and Dr. Thijs Heus and Prof. Roel Neggers for providing the Large Eddy Simulation data.

I am also thankful to Dr. Jordi Tiana and Dr. Diego Lange for their help and guidance on lidar and Kalman filter. Special thanks to Dr. Dave Turner from National Severe Storms Laboratory, NOAA for his insightful discussions and ideas on microwave radiometry and boundary-layer physics.

Finally, I would like to thank the ITARS network for providing an excellent platform and resources for doing science and organizing several networking events, and to everybody who have contributed directly and indirectly to this Ph.D.

Barcelona, June 2016

Umar Saeed

Abstract

The Atmospheric Boundary Layer Height (ABLH) is an important parameter in weather forecasting, meteorology, avionics, and air-quality and dispersion models. Local development of the Atmospheric Boundary Layer (ABL) over the full diurnal cycle is a function of several parameters which, among others, include geographical location of the place, its topography, time of the year, and day and night conditions. There are several remote sensing instruments and methods to retrieve the ABLH, however, none of these can fully measure ABL development under all atmospheric conditions.

This Ph.D. thesis deals with estimation of the ABLH over the full diurnal cycle, which includes day-time mixing layer, nocturnal stable boundary layer, and morning/evening transition boundary layer, by using ground-based microwave-radiometer (MWR) and ceilometer (lidar principle) remote-sensing instruments as well as related signal processing techniques. ABLH estimates from Doppler lidar and radiosondes are used as references. An aim of this thesis is also to combine data from these two instruments, thus, exploiting their individual strengths and overcoming their limitations. In this context, this thesis has been structured around three main goals:

First, a synergetic method for estimation of the Mixing Layer Height (MLH) is presented. Towards this end, uncertainties in the MLH derived from backscattered ceilometer signals and MWR-retrieved potential temperature profiles are analysed and compared. While the Extended Kalman Filter (EKF) is used as adaptive filter to process backscattered lidar signals from the ceilometer, the parcel method is used with the MWR-retrieved potential temperature profile. Finally, the two methods are combined into a new methodology for synergetic MLH retrieval.

Second, methods for the estimation of the nocturnal Stable-Boundary-Layer Height (SBLH) from ceilometer and MWR data, in stand-alone and in synergetic fashion, are investigated. The SBLH from backscattered ceilometer signals is retrieved by using Minimum Variance Regions (MVRs) as signatures of aerosol stratification in the SBL. For the MWR, idealized physical models from the literature are used to estimate the SBLH. Next, a synergetic SBLH retrieval method is developed, which combines measurement data from both instruments.

Finally, a preliminary study on the feasibility of Large Eddy Simulation (LES) as a tool for understanding the ABL is presented. To this end, LES-simulated lidar backscatter and potential temperature profiles are compared against instrumental measurements. In addition, a new method for direct retrieval of the MLH from LES-simulated brightness temperature measurements is presented, hence, alleviating the need for physical temperature retrieval first. The impact of retrieval errors on MLH estimates is also investigated.

The techniques developed in this Ph.D. have been tested on the data from HOPE measurement campaign (Jülich, Germany), where different test cases under different atmospheric conditions have been considered.

Contents

List of Figures

List of Tables

List of Symbols

T_B Brightness Temperature [K]. 14

α Total extinction [m^{-1}]. 18

β Total backscatter [$\mathrm{m}^{-1}\mathrm{sr}^{-1}$]. 19

β_{mol} Molecular backscatter [$\mathrm{m}^{-1}\mathrm{sr}^{-1}$]. 19, 42

β_{aer} Aerosol backscatter [$\mathrm{m}^{-1}\mathrm{sr}^{-1}$]. 19, 42

I_ν Spectral Radiance $[W \cdot \mathrm{m}^{-2} \cdot \mathrm{sr}^{-1} \cdot Hz^{-1}]$. 21

h Plank's Constant $6.34 \times 10^{-34} [J \cdot s]$. 21

k_B Boltzmann Constant $1.38 \times 10^{-23} [J \cdot K^{-1}]$. 21

c Speed of Light $3 \times 10^8 [m \cdot s^{-1}]$. 21

$T_{incident}$ Incident Antenna Temperature [K]. 35

T_{AP} Apparent Temperature [K]. 35

T_A Antenna Temperature [K]. 37

Δz_{T_b} Error on MLH due to brightness temperature measurements errors. 50, 51, 55–57

Δz_{res} Error on MLH due to low vertical resolution of the retrieved temperature. 50, 51, 55–57

z_{MLH} Mixing Layer Height. 52, 112, 113

θ Atmospheric potential temperature [K]. 53

σ Standard deviation. 72

List of Acronyms

ITARS Initial Training for Atmospheric Remote Sensing. 1–3, 12

EU European Union. 1

ABLH Atmospheric Boundary Layer Height. 3, 6, 13–15, 32, 39–44, 46–48, 85, 89, 109, 110, 121

ABL Atmospheric Boundary Layer. 3–6, 10, 12, 13, 15, 31, 38–43, 47, 66, 70, 71, 75, 91, 109, 110, 121

FT Free Troposphere. 3, 6, 38, 40–43, 47, 52, 59, 75, 110, 113, 119

WV Water Vapor. 3, 9, 14, 21, 22, 25–27, 29, 31, 33

MWR MicroWave Radiometer. 3–8, 10, 12–14, 21, 23, 29, 31–33, 44, 46–51, 53, 55–57, 59, 60, 62, 64–67, 73, 84–88, 90, 91, 100, 103, 104, 108, 112, 115, 117, 119–121

RS Radiosonde. 3, 7, 10, 31, 48, 60, 82, 119, 120

UPC Universitat Politécnica de Catalunya. 3

UCOL University of Cologne. 3, 4, 6, 7, 26

EKF Extended Kalman Filter. 4, 5, 12, 40, 42, 43, 49, 50, 52–54, 60, 62, 65–67, 72, 84, 86–88, 90, 91, 93, 95, 99, 104, 105, 108, 119–121

JOYCE Jülich ObservatorY for Cloud Evolution. 4, 7, 8, 11

RPG Radiometer Physics GmbH. 4–8, 10, 32, 33, 57, 66

HATPRO Humidity and Temperature Profilers. 4, 5, 7, 8, 10, 32, 33, 51, 56, 57, 66, 104, 120

MLH Mixing Layer Height. 4–6, 8, 11, 12, 32, 40, 42–44, 49–57, 59, 60, 62, 64–67, 91, 95, 111–113, 115, 117, 119–121

SBLH Stable Boundary Layer Height. 4, 5, 12, 14, 44, 46, 48, 72, 73, 75, 77, 80–84, 86–91, 93, 95, 104, 105, 107, 108, 120

LES Large Eddy Simulation. 4–6, 12, 57, 109–111, 113–115, 117, 121

HOPE HD(CP)^2 Observational Prototype Experiment. 5, 6, 11, 57, 66, 67, 73, 84–87, 89, 95, 105, 106, 108, 117, 120

SBL Stable Boundary Layer. 5, 38, 46, 64, 69–73, 75, 76, 79, 80, 83–88, 91, 95, 97, 98, 100, 104, 106–110, 120

MVR Minimum Variance Region. 5, 12, 70, 72, 74, 75, 77, 79–84, 87, 88, 90, 91, 95, 98, 108, 120

RTM Radiative Transfer Model. 6, 12, 14, 23, 25, 26, 29, 48

OEM Optimal Estimation Method. 6, 31, 111, 112, 114

DoF Degrees of Freedom. 10, 32, 51, 55, 56, 66, 112, 113, 117

RH Relative Humidity. 10, 26, 110

ML Mixing Layer. 14, 32, 38, 40, 42–44, 47, 52, 59, 60, 62, 64, 65, 67, 69, 71, 75, 76, 79–82, 91, 110, 113, 119

EM ElectroMagnetic. 14, 21

IWV Integrated Water Vapor. 14, 32

IPW Integrated Precipitable Water. 14

APD Avalanche Photo-Diode. 17

PMT Photo-Multiplier Tube. 17

LW Liquid Water. 22

FWD Forward. 26

pdf Probability Density Function. 31

LWC Liquid Water Content. 31

KF Kalman filter. 32, 42, 52

superhet SuperHetrodyne. 33

CBL Convective Boundary Layer. 38, 90, 109

EZ Entrainment Zone. 38, 40, 42, 43, 65, 70, 71, 75, 76, 79, 90, 112, 113, 117

RL Residual Layer. 39, 46, 59, 60, 62, 64, 66, 67, 71–73, 75, 76, 81, 82, 86, 87, 100, 110

MA Moving Average. 42, 74, 75, 77–79, 84

SNR Signal-to-Noise Ratio. 42, 52, 74, 91

mMSE Minimum Mean-Square Error. 45, 86–88, 120

RMSE Root-Mean-Square Error. 46, 60, 67, 84, 87

NBL Nocturnal Boundary Layer. 69, 70

CI Capping Inversion. 70, 71, 76

NLSQ Non-linear Least SQuares. 72, 93, 104, 120, 121

PSD Power Spectral Density. 75, 77, 78

LSQ Least SQuares. 86, 88

CBLH Convective Boundary Layer Height. 89

DALES Dutch Atmospheric Large-Eddy Simulation. 109, 111, 113

Chapter 1

Introduction

This chapter gives an overview of the ITARS project, which is the framework topic of this Ph.D. thesis and its mobility context, and the main Ph.D. objectives. This chapter is complemented with a summary of the remote sensing instrumentation used.

1.1 The ITARS network

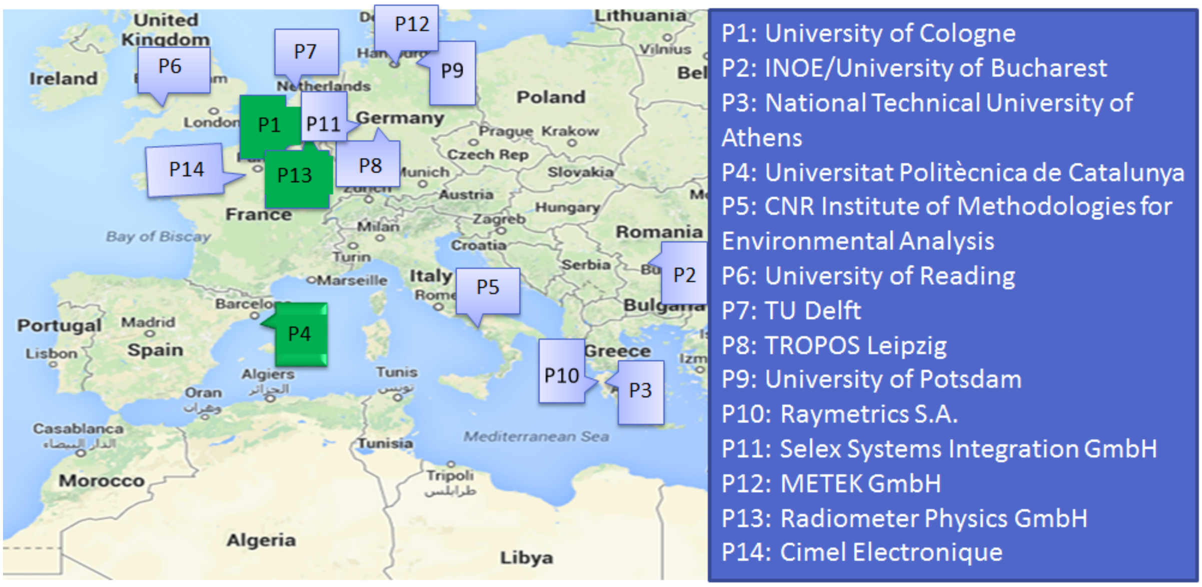

Figure 1.1: The organizational structure of the ITARS research and training programme [ITARS proposal, 2012].

This Ph.D. thesis is a part of the Initial Training for Atmospheric Remote Sensing (ITARS)[1], a Marie Curie - Initial Training Network (ITN), under the 7th Framework Programme (FP7) for Research and Technological Development of the European Union (EU),

---

[1] `http://itars.uni-koeln.de/`

for the training of the Early Stage Researchers (ESRs). The network is comprised of 9 degree awarding research institutes and 5 private-sector associated partners, which are Small and Medium Enterprises (SMEs), in 8 European countries (Fig. 1.1). 11 ESRs for 36-months and 4 experienced researchers (ER) for 24-months were hired to pursue the doctorate and post-doctorate degrees, respectively *Banks et al.* [2016].

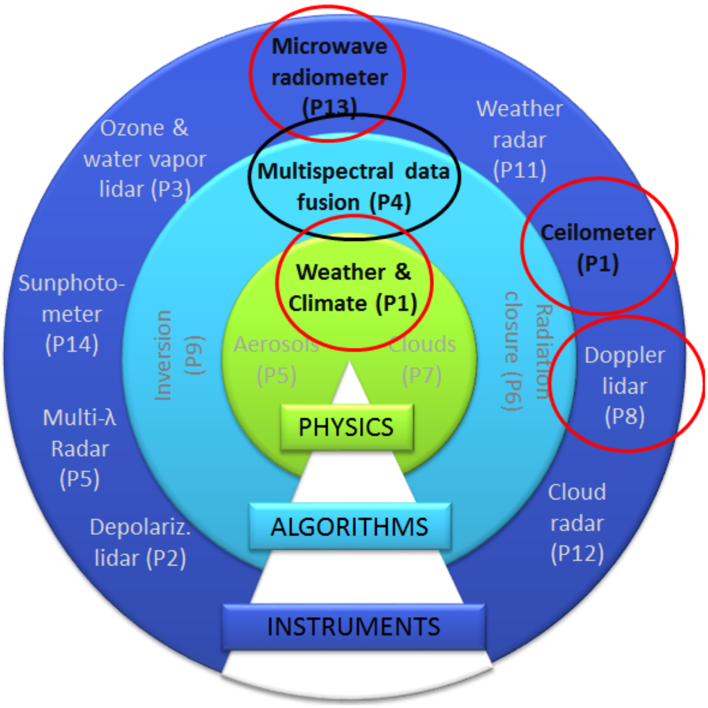

Figure 1.2: The scientific structure of the ITARS with individual research fields and tools [ITARS proposal, 2012]. Topics of relevance to this Ph.D. thesis are encircled in red color.

As mentioned in the ITARS proposal, it is aimed to focus on the synergistic application of high-end ground-based remote-sensing instruments, which have potential to substantially contribute to the improved understanding of aerosols, clouds, aerosol-cloud interaction processes, and their role for both climate and weather. The main areas of research in ITARS are shown in Fig. 1.2, with *aerosols*, *climate and weather*, and *clouds* sharing common grounds with *instruments*, *algorithms*, and *physics*. In order to exploit the full information content of measurements, and convert the measured properties, e.g., multi-wavelength radiances, backscattered signals, and polarimetric quantities to atmospheric parameters, detailed knowledge on the algorithms and instruments is necessary.

Within ITARS, each ESR was supervised by a *supervision team*, which consisted of a primary adviser from the host institute, a co-adviser preferably from another ITARS partner, and a third member suggested by the fellow. The training plan of ITARS for each ESR comprised of an individual *Career Development Plan* (CDP) with *individual* and *network* training components. The individual training component of the CDP consisted of individual research topic, courses at the host institution, secondments at private sector and other research institutes in ITARS, and other complimentary training elements such as the project management, local languages etc. The network training component of the CDP, common for all ITARS fellows, comprised of e-seminars and tutorials, and summer schools along with complementary elements such as courses on communication skills, entrepreneurship, ethics and IPR, and outreach.

1.2 Ph.D. topic

Continuous estimates of the Atmospheric Boundary Layer Height (ABLH) are needed for several applications ranging from weather, avionics, and air-quality and dispersion models. The Atmospheric Boundary Layer (ABL) is the lowest part of the troposphere which is directly affected by the Earth surface on a scale of an hour or less *Stull* [1988]. It is the part of the troposphere which is responsible for exchange of heat, momentum, and aerosols between the Earth surface and the Free Troposphere (FT). The ABLH is a key atmospheric parameter and is directly linked with its behaviour and development, and it can be determined by the signature within the profiles of temperature, potential temperature, virtual potential temperature, Water Vapor (WV), aerosols, wind, and other trace gases *Emeis* [2010]. Different kinds of instruments have been used for the study of atmosphere in the tropospheric region which include radar, sodar, MicroWave Radiometer (MWR), lidar, *in situ* instruments such as weather balloon, Radiosonde (RS), and even aircrafts. The ground-based remote-sensing instruments offer continuous availability, better spatial and temporal resolution, and low cost solution.

This Ph.D. thesis is aimed at the development of signal processing methods to retrieve the ABLH from stand-alone as well as synergetic observations from ground-based lidar and MWR instruments.

The Ph.D. work includes several aspects of these instruments, their interaction with the atmosphere, the retrieval of the atmospheric parameters of interest from measured signals, and related error uncertainties. The thesis has been supervised by the Universitat Politécnica de Catalunya (UPC)[1] (Remote Sensing Lab., Dep. of Signal Theory and Communications)[2] and the University of Cologne (UCOL)[3] (Institute for Geophysics and Meteorology)[4], UPC focusing more on the signal processing/lidar side and UCOL on the physical/MWR one.

On the signal-processing side, much work has been done by the earlier Ph.D. students *Reba* [2010]; *Kumar* [2012]; *Lange* [2014], advised by Dr. Rocadenbosch at UPC. The simulator for the retrieval of opto-atmospheric parameters using the backscattered signal from the UPC multi-spectral lidar system, contains comprehensive set of scenarios for the aerosol

---

[1] `http://www.tsc.upc.edu`

[2] `http://www.tsc.upc.edu/rslab/`

[3] `http://www.portal.uni-koeln.de/uoc_home.html?&L=1`

[4] `http://www.geomet.uni-koeln.de/en/general/home/`

profiles, and retrieval algorithms. An Extended Kalman Filter (EKF)-based algorithm for the continuous tracking of the ABL using the lidar return signal, has also been successfully implemented *Lange et al.* [2014]. These expertise and resources will be extremely helpful for the goals of this Ph.D.

On the MWR side, measurement data and expertise from the group of Prof. Susanne Crewell at the UCOL will be utilized. The Jülich super-site called Jülich ObservatorY for Cloud Evolution (JOYCE)[1] linked to the UCOL operates Radiometer Physics GmbH (RPG) Humidity and Temperature Profilers (HATPRO) *Rose et al.* [2005] as well as ceilometers and other instruments. The data is available on the UCOL servers and will be utilized for the lidar and MWR related algorithms.

A note on terminology: The term "lidar" refers to general purpose laser-radar systems, including advanced multi-spectral elastic/Raman systems for tropospheric profiling while "ceilometer" refers to a low-power, low-cost, single-wavelength lidar. In this Ph.D., ceilometers are used as far as lidar instruments are concerned (see Sect. 1.5 for a detailed description of the remote sensing instruments involved). In spite of the fact that in this Ph.D. only ceilometers are used for the lidar part, the term "lidar" will be used for the concepts and theory related to optical remote sensing of atmosphere, while the term "ceilometer" will be used in the context of the instrument itself and related backscatter signal processing.

1.3 Ph.D. objectives

1. *Development of a synergetic method for Mixing Layer Height (MLH) estimation from combined lidar and MWR measurements.* This objective involves evaluation of the associated uncertainties.

2. *Development of algorithms for Stable Boundary Layer Height (SBLH) estimation from lidar and MWR measurements, either non-synergetic or synergetic.* This objective has been divided into two sub-objectives:

    (a) Non-synergetic SBLH estimation.

    (b) Synergetic SBLH estimation.

3. *Feasibility study on the usage of Large Eddy Simulation (LES) data for MLH estimation.*

---

[1] `http://www.geomet.uni-koeln.de/en/general/research/joyce/`

1.3.1 Obj. 1: Development of a synergetic method for MLH estimation from combined lidar and MWR measurements

MLH retrieval methods using backscattered lidar signals and MWR-retrieved potential-temperature profiles are to be compared in terms of their capabilities and associated uncertainties. The EKF will be used for MLH retrieval from backscattered lidar signals and the parcel method for MLH retrieval from MWR-retrieved potential-temperature profiles. Measurement and retrieval errors are to be revisited and incorporated into the MLH estimation methods used. Uncertainties on MLH estimates from the two methods will be compared along with a combined MLH-retrieval discussion case. Measurement data from a Jenoptik CHM 15k Nimbus ceilometer and a RPG HATPRO MWR collected during the HD(CP)^2 Observational Prototype Experiment (HOPE) campaign will be used.

1.3.2 Obj. 2: Development of algorithms for SBLH estimation from lidar and MWR data

1.3.2.1 Obj. 2a: Non-synergetic SBLH estimation

Stable Boundary Layer (SBL) is one of the least understood topics and still a matter of research in the field of meteorology and weather forecast. In this sub-objective, first a review of the behaviour of aerosols and physical temperature in the atmosphere under stable conditions will be presented. In this context, backscatter lidar returns are to be analysed with a view to identify signatures for aerosol stratification. Minimum Variance Regions (MVRs) in the backscatter lidar signal will be considered for SBLH estimation. SBLH estimation from MWR-retrieved potential temperature profiles will also be considered under different idealized physical models from the literature to estimate the SBLH.

1.3.2.2 Obj. 2b: Synergetic SBLH estimation

A synergetic approach for estimation of the nocturnal SBLH will be presented. Aerosol backscatter from a lidar-ceilometer and potential temperature from a MWR are to be combined by adaptive signal processing methods, such as the EKF. The method will be applied to data from a Vaisala CT25K ceilometer and a HATPRO MWR collected during the HOPE campaign.

1.3.3 Obj. 3: Feasibility study on the usage of LES data for MLH estimation

In this objective, LES model will be introduced as a tool for understanding the ABL. Thus, LES-simulated data is to be cross-compared with instrumental measurements. As a test case, a method for MLH retrieval directly from simulated brightness measurements will be presented. Towards this end, the algorithm is to compare "truth" brightness temperatures and LES-simulated data, to algorithm-generated ones, obtained via parametrized temperature profile and a Radiative Transfer Model (RTM), by using an Optimal Estimation Method (OEM).

1.4 Ph.D. mobility context

The University of Cologne is one of the largest universities in Germany. The Institute for Geophysics and Meteorology (IGMK) which is part of the Department of Geoscience, one of the six departments under the Faculty of Mathematics and Natural Sciences, combines research groups from applied geophysics, space physics, turbulence atmospheric modelling, and integrated remote sensing, among others.

The RPG which was founded in 1991 as a private company, and is now a subsidery of Rohde & Schwarz GmbH, is one of the leading suppliers of remote sensing, millimeter wave, sub-mm and THz instrumentation and components.

During this 3-year Ph.D., six secondments were completed, five at IGMK (UCOL) and one at RPG. Various aspects of microwave radiometry and ceilometer data processing, especially, ABL physics and meteorology, retrieval of ABLH, RTM, and instrument functioning were learned during these secondments. In the following a summary of each visit is given:

- 17 April - 27 April 2013: During this secondment at UCOL, familiarization with the format and structure of netcdf data files associated to lidar and MWR measurement data at UCOL was made. Moreover, study and implementation of the ABLH estimation methods such as the parcel method and Bulk Richardson number method by using the MWR-retrieved temperature data was done.

- 29 July - 31 August 2013: In this one month-long secondment at UCOL, sensitivity analysis of MWR brightness temperature to the ABLH, FT temperature gradient, and surface temperature was carried out. Forward modelling was used to simulate brightness temperatures of at different frequencies and elevation angles.

- 09 March - 15 March 2014: The goals defined for this short visit to UCOL included learning the operational method for temperature retrieval using MWR data, calculation of temperature weighting functions, to get acquainted with Jenoptik and Vaisala ceilometer data and its pre-processing, and to identify suitable case-study days from HOPE campaign.

- 07 August - 02 September 2015: This one month-long secondment was split between UCOL and RPG. At UCOL, work on the LES data was started and a comparative analysis based on different approaches for the ABLH estimation was initiated.

The two weeks training at RPG included introduction to the HATPRO MWR hardware, retrieval software, and state-of-the-art practices in the MWR industry.

- 20 March - 25 March 2016: This secondment to UCOL was completed under the framework of COST Action Short Term Scientific Mission (STSM) titled "A physical retrieval of mixing-layer height using simulated brightness temperature measurements".

1.5 Instruments and data-sets

The instruments used in this work include two different types of ceilometers, a Doppler lidar, a MWR, and RSs. In the following, a summary of each instrument is given. In order to successfully cross-examine data and/or to assimilate it synergetically, collocated measurements taken in April/May 2013 at the JOYCE *Löhnert et al.* [2015] in Jülich, Germany are used for case studies and statistical analysis.

1.5.1 Vaisala CT25K ceilometer

Figure 1.3: Vaisala CT25k ceilometer on the rooftop of the Jülich supersite.

Vaisala CT25K *Schween et al.* [2014]; *Löhnert et al.* [2015] ceilometer at JOYCE (Fig. 1.3) uses a transmission wavelength of 905 [nm] with a pulse repetition frequency (PRF) of 5.6 [kHz]. Under clear-sky conditions the typical sounding range of the instrument is roughly

Table 1.1: Specifications of the Vaisala CT25k ceilometer.

Parameter	Specification
Wavelength	• 905 [nm]
Transmission parameters	• Pulse repetition frequency (PRF): 5.6 [kHz]
Range	• 60. . .7500 [m]
Range Resolution	• 30 [m]
Receiver field-of-view (FOV)	• 0.66 [mrad]
Power Consumption	• max 400 [W] (including heating)
Weight, Dimensions	• 70 [kg] (complete system), 378 × 447 × 1335 [mm]

from 60 to 7,500 [m] with a range resolution of 30 [m] and time resolution of 15 [s]. The receiver field-of-view (FOV) is 0.66 [mrad]. Since this ceilometer is a co-axial system (laser and receiving-telescope optical axis coincide) its minimum sounding height of approximately 60 [m] is caused by the near-range saturation effect. The instrument software provides profiles of the attenuated backscatter coefficient β^{att} as an output. Table 1.1 summarizes its key specifications.

1.5.2 Jenoptik CHM15k Nimbus ceilometer

The Jenoptik CHM 15k Nimbus ceilometer *Schween et al.* [2014]; *Löhnert et al.* [2015] operates at a wavelength of 1064 [nm] with a pulse duration of 5 [ns] and repetition rate of $5 - 7$ [kHz]. Its maximum range, under clear-sky conditions, is 15 [km] with a range resolution of 15 [m]. The temporal resolution of the instrument is 15 [s]. Since it is a bi-axial system with separate optics for transmitter and receiver, the full overlap is available from above 350 [m]. However, this does not typically pose any limitation for mixing layer studies since the MLH is normally in the range of a few kms. Table 1.2 summarizes key specifications of the Jenoptik CHM 15k Nimbus ceilometer installed at JOYCE (Fig. 1.4).

1.5.3 HATPRO microwave radiometer (MWR)

A MWR measures the column-integrated values of atmospheric radiation in terms of brightness temperature. Measurements at different frequency bands and elevation angles can be used to derive several physical quantities such as temperature, water vapor, integrated water vapor, and integrated liquid water. The HATPRO MWR (Fig. 1.5) manufactured by RPG *Rose et al.* [2005]; *Löhnert et al.* [2015] measures the atmospheric brightness temperature at seven frequencies and seven angles in two bands. Measurements in the K-band, 20-30 [GHz]

Figure 1.4: Jenoptik CHM 15k NIMBUS ceilometer on the rooftop of the Jülich supersite.

Table 1.2: Specifications of the Jenoptik CHM 15k NIMBUS ceilometer *Jenoptik* [2013].

Parameter	Specification
Wavelength	• 1064 [nm]
Transmission parameters	• Pulse duration: 1. . . 5 [ns], Pulse repetition frequency (PRF): 5-7 [kHz]
Range	• 5. . .15,000 [m]
Range Resolution	• 5 [m]
Laser Divergence	• <0.3 [mrad]
Receiver field-of-view (FOV)	• 0.45 [mrad]
Power Consumption	• 250 [W]
Weight, Dimensions	• 70 [kg] (complete system), 500 × 500 × 1550 [mm]

range, are used for WV retrieval, and in the V-band, 50-60 [GHz] range, for temperature retrieval. It works in two scanning modes, zenith-pointing mode for full tropospheric profiling (range up to 10 [km], vertical *discretization* of 150-250 [m]), and boundary-layer scanning mode (6 elevation angles, range up to 1000 [m], vertical *discretization* 50 [m]). Measurement

Figure 1.5: RPG HATPRO on the rooftop of the Jülich supersite.

time resolution is about 2.70 minutes.

The limited vertical-resolution of the MWR-retrieved quantities (e.g., physical temperature) is inherently due to having less Degrees of Freedom (DoF) than the available measurement channels. Thus, for temperature retrieved profiles only about four pieces of independent information are available *Löhnert and Maier* [2012]. Therefore, the true vertical *resolution* on the inverted products ("clean-data" spatial resolution) is much lower than the vertical discretization of the retrieved temperature profile. When compared with RS measurements Löhnert and Maier (2012) have shown random differences between MWR and RS down to 0.5 [K] in the lower boundary-layer increasing to 1.7 [K] at 4 [km] in height. Table 1.3 summarizes key specifications of RPG HATPRO.

1.5.4 Graw DFM-09 radiosonde

A RS is an *in situ* instrument that is capable of measuring temperature, pressure, Relative Humidity (RH), and wind speed and direction in the atmosphere up to about 30 [km] by vertical sounding. It is launched through a large balloon inflated with hydrogen or helium gas. During its flight up to 30 [km] in height, it can drift more than 200 [km] away from above the point of its launch, though the horizontal displacement within the ABL is not significant for practical purposes. Nevertheless, the vertical profiles of atmospheric parameters measured by the RS are still considered a *de facto* reference or physical truth for the remote sensing purposes. The radiosonde used in this work is the Graw DF-09 manufactured by Graw GmbH and it includes temperature, pressure, wind and humidity sensors.

Table 1.3: Specifications of the RPG HATRPRO *RPG* [2011].

Parameter	Instrument specification
Temperature profile performance	• *Vertical discretization*: BL-Mode: 30 m-50 m (range 0-1200 m) Z-Mode: 200 m (range 1200-5000 m), 400 m (range 5000-10000 m) • *Accuracy*: 0.25 K, RMS (range 0-500 m), 0.50 K RMS (range 500-1200 m) 0.75 K RMS (range 1200-4000 m), 1.00 K RMS (range 4000-10000 m)
Humidity profile performance	• *Vertical discretization*: 200 m (range 0-2000 m), 400 m (range 2000-5000 m), 800 m (range 5000-10000 m) • *Accuracy*: 0.4 g/m^3 RMS (absolute humidity), 5% RMS (RH)
Channel center frequencies	• K-Band: 22.24 GHz, 23.04 GHz, 23.84 GHz, 25.44 GHz, 26.24 GHz, 27.84 GHz, 31.4 GHz • V-Band: 51.26 GHz, 52.28 GHz, 53.86 GHz, 54.94 GHz, 56.66 GHz, 57.3 GHz, 58.0 GHz
Radiometric range and accuracy	• Range: 0-800 K, Absolute brightness temperature accuracy: 0.5 K

1.5.5 HALO Photonics Streamline wind lidar

Doppler wind lidar along with radiosondes (whenever available) are used as the reference or truth. The Doppler lidar used in this work is the HALO Photonics Streamline Wind Lidar *Pearson and Collier* [1999]; *Pearson et al.* [2010]; *Schween et al.* [2014]. The instrument is a coherent pulsed Doppler lidar with an average pulse energy of 100 [μJ] at a frequency of 15 [kHz]. The maximum range of the instrument is 8 [km] but, in practice, it is limited by the absence of aerosols in the upper atmosphere. The vertical resolution of the instrument is 30 [m]. MLH from the Doppler lidar is determined by the standard deviation, σ_w, of the vertical wind velocity every 5 [min] when using a sliding temporal window of 30 [min].

1.5.6 The Jülich ObservatorY for Cloud Evolution (JOYCE)

The JOYCE is located in Forschungszentrum Jülich in the western part of Germany. JOYCE contains an array of state-of-the-art active and passive remote sensing and in-situ instruments for the observation of clouds and related processes *Löhnert et al.* [2015]. The data used in this work has been collected during the HOPE campaign at JOYCE. HOPE was conducted during April 02-July 24, 2013. During the measurement period 226 soundings of Graw DFM-09 have been performed and used, among others, for a water vapor intercomparison study *Steinke et al.* [2015].

1.6 Organization of the Ph.D. thesis

This Ph.D. thesis is organized as follows:

Chapter 1 provides an overview of the ITARS project, the topic of this Ph.D. thesis and related Ph.D. objectives, as well as the remote-sensing instruments used.

Chapter 2 reviews lidar and radiometric remote sensing. From the lidar side, concepts such as atmospheric extinction and backscatter, the lidar equation, and an overview of the lidar instrument will be covered. For the MWR part, RTM, inversion techniques, and MWR instrument will be covered.

Chapter 3 focuses on the study of a synegrtic algorithm for MLH estimation. A review of the uncertainties associated to existing MLH estimation methods from lidar backscatter (EKF method) and MWR-retrieved potential temperature (parcel method) is first presented. Second, a synergetic MLH estimation method will be formulated.

Chapter 4 covers the first part on the development of SBLH estimation methods. In this chapter, first the SBLH estimation problem is formulated for both the lidar and the MWR. Then, a MVRs-based SBLH estimation method is presented for the lidar case. Finally, SBLH estimation from MWR-retrieved potential-temperature profiles is presented by using idealized models from the literature.

Chapter 5 covers the second part of SBLH estimation methods. This chapter focuses on synergetic SBLH estimation from combined backscatter lidar and MWR-retrieved potential temperature measurements.

Chapter 6 introduces the LES model as a way to better understand the ABL and its related concepts. Simulated brightness-temperature data will be used for direct retrieval of the MLH. This chapter is inherently prospective in itself.

Chapter 7 gives concluding remarks and future lines of work.

Chapter 2

Lidar and microwave radiometric atmospheric remote sensing

This chapter summarizes the basic concepts and principles of lidar and radiometric remote sensing. Key concepts concerning atmospheric remote sensing using these sensors such as the lidar equation, atmospheric extinction and backscatter, the microwave radiative transfer model and atmospheric temperature-retrieval are presented. A brief overview of the diurnal cycle of the atmospheric boundary-layer height, its development and state-of-art retrieval methods is also presented.

2.1 Introduction

ABLH is defined as the height of the atmosphere which is directly affected by the changes on the surface of the Earth on a time scale of an hour or so *Stull* [1988]. It is a parameter of interest for many applications which include weather forecasting, air quality and chemical dispersion models and avionics. However, there is no instrument or method which can directly measure the ABLH. Instead, a proxy or tracer for the ABL can be used. Such proxies, among others, include aerosols in atmosphere, the temperature profile, wind profile and energy flux *Emeis* [2010]; *Seibert et al.* [2000].

Ground-based remote-sensing instruments provide an economic and reliable way of continuously monitoring the atmospheric boundary-layer at a single location. There are several such instruments which include active ones like lidar, radar, and sodar etc. and passive ones such as MWR.

In this work, ground-based lidar and MWR instruments for the retrieval of ABLH will be used. Lidar measures the backscattered light from the atmospheric constituents which it transmits, as a nearly monochromatic pulse, in the first place. MWR measures the column-integrated values of the atmospheric brightness temperature at several frequencies and elevation angles.

Lidar - Ground-based remote sensing of the lower atmosphere by backscatter lidars (e.g., ceilometers) is widely used because it enables spatial resolution of a few meters and time resolution of a tens of seconds to a couple of minutes. The European Aerosol Research Lidar Network (EARLINET) and the NASA's Micro-Pulse Lidar Network (MPLNET) are two examples of such lidar networks, spread over continental scale in the first case, and planetary scale in the second, providing aerosol measurements comprehensively in the vertical and temporal domains. Therefore, the search for an ABLH estimation method based on lidar data-only is one of the active and most relevant research topics today.

A ground-based lidar uses the backscatter from airborne atmospheric constituents (aerosols and molecules) to provide an indicator for the ABLH. Towards the near-infrared (NIR), aerosol backscatter is the dominant scattering source. While it has been shown that aerosols are good tracers of the Mixing Layer (ML) in case of fully developed convection *Emeis et al.* [2008]; *Haeffelin et al.* [2012]; *Lange et al.* [2014], the situation gets complicated during night-time when stable conditions frequently prevail. Some of the key challenges related to the estimation of the SBLH from a lidar signal include the presence of multiple aerosol layers *Stull* [1988]; *Haeffelin et al.* [2012], the lidar overlap factor, the effect of humidity on the aerosol concentration, and the presence of low-level clouds *Pandolfi et al.* [2013]. Insufficient overlap between transmitted and detected lidar signal strongly depends on the type of the lidar and varies from a few meters to a couple of hundred meters.

MWR - Atmospheric remote sensing by MWRs is based on the reception and processing of atmospheric radiation in the microwave region of frequencies. Atmospheric gases and water content emit ElectroMagnetic (EM) radiations due to their thermodynamic state, and at the same time absorb and scatter the EM energy coming from sun and other sources. The major contributors of emissions in the microwave band are oxygen and WV. In the 100 [GHz] range WV has an absorption line at 22.235 [GHz] and oxygen has a band of absorption lines spanning from 53-67 [GHz] with peak value at 60 [GHz]. Liquid water absorption dominates the 30-50 [GHz] frequency range *Hewison* [2006]*Planck and Masius* [1914]*Chandrasekhar* [1950]*Rybicki and Lightman* [2004].

In the RTM of a microwave radiometer, scattering is normally ignored in clear-sky conditions due to the larger wavelength of the received microwave radiation in comparison to size of the gas molecules and the WV. In case of clouds or rain in the atmosphere, which can have a particle size comparable to the wavelength of the radiations, scattering effects also become significant and need to be taken into account *Ulaby et al.* [1981]*Janssen* [1993].

The received intensity of the radiations can be assumed to be the sum of infinitesimally small stratified layers of atmosphere and is expressed in terms of the brightness temperature, T_B. The required profile of the atmospheric parameters, i.e., temperature, humidity, Integrated Water Vapor (IWV) and Integrated Precipitable Water (IPW) can then be extracted using a series of observations at different frequencies or elevation angles. The retrieval is based on a set of coefficients called weighting functions for each level of vertical resolution.

These coefficients are mostly calculated in advance using measurements from radiosondes or other *in-situ* methods *Ulaby et al.* [1981]*Janssen* [1993]*Askne and Westwater* [1986]*Crewell et al.* [2001].

2.2 Lidar remote sensing

For the studies related to low troposphere, and especially in the ABL, lidar-ceilometers are the most popular instruments due to them being lightweight, robust and economical. A ceilometer is a single-wavelength elastic backscatter lidar system, meaning it transmits and receives at a single wavelength, and is generally used for the detection of cloud-base height. It works on the principle of LIght Detection And Ranging (LIDAR), essentially measuring the backscattered light, after the emission of a laser pulse. The time of flight of the backscattered pulse is used to determine the distance to the target/height distribution of the atmospheric scatterers. Under relatively clear atmospheric conditions (typically, optical thickness, $\tau < 1$), the range-corrected intensity of the backscattered lidar signal is essentially proportional to the aerosol/molecular concentration of the atmospheric mixture. Though ceilometry refers to "cloud height and extent" and the fact that former ceilometer instruments were initially designed for cloud-base height detection only, today, modern ceilometers can usually detect both the ABLH and the cloud-base height. In case of semi-transparent clouds multiple layers can be observed. Most ceilometers are designed to transmit in the infra-red region of the spectrum, e.g., Vaisala CT25k and Jenoptik CHM15k Nimbus ceilometers transmit at the wavelengths of 906 [nm] and 1064 [nm], respectively.

Ceilometers are single wavelength, elastic lidar systems and, therefore, a low-cost simplistic version of a multi-wavelength lidar system. A detailed treatment of the multi-spectral Raman lidar system at UPC RSLAB has been presented in the previous doctoral thesis by *Kumar* [2012] and the related processing for the retrieval of the optical atmospheric parameters and the ABLH in another doctoral thesis by *Lange* [2014]. Therefore, in the following only the key concepts related to lidar instrument and its working principles are summarized, for the sake of completeness.

Like the lidar, a ceilometer, as shown in Fig. 2.1, has three main hardware modules, namely, the laser, the telescope, and the detection and processing system.

The transmission system of a ceilometer consists of a laser which transmits lights pulses along the Line-Of-Sight (LOS) of the instrument at a single wavelength with given specifications of pulse energy (1.6 [μJ] for Vaisala CT25k and 8 [μJ] for Jenoptik CHM15k), pulse repetition frequency (5.6 [kHz] for Vaisala CT25k and 5-7 [kHz] for Jenoptik CHM15k), and pulse duration (100 [ns] for Vaisala CT25k and 1-5 [ns] for Jenoptik CHM15k) *Schween et al.* [2014]; *Muenkel et al.* [2004]; *Wiegner and Geiß* [2012]. The transmitted power of the ceilometer is generally kept low to make it an eye-safe system. Nd:YAG (Neodymium-doped:

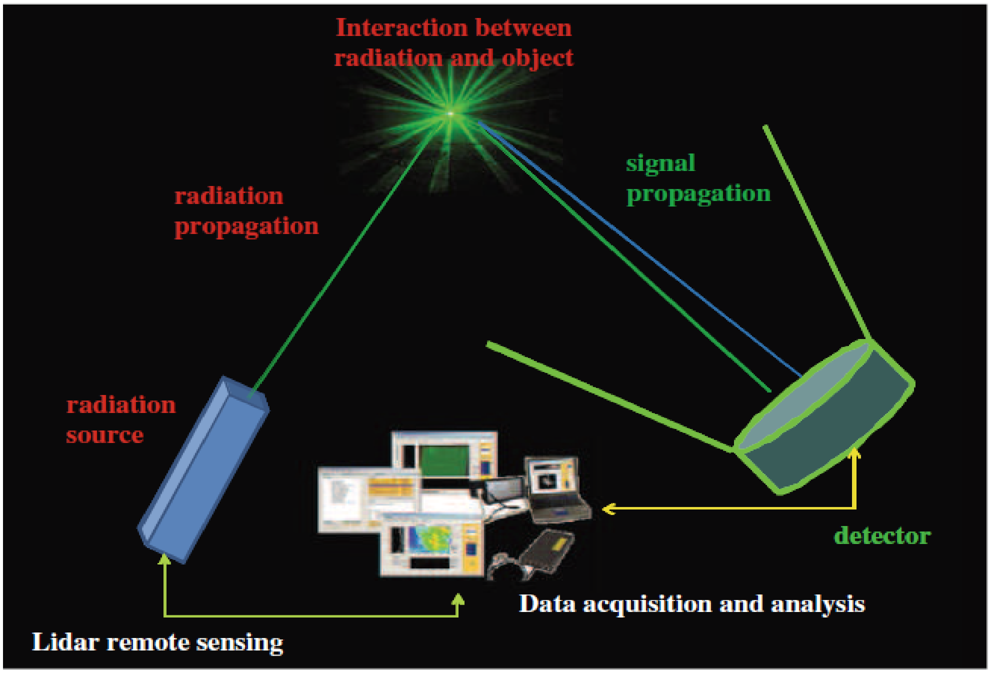

Figure 2.1: Functional ceilometer layout showing the main building blocks of a ceilometer instrument *Cimini et al.* [2010a].

Yttrium Aluminum Garnet) lasers are generally used as a laser source. Nd:YAG lasers emit in NIR spectral region at 1064 [nm]. The choice of transmission wavelength is generally dictated by the frequency window in which atmosphere is relatively transparent.

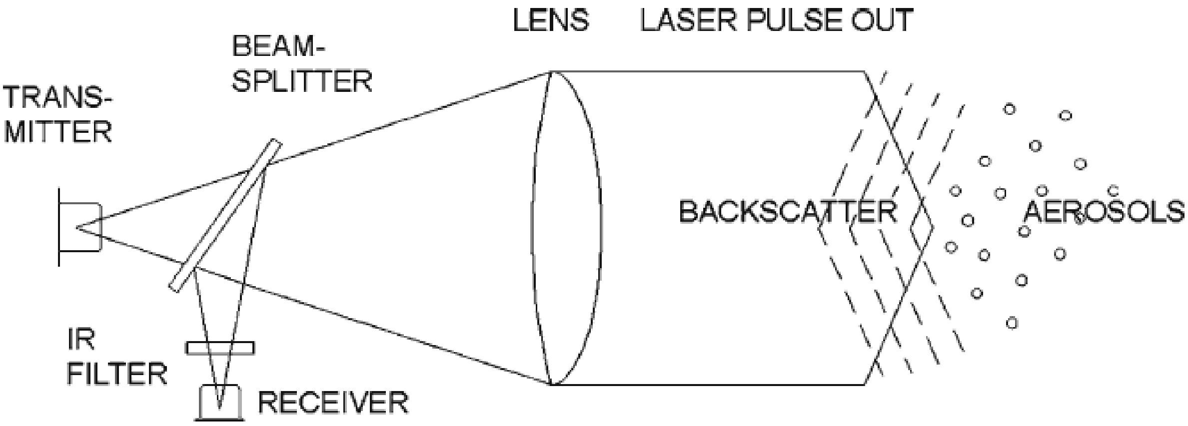

Figure 2.2: Mono-axial Vaisala CT25k laser-telescope ceilometer system *Münkel et al.* [2007].

The receiver system consists of a telescope which collects the backscattered light from the atmospheric constituents. The Field-Of-View (FOV) of the telescope, which is the angle between the laser beam and the axis of the telescope, determines the effective amount of received light and the lowest height of full-overlap. Based on the design of the system, there can be two types of arrangements for the telescope axis and the laser's line of transmission. A mono-axial system, where the telescope FOV and the laser beam share the same axis, provides full-overlap virtually starting from the point of emission. Such a system, as used in Vaisala ceilometers, is shown in Fig. 2.2 *Münkel et al.* [2007]. In contrast, a bi-axial system, where the laser beam and the telescope FOV are separate, provided full-overlap between the two starting from several hundred meters above the ground. Jenoptik ceilometers use such a bi-axial system.

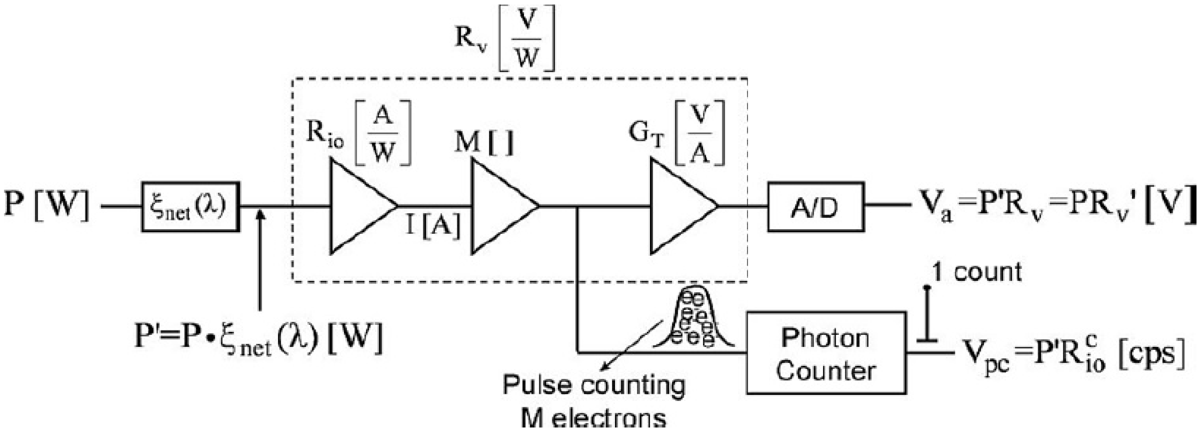

Figure 2.3: Generalized block diagram of a lidar receiving channel using a PMT-based detection *Lange* [2014].

There are two main types of detectors depending on the incident optical wavelength: The Avalanche Photo-Diode (APD) and the Photo-Multiplier Tube (PMT). APD detectors are particularly suited for the detection of near-infrared (NIR) wavelengths while PMT detectors for the visible (VIS) and ultra-violet (UV) range. Besides, PMT detectors enable quantum-level detection, i.e., the possibility of detecting individual photons and hence, they are more sensitive than APD detectors. Fig. 2.3 shows a generalised lidar channel detection front-end using a PMT-based detection head and combined analog (analog-to-digital-converter, A/D) and photon-counting acquisition units.

2.2.1 Atmospheric extinction

A laser transmitted pulse of light from a ceilometer experiences extinction while passing through the atmosphere *Collis and Russell* [1976]; *Emeis* [2010]; *Lenoble et al.* [2013]. Extinction results from absorption as well as scattering from the constituents (gaseous molecules and aerosols) of the atmosphere. The received intensity of a given pulse of light with initial intensity, I_0, and wavelength, λ, while passing through a section of atmosphere between heights $z = 0$ to $z = Z$ is given by Beer's law *Beer* [1852] as

$$I(\lambda, Z) = I_0 exp\left(-\int_0^Z \alpha(\lambda, z)dz\right), \tag{2.1}$$

where α is total extinction coefficient in [m^{-1}], and $T(\lambda, Z) = exp\left(-\int_0^Z \alpha(\lambda, z)dz\right)$ is the atmospheric transmissivity.

The total extinction coefficient, α, can be represented as the sum of individual sources as follows

$$\alpha = \alpha_{sca,aer} + \alpha_{sca,mol} + \alpha_{abs,mol}, \tag{2.2}$$

where $\alpha_{sca,aer}$ is the Mie aerosol scattering, $\alpha_{sca,mol}$ is the Rayleigh molecular scattering, and $\alpha_{abs,mol}$ is the molecular absorption.

Scattering is a function of the physical properties (e.g., refractive index, cross section, radii distribution) of the atmospheric constituents. Scattering of photons by the aerosols and the molecules can be defined in terms of their relative size with respect to the wavelength of the incident light. On one hand, scattering by the aerosols is defined by Mie's scattering, in which the size of scatterers is comparable to that of the incident wavelength. On the other hand, the molecular scattering, $\alpha_{sca,mol}$, is defined by the Rayleigh scattering mechanism since the size of the molecules is generally much smaller than the wavelength of the incident light.

The scattering by aerosols, $\alpha_{sca,aer}$, is described in terms of Mie scattering (Mie scattering coefficient $\approx \lambda^{-K}$; $0 \leq K \leq 2$) and is given by

$$\alpha_{sca,aer} = \int_0^\infty \pi a_{aer}^2 Q_{ext}(x, m) N_{aer}(a_{aer}) da, \tag{2.3}$$

where a_{aer} is the aerosol radius, Q_{ext} is the extinction efficiency, x is the particle size parameter ($x = 2\pi a_{aer}/\lambda$ [.], λ the wavelength, a_{aer} the particle's radius), m is complex refractive index [.], and N_{aer} is the aerosol density per unit radius interval [m^{-3}]. Rayleigh scattering coefficient is proportional to λ^{-4} (Rayleigh's spectral law) and is given in terms of the number density of gas molecules [no. of molecules/m^3], N_g, and the Rayleigh's scattering cross-section [m^2/molecule], $\sigma_{RAY}(\lambda)$, as follows

$$\alpha_{sca,mol} = N_g \sigma_{RAY}(\lambda). \tag{2.4}$$

Fig. 2.4 outlines the changes in the relative strengths of total extinction and the backscatter in response to wavelength of incident light and different atmospheric species.

Molecular absorption, $\alpha_{abs,mol}$, becomes a significant component of the total extinction only when the laser wavelength is tuned-in in an absorption band of the atmospheric molecule (or gas species) of interest. This is not the case of backscatter lidars and ceilometers, which only rely on elastic interaction, that is, aerosol (Mie's) and molecular (Rayleigh's) scattering.

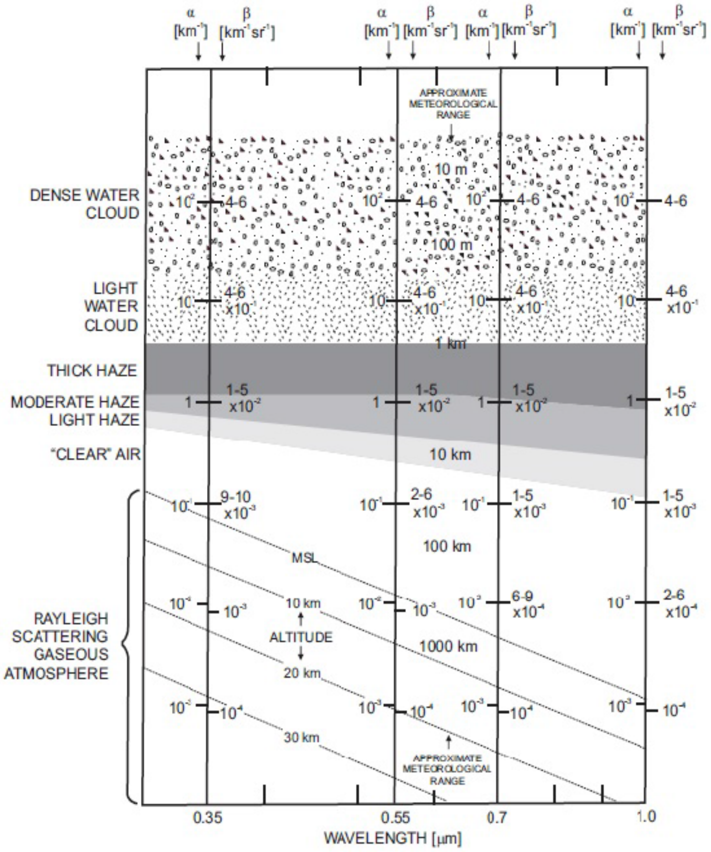

Figure 2.4: Optical extinction and backscatter coefficients with respect to wavelength and the atmospheric constituents. *Collis and Russell* [1976].

2.2.2 Atmospheric backscatter

The component of the scattered light signal which is received by the telescope of the ceilometer is the one which is scattered backwards at 180 degrees to the incident light pulse and includes contributions from molecular as well as aerosol scattering. The total backscatter coefficient, β, therefore, is the sum of molecular backscatter, β_{mol}, and aerosol backscatter, β_{aer}, coefficients

$$\beta = \beta_{mol} + \beta_{aer}. \tag{2.5}$$

The total backscatter coefficient is directly related to the amount of light intensity received at the telescope of the lidar. The individual contributions from the molecular backscatter, β_{mol}, and the aerosol backscatter, β_{aer}, can be formulated on the similar lines as the total molecular scattering, $\beta_{sca,mol}$ (Eq. 2.4), and aerosol scattering, $\beta_{sca,aer}$ (Eq. 2.3). Consequently,

$$\beta_{mol} = N_g \frac{d\sigma_{RAY}(\pi, \lambda)}{d\Omega}, \tag{2.6}$$

where $\frac{d\sigma_{RAY}(\pi,\lambda)}{d\Omega}$ [$\mathrm{m}^{-1}\mathrm{sr}^{-1}$] is the fractional Rayleigh scattering per solid angle unit in the backward direction. And

$$\beta_{aer} = \int_0^\infty \pi a_{aer}^2 Q_{back}(x,m) N_{aer}(a_{aer}) da, \tag{2.7}$$

where Q_{back} is the backscatter efficiency.

Whereas it is a challenge to precisely formulate the aerosol backscatter, β_{aer}, due to its dependence on shape, size and composition of aerosols, of special relevance is the dependence of aerosol size on the amount of humidity in the atmosphere. A study to explore the relationship between humidity and aerosol backscatter, and variations of the aerosol concentration during day-time and night-time has been performed by *Pandolfi et al.* [2013]. Results indicate that the mean backscatter coefficient behaved in opposite fashion to the diurnal cycle of humidity with higher values during the night-time and lower values during the day-time. Since the size of the aerosols varies with the moister content in the air *Eresmaa et al.* [2006] due to hygroscopic effects, the higher backscatter coefficient during the night-time is linked to a higher amount of humidity in the atmosphere.

2.2.3 The elastic lidar equation

Finally, the relationship between the measured lidar backscattered signal and the total backscatter coefficient is described by the, so called, lidar equation. The lidar power return is given by the single-scattering elastic lidar equation *Measures* [1992],

$$P(z) = \frac{C}{z^2}\beta(z)T^2(z), \tag{2.8}$$

where $\beta(z)$ is the range-dependent total volume backscatter coefficient of the atmosphere [$\mathrm{m}^{-1}\mathrm{sr}^{-1}$] (Eq. 2.5), $\mathrm{T}^2(\mathrm{z}) = \mathrm{e}^{-2\int_0^z \alpha(z')dz'}$ is the two-way path atmospheric transmittance, and C is the system constant [Wm^3]. The quantity $\beta(z)T^2(z)$ is known as the attenuated backscatter coefficient,

$$\beta^{att}(z) = \frac{z^2}{C}P(z). \tag{2.9}$$

Under moderate-to-clear atmospheres and lidar sounding paths roughly below 3 [km], the transmittance term can be assumed close to unity and, therefore, $\beta^{att}(z) \cong \beta(z)$ *Münkel et al.* [2007]; *Lange et al.* [2014]. In the following, the term $\beta(z)$ will be used to refer to the lidar attenuated backscatter or simply “the backscatter”.

In practice, the range-dependent background-subtracted received lidar signal is corrupted by observation (measurement) noise and takes the form,

$$Q(z) = P(z) + n(z), \tag{2.10}$$

where $P(z)$ is the ideal (i.e., noiseless) lidar power return, and $n(z)$ is the observation noise.

The noisy attenuated backscatter coefficient, $\beta'(z)$, in response to a measured (i.e., noisy) lidar signal, $Q(z)$, can be obtained from Eq. 2.9 by substituting $Q(z)$ (Eq. 2.10) in place of $P(z)$. It follows that

$$\beta'(z) = \beta(z) + v(z), \tag{2.11}$$

where $\beta'(z)$ is the noisy attenuated backscatter coefficient, $\beta(z)$ is the noiseless attenuated backscatter coefficient, and $v(z) = \frac{z^2}{C}n(z)$ is the range-corrected noise scaled by the lidar system constant, C. Primes denote noise-corrupted variables. In the following, the term $\beta'(z)$ will be used to refer to the lidar-ceilometer attenuated backscatter or simply "the backscatter".

2.3 Microwave radiometer remote sensing

2.3.1 Radiative transfer modelling

A ground-based MWR (microwave frequency range: 0.3 GHz to 300 GHz) measures the amount of atmospheric radiation in terms of spectral radiance, I_ν $[\mathrm{W \cdot m^{-2} \cdot sr^{-1} \cdot Hz^{-1}}]$, which is given by

$$I_\nu = \int_0^\infty B_\nu(r,T)\alpha_\nu(r)e^{-\tau_\nu(r,\infty)}dr + I_0 e^{-\tau_\nu(0,\infty)}, \tag{2.12}$$

where I_0 is the cosmic background term, α_ν $[\mathrm{Nep \cdot m^{-1}}]$ is the absorption coefficient, $\tau_\nu(0,R) = \int_0^R \alpha_\nu(r)dr$ [Nep] is the optical thickness of the sounding path over the range interval $(0,R)$, usually along the vertical direction, and B_ν is the spectral radiance of a *blackbody*. The subscript ν shows the frequency dependence of quantities *Janssen* [1993]; *Mattioli et al.* [2013]; *Ulaby et al.* [1981]. The spectral radiance, B_ν $[\mathrm{W \cdot m^{-2} \cdot sr^{-1} \cdot Hz^{-1}}]$, of a blackbody at physical temperature, T [K], is given by Plank's law

$$B_\nu(T) = \frac{2h\nu^3}{c^2}\frac{1}{e^{\frac{h\nu}{kT}} - 1}, \tag{2.13}$$

where h is the Plank's constant, k_B is the Boltzmann constant, and c is the speed of light.

The emission and absorption of radiation from the atmosphere is a result of continuous absorption, scattering, and re-emission of radiation and incident energy from other cosmic sources. The frequency of emission is directly related to the energy levels of the constituents of atmosphere, which include gases like oxygen, O_2, nitrogen, N_2, carbondioxide, CO_2, WV, and cloud liquid-water. In the microwave region of frequencies, especially in the 10-100 [GHz] range, oxygen and WV are the dominant absorbers of EM energy. Fig. 2.5 shows

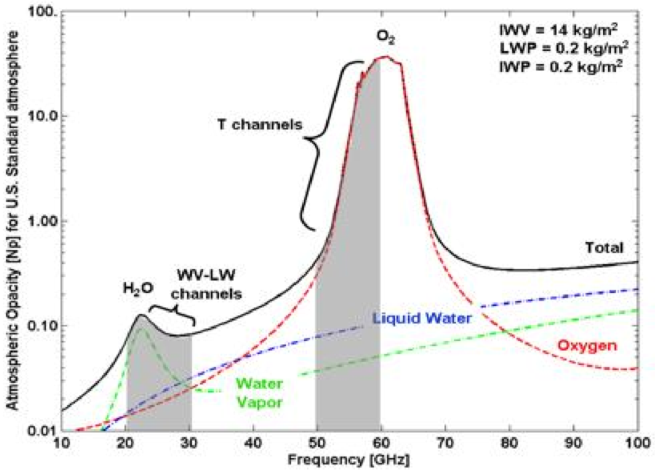

Figure 2.5: Atmospheric opacity for U.S. standard atmosphere with liquid and ice water clouds. The ice water contribution is below 0.01 [Np] throughout the 10-100 [GHz] range. The spectral range of commercially available water vapor (K-band 20-30 [GHz]) and temperature (V-band 50-60 [GHz]) microwave profilers is indicated *Illingworth et al.* [2013].

the atmospheric opacity in the 10-100 [GHz] frequency range, the oxygen absorption band in the 50-60 GHz, and WV and Liquid Water (LW) continuum (proportional to ν^2) in the 20-30 [GHz] range. The effects of scattering are negligible for frequencies below 100 [GHz] in non-rainy conditions, and hence are not considered in this work.

The frequency and height dependent net absorption coefficient, for frequencies below 100 [GHz], is the sum of the individual contributions, and can be given by

$$\alpha_\nu(r) = \alpha_{O_2}(r) + \alpha_{WV}(r) + \alpha_C(r), \tag{2.14}$$

where α_{O_2} is the oxygen absorption coefficient, α_{WV} is the WV absorption coefficient, and α_C is the cloud liquid-water absorption coefficient *Ulaby et al.* [1981].

Since the absorption of oxygen is dependent upon the atmospheric temperature and density (through pressure), the total absorption coefficient, α_ν, of atmosphere, in general, is a function of temperature, dry density, ρ, WV density, ρ_{WV}, and cloud liquid density, ρ_C,

$$\alpha_\nu(r) = \alpha\left(T(r), \rho(r), \rho_{WV}(r), \rho_C(r)\right). \tag{2.15}$$

In clear-sky conditions, the contribution from cloud liquid-water can be neglected, therefore, the absorption coefficient is solely due to gaseous components, i.e., oxygen and WV absorptions,

$$\begin{aligned} \alpha_\nu(r) &= \alpha_g(r) = \\ &= \alpha_{O_2}(r) + \alpha_{WV}(r). \end{aligned} \tag{2.16}$$

In order to simplify the units of measurement, Plank's law from Eq. 2.13 can be solved for the physical temperature of the blackbody (usually using the Rayleigh-Jeans approximation). Likewise, for a non-blackbody, the so-called *greybody*, with the same spectral radiance as that of the ideal blackbody, an equivalent temperature called *brightness temperature*, $T_{B\nu}$ [K], can be derived *Mattioli et al.* [2013]. From Eq. 2.12, and the considerations above, the brightness temperature of the atmosphere, which is also a greybody, measured by a ground-based MWR, can be expressed as

$$T_{B\nu} = \int_0^\infty T(r)\alpha_\nu(r)e^{-\tau_\nu(0,r)}dr + T_{BG}e^{-\tau(0,\infty)}, \tag{2.17}$$

where T_{BG} is the background brightness temperature and T is the physical temperature of the *greybody* (which is always greater than $T_{B\nu}$ for the atmosphere).

Eq. 2.17 encompasses a relationship between the MWR measured quantity, i.e., $T_{B\nu}$, and the physical temperature profile of the atmosphere in the form of a Fredholm integral of the first-kind *Hanna et al.* [2005]. The retrieval of temperature profile from Eq. 2.17 requires a solution to this ill-posed problem (multiple number of temperature profiles which result in the same measured $T_{B\nu}$). The problem is further complicated due to the dependence of $T_{B\nu}$ on $\alpha_\nu(r)$ as well, which itself is a function of profiles of temperature, and density variables.

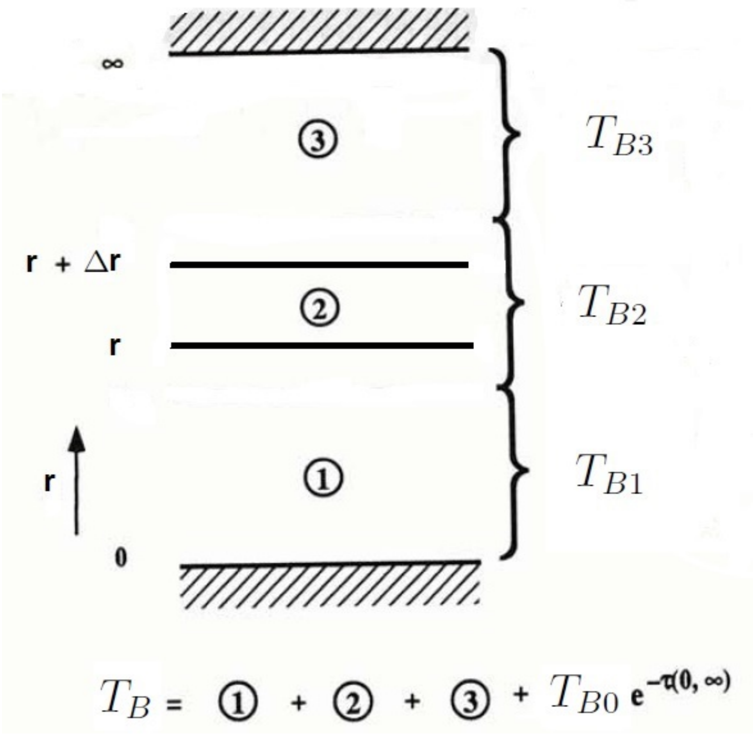

Figure 2.6: Layered structure of the atmosphere for the linearization of radiative-transfer-model (RTM) (Adapted from *Janssen* [1993]).

Towards this end, the RTM (Eq. 2.17) is linearized *Janssen* [1993], by first expressing the integral as sums over homogeneous layers i (Fig. 2.6). In the next step, the effect of small perturbations in the temperature, dT_i, and the absorption coefficient, $d\alpha_i$, on the received brightness temperature is considered. The subscript ν from T_B and α is dropped for convenience.

Fig. 2.6 shows the geometry involved in the linearization of Eq. 2.17 for a simplified atmosphere consisting of 3 layers and under the assumption of a horizontally stratified atmosphere. The contribution to T_B from the layer i extending from r to $r + \Delta r$ can be separated (second term), by first expressing Eq. 2.17 as

$$\begin{aligned} T_B = & \int_0^r T(u)\alpha(u)\kappa(0,u)du + \kappa(0,r)\int_r^{r+\Delta r} T(u)\alpha(u)\kappa(r,u)du + \\ & \kappa(0,r+\Delta r)\int_{r+\Delta r}^{\infty} T(u)\alpha(u)\kappa(r+\Delta r,u)du + T_{BG}\kappa(0,\infty), \\ = & T_{B1} + T_{B2} + T_{B3} + T_{B0}, \end{aligned} \tag{2.18}$$

where $\kappa(a,b) = e^{-\int_a^b \alpha(u)du}$ is the transmissivity in the range interval (a,b) and u is the variable of integration.

The contribution of the ith layer, $(r, r+\Delta r)$, to the measured T_B can be attributed to three terms which are directly influenced by the changes in it, and can be identified in Eq. 2.18 as

- direct contribution from the ith layer, $T_{B2} = \kappa(0,r)\int_r^{r+\Delta r} T(u)\alpha(u)\kappa(r,u)du$,
- contribution through the transmissivity term, $\kappa(0, r+\Delta r)$, in T_{B3},
- contribution through the background term, $T_{B0} = T_{BG}\kappa(0,\infty)$.

The response of T_B to the perturbations in temperature within the ith layer, can be calculated by taking the derivative of Eq. 2.18 with respect to temperature, in line with the three terms identified above (see Appendix B for details),

$$d^2T_B(r) = \left[\left(\frac{\partial T_{B,2}}{\partial T} + \frac{\partial T_{B,2}}{\partial \alpha}\frac{\partial \alpha}{\partial T}\right) + \left(\frac{\partial T_{B,3}}{\partial \alpha}\frac{\partial \alpha}{\partial T}\right) + \left(\frac{\partial T_{B,0}}{\partial \alpha}\frac{\partial \alpha}{\partial T}\right)\right] dT(r), \tag{2.19}$$

where $\left(\frac{\partial T_{B2}}{\partial T} + \frac{\partial T_{B2}}{\partial \alpha}\frac{\partial \alpha}{\partial T}\right) = \left[\kappa(0,r)\alpha(r) + \kappa(0,r)T(r)\frac{\partial \alpha(r)}{\partial T}\right] dr$, $\left(\frac{\partial T_{B3}}{\partial \alpha}\frac{\partial \alpha}{\partial T}\right) = -\kappa(0,r)\left(\frac{\partial \alpha}{\partial T}\right)$ $\left[\int_r^{\infty} T(u)\alpha(u)\kappa(r,u)du\right] dr$, and $\left(\frac{\partial T_{B0}}{\partial \alpha}\frac{\partial \alpha}{\partial T}\right) = -T_{BG}\kappa(0,\infty)\frac{\partial \alpha}{\partial T}dr$. Note that the variations of temperature and absorption in the bottom layer, $[0,r]$, $\frac{\partial T_{B1}}{\partial T}$ and $\frac{\partial T_{B1}}{\partial \alpha}\frac{\partial \alpha}{\partial T}$, respectively, do not contribute to $dT_B(r)$, which results due to perturbations in the layer i, $[r, r+\Delta r]$. Therefore, $\frac{\partial T_{B1}}{\partial T}|_{ith} = 0$, $\frac{\partial T_{B1}}{\partial \alpha}\frac{\partial \alpha}{\partial T}|_{ith} = 0$.

The quantity,

$$W_T(r) = \left[\left(\frac{\partial T_{B,2}}{\partial T} + \frac{\partial T_{B,2}}{\partial \alpha} \frac{\partial \alpha}{\partial T} \right) + \left(\frac{\partial T_{B,3}}{\partial \alpha} \frac{\partial \alpha}{\partial T} \right) + \left(\frac{\partial T_{B,0}}{\partial \alpha} \frac{\partial \alpha}{\partial T} \right) \right] / dr, \tag{2.20}$$

is commonly referred as the temperature weighting functions, and it directly relates the small perturbations in atmospheric temperature to the perturbations in the T_B in an infinitesimally small section, dr, of the atmosphere (i.e., $W_T(r)$ is a measure of the brightness temperature *increment*, i.e., dT_B, in response to an *incremental* change in temperature),

$$\Delta T_B \leftarrow W_T \Delta T. \tag{2.21}$$

Although, a common practice in the remote sensing community is to call $\alpha(r) \cdot \kappa(0, r)$ the temperature weighting functions, this is true only when the Rayleigh-Jeans approximation is valid for the frequencies of interest and $\frac{\partial \alpha}{\partial T} = 0$ *Janssen* [1993].

The changes in the T_B, however, are not always a function of temperature alone, instead they depend upon ρ, ρ_{WV}, and ρ_C as well *Janssen* [1993]; *Ulaby et al.* [1986], through α (Eq. 2.15). Hence, the total change in T_B over dr can be represented by

$$d^2T_B(r) = W_T(r)dT(r)dr + W_\rho(r)d\rho(r)dr + W_{\rho_{WV}}(r)d\rho_{WV}(r)dr + W_{\rho_C}(r)d\rho_C(r)dr, \tag{2.22}$$

where $W_\rho(r)$, $W_{\rho_{WV}}(r)$, and $W_{\rho_C}(r)$ are the weighting functions of dry density, WV, and the clouds liquid-water. Following similar reasoning as in the derivation of Eq. 2.20,

$$W_{\rho_x(r)} = \left[\left(\frac{\partial T_{B,2}}{\partial \alpha} \frac{\partial \alpha}{\partial \rho_x} \right) + \left(\frac{\partial T_{B,3}}{\partial \alpha} \frac{\partial \alpha}{\partial \rho_x} \right) + \left(\frac{\partial T_{B,0}}{\partial \alpha} \frac{\partial \alpha}{\partial \rho_x} \right) \right] / dr, \tag{2.23}$$

where x can represent dry density, WV density, and the cloud liquid-water density.

The total change in T_B over the full column of the atmosphere is then, the integral of the differential changes at each height, r, that is,

$$dT_B(r) = \int_0^\infty W_T(r)dT(r)dr + \int_0^\infty W_\rho(r)d\rho(r)dr + \int_0^\infty W_{\rho_{WV}}(r)d\rho_{WV}(r)dr + \int_0^\infty W_{\rho_C}(r)d\rho_C(r)dr. \tag{2.24}$$

Eq. 2.24 is known as linearized or perturbation form of the RTM. In the linearized RTM, the changes in the measured brightness temperature, $dT_B(r)$, due to changes in the physical temperature, dT, and the absorption coefficient, $d\alpha$, that occur only at height r, are considered. The resulting sensitivity equations can be assimilated into the inversion algorithms and adaptive filters, as “trajectory” information of T_B in response to changes in temperature and/or absorption.

It is also important to remember that the weighting functions are calculated in reference to some background or initial-guess profiles of all these variables (temperature, dry density, WV density, and cloud-liquid density) *Janssen* [1993]; *Ulaby et al.* [1986].

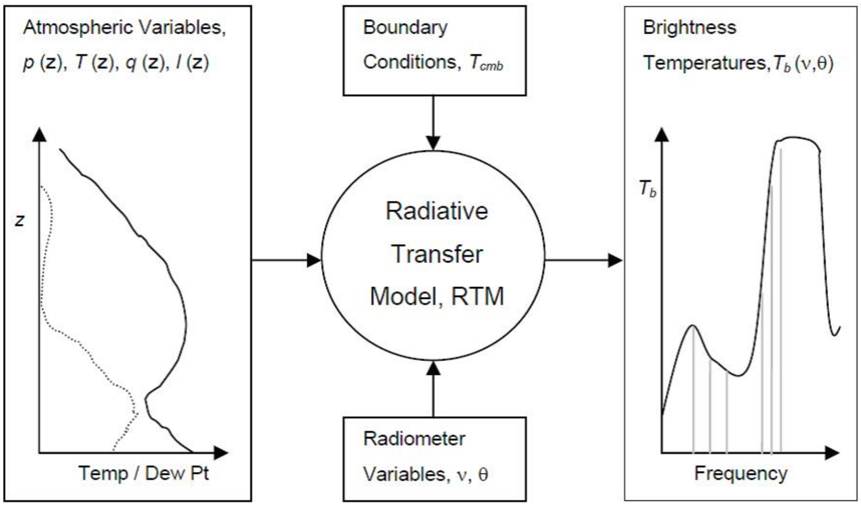

Figure 2.7: Schematic diagram of the forward problem of estimating observations from an atmospheric profile using the RTM *Hewison* [2006].

For retrieval purposes, generally, a Forward (FWD) model, which outputs a value of brightness temperature for given profiles of temperature, pressure, and humidity etc., by incorporating the physics behind the absorption and scattering properties of the atmospheric constituents, at the observation frequency and viewing angle, is used. Several FWD models *Liebe* [1989]; *Liebe et al.* [1993]; *Rosenkranz* [1998]; *Clough et al.* [2004]; *Cadeddu et al.* [2007]; *Eriksson et al.* [2011]; *McGarragh* [2012] have been developed over the years with varying features and degrees of accuracy, ranging from inclusion/omission of scattering effects, WV continuum, liquid water, pressure broadening effects, and the line parameters of oxygen and WV. The FWD model, which will be utilized for the purposes of this PhD thesis, was implemented at the UCOL, and is based on the additions of *Rosenkranz* [1998] to the millimeter-wave propagation model (MPM) *Liebe* [1989]. It is a non-scattering microwave RTM for the gas absorption, which outputs T_B values for the *input profiles of T, p* and *RH* at *given frequencies* and *angles*. Fig. 2.7 shows a schematic diagram of the use of RTM for simulating brightness temperature measurements.

The process of inverting the measured brightness temperature, $T_{B,meas}$, in order to retrieve the profiles of atmospheric parameters (temperature, WV density, and cloud liquid density), generally requires an initial-guess for these profiles *Rodger* [2000]; *Janssen* [1993]; *Ulaby et al.* [1986]. The guess profiles are then corrected based on the difference of $T_{B,meas}$

and $T_{B,guess}$ (obtained via FWD-model and the guess profiles), i.e.,

$$\delta T_B = T_{B,meas} - T_{B,guess}. \tag{2.25}$$

The process can be repeated until δT_B is minimized. When inverting for a particular quantity, e.g., temperature profile, the measurement frequency, or the so-called *spectral channel*, is chosen in such a way that the sensitivity of the measurements is maximized with respect to the perturbations in that parameter. However, there is always some influence on the measurements from other parameters, i.e., effect of WV and clouds on the temperature sounding, etc. As a result, for accurate retrieval, it is best to make simultaneous use of temperature, WV, and the cloud liquid channels, thereby, taking into account the influence of all these profiles together, on the measured brightness temperature *Janssen* [1993]; *Ulaby et al.* [1986].

Eq. 2.24 can be related to the standard form of Fredholm integral equation of the first-kind,

$$\begin{aligned} g_{e_i} &= g_i + \epsilon_i, \\ &= \int_a^b W_i(r) f(r) dr + \epsilon_i, i = 1, 2, \ldots, N \end{aligned} \tag{2.26}$$

where g_i is the ith "perfect" measurement, ϵ_i is the observation error, $W_i(r)$ is the known weighting function and $f(r)$ represents the unknown profile of temperature, and density variables in the height interval $a \leq r \leq b$. The N measurements can come from different measurement frequencies and/or scanning angles. The observation error, ϵ_i, can arise from different sources, which include *measurement noise*, *linearization errors*, *modelling errors*, and *weighting function errors.*

For computer implementation and numerical solution, a discrete number of points, $j = 1, 2, \ldots, M$ over continuous height interval, $a \leq r \leq b$, can be defined, and the integral can be approximated by the quadrature solutions (e.g., trapezium rule), resulting in a matrix form,

$$\boldsymbol{g}_e = \boldsymbol{A}\boldsymbol{f} + \boldsymbol{\epsilon}, \tag{2.27}$$

where $\boldsymbol{A}_{ij} = w_j \boldsymbol{W}_i(r_j), i = 1, 2, \ldots, N, j = 1, 2, \ldots, M,$ $\boldsymbol{f} = \left[f(r_1), f(r_2), \ldots, f(r_M)\right]^T$, $\boldsymbol{g}_e = \left[g_{e_1}, g_{e_2}, \ldots, g_{e_N}\right]^T$, and w_j is quadrature weight associated with the jth point.

In the simplest case of $f(r)$ representing only the unknown temperature profile, Eq. 2.26

can be expanded as

$$\begin{pmatrix} g_1 \\ g_2 \\ \vdots \\ g_N \end{pmatrix}_{N\times 1} = \begin{pmatrix} w_1 W_1(r_1) & w_2 W_1(r_2) & \dots & w_M W_1(r_M) \\ w_1 W_2(r_1) & w_2 W_2(r_2) & \dots & w_M W_2(r_M) \\ \vdots & \vdots & \ddots & \vdots \\ w_1 W_N(r_1) & w_2 W_N(r_2) & \dots & w_M W_N(r_M) \end{pmatrix}_{N\times M} \begin{pmatrix} f_1 \\ f_2 \\ \vdots \\ f_M \end{pmatrix}_{M\times 1} . \tag{2.28}$$

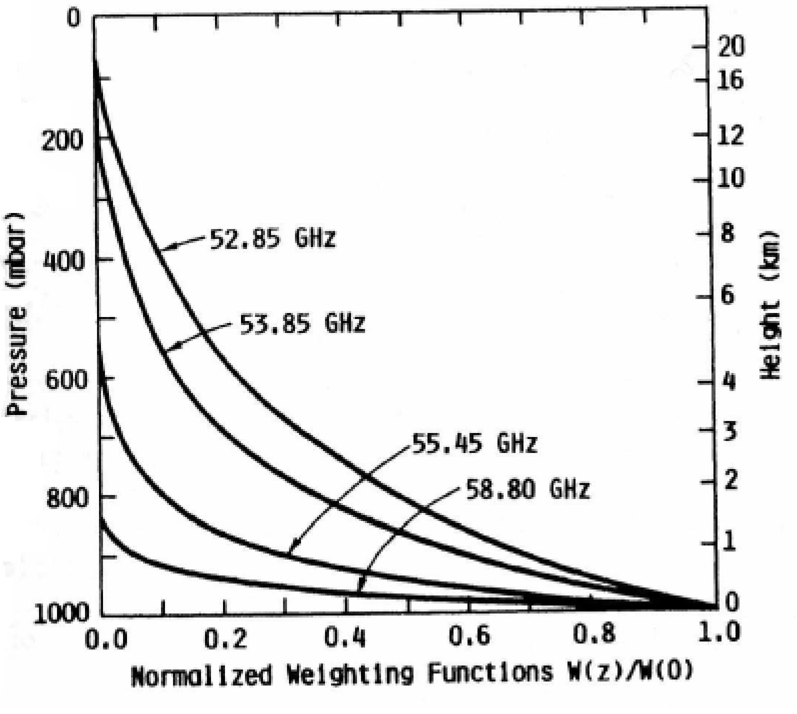

Figure 2.8: Weighting functions for measurements at four frequency channels (52.85 [GHz], 53.85 [GHz], 55.45 [GHz], 58.80 [GHz]) and in the zenith direction in 50-60 [GHz] Oxygen absorption band for temperature retrieval *Ulaby et al.* [1986].

Fig. 2.8 shows an example of weighting functions for measurements at four different frequencies (with zenith angle) illustrating the relevant contribution of these measurements towards temperature retrieval at different heights *Westwater and Grody* [1980]; *Ulaby et al.* [1986].

Another example in which $f(r)$ represents the unknown atmospheric state given by the combination of two variables (the temperature and the WV profiles), can be given as

$$\begin{pmatrix} g_1 \\ g_2 \\ \vdots \\ g_N \end{pmatrix}_{N\times 1} = \left[\begin{matrix} w_1W_1(r_1) & w_2W_1(r_2) & \dots & w_MW_1(r_M) \\ w_1W_2(r_1) & w_2W_2(r_2) & \dots & w_MW_2(r_M) \\ \vdots & \vdots & \ddots & \vdots \\ w_1W_N(r_1) & w_2W_N(r_2) & \dots & w_MW_N(r_M) \end{matrix}\right. \\ \left.\begin{matrix} w_1W_1'(r_1) & w_2W_1'(r_2) & \dots & w_MW_1'(r_M) \\ w_1W_2'(r_1) & w_2W_2'(r_2) & \dots & w_MW_2'(r_M) \\ \vdots & \vdots & \ddots & \vdots \\ w_1W_N'(r_1) & w_2W_N'(r_2) & \dots & w_MW_N'(r_M) \end{matrix}\right]_{N\times 2M} \begin{pmatrix} f_{T_1} \\ f_{T_2} \\ \vdots \\ f_{T_M} \\ f_{WV_1} \\ f_{WV_2} \\ \vdots \\ f_{WV_M} \end{pmatrix}_{2M\times 1}, \tag{2.29}$$

where W is the temperature-weighting function and W' is the WV-weighting function (Noted as W_T and W_{WV} in Eq. 2.24).

State-of-the-art inversion methods and techniques to solve Eq. 2.27 are summarized in Sec. 2.3.2.

2.3.2 Inversion algorithms

The classical MWR inversion algorithms can be divided into the following categories *Janssen* [1993]; *Ulaby et al.* [1986]; *Solheim et al.* [1998]; *Chang* [2001]

- Regularization Methods (RE)
- Iterative Methods (IT)
- *A Priori* Linear Statistical Methods (ST)
- Regression Methods (RG)
- Neural Network based Methods (NN)
- Kalman Filter based Methods (KF)

(RG) Regularization methods were developed in early 1960s and have been used for the atmospheric retrieval problems by for example *Velez-Reyes* [1998]. The method works by applying a controlled smoothing on the solution, and finding a compromise between the weighted least-squares (WLSQ) solution to the RTM and a least-squares departure from the *a priori* guess *Janssen* [1993]. The general quadratic form of the regularization method is given by

$$Q(\boldsymbol{f}) = (\boldsymbol{A}\boldsymbol{f} - \boldsymbol{g}_e)^T (\boldsymbol{A}\boldsymbol{f} - \boldsymbol{g}_e) + \gamma (\boldsymbol{f} - \boldsymbol{f}_0)^T (\boldsymbol{f} - \boldsymbol{f}_0), \tag{2.30}$$

where $\boldsymbol{\epsilon} = \boldsymbol{A}\boldsymbol{f} - \boldsymbol{g}_e$ is the error on the Fredholm integral solution, $\boldsymbol{\eta}_0 = \boldsymbol{f} - \boldsymbol{f}_0$ is the error on the *a priroi* guess, $\boldsymbol{g_e}$ denotes the measurements, $\boldsymbol{f}_0$ is the *a priori* guess and γ is the regularization parameter (always positive).

In Eq. 2.30 above, $Q(f)$ is equivalent to the *objective function*

$$Q(\boldsymbol{f}) = \|\boldsymbol{\epsilon}(\boldsymbol{f})\|^2 + \gamma \|\boldsymbol{\eta}_0(\boldsymbol{f})\|^2, \tag{2.31}$$

where the weighted Euclidean norm of the errors, $\boldsymbol{\epsilon}$ and $\boldsymbol{\eta_0}$, is minimized to obtain the solution using the regularization parameter γ.

The function $Q(\boldsymbol{f})$ when minimized with respect to $\boldsymbol{f}$, yields

$$\hat{\boldsymbol{f}} = \boldsymbol{f}_0 + \boldsymbol{A}^T \left[\boldsymbol{A}\boldsymbol{A}^T + \gamma \boldsymbol{I}\right]^{-1} [\boldsymbol{g}_e - \boldsymbol{A}\boldsymbol{f}_0], \tag{2.32}$$

where $\hat{\boldsymbol{f}}$ is the solution and $\boldsymbol{I}$ is an identity matrix. The accuracy of this solution is dependent upon the accuracy of initial guess.

(IT) Iterative techniques were pioneered by Chahine (1970) and Landweber (1951). A solution $\boldsymbol{f}$ is approached by successive approximations. The general form of linear iterative algorithm is

$$\hat{\boldsymbol{f}}_k = \hat{\boldsymbol{f}}_{k-1} + \boldsymbol{D}\boldsymbol{A}^T \left[\boldsymbol{g}_e - \boldsymbol{A}\hat{\boldsymbol{f}}_{k-1}\right] k = 1, 2, \ldots, \tag{2.33}$$

where $\boldsymbol{D}$ is the matrix given by

$$\boldsymbol{D} = \left[\boldsymbol{A}\boldsymbol{A}^T + \gamma \boldsymbol{I}\right]^{-1}. \tag{2.34}$$

Kadygrov and Pick [1998] have used this technique for the retrieval of temperature profile using measurements by an angular-scanning single-channel microwave radiometer, and have compared the results with *in situ* observations.

(ST) *A priori* statistical methods *Janssen* [1993]; *Ulaby et al.* [1986]; *Chang* [2001] require the time average profile of $\mathbf{f}$ and $\boldsymbol{\epsilon}$ over their ensemble of observations, and their covariances as well, which are given as

$$\begin{aligned} < \boldsymbol{f} > &= E[\boldsymbol{f}] \\ < \boldsymbol{\epsilon} > &= E[\boldsymbol{\epsilon}] \equiv 0 \\ \boldsymbol{S}_f &= E\left[(\mathrm{f}- < \boldsymbol{f} >)\,(\boldsymbol{f}- < \boldsymbol{f} >)^T\right] \quad , \\ \boldsymbol{S}_\epsilon &= E\left[\boldsymbol{\epsilon}\boldsymbol{\epsilon}^T\right] \end{aligned} \tag{2.35}$$

where $\boldsymbol{S}_f$ and $\boldsymbol{S}_\epsilon$ are the covariances of $\boldsymbol{f}$ and $\boldsymbol{\epsilon}$. The expectation is taken over the joint Probability Density Function (pdf) of $\boldsymbol{f}$ and $\boldsymbol{\epsilon}$. The average values and the covariances can be found by using data from RS measurements representative for a given site.

One of the first applications of statistical retrieval methods to retrieve the temperature and humidity profiles from the MWR data was made in 1983 *Hogg et al.* [1983]. The method also provided a framework for the synergy of MWR and radar instruments; the radar data was used as the *a priori* information to calculate the coefficients of the retrieval algorithm. Another attempt was made in 1986, where temperature and WV profiles were retrieved from the MWR data *Askne and Westwater* [1986]. Later on, *Güldner and Spänkuch* [2001]; *Liljegren et al.* [2004] have also used statistical methods for the retrieval of the temperature profile.

Statistical retrieval algorithms incorporating *multi-frequency* and *multi-angle* T_B measurements in linear or higher order terms, along with some auxiliary data, for the study of ABL, have also been used by *Crewell and Löhnert* [2007].

The OEM *Rodger* [2000], which is a combination of the statistical and the iterative methods, is well suited for combining *a priori* information and measurements from multiple sources. A derivative of the OEM called Integrated Profiling Techniques (IPT), which combines measurements from a ground-based multichannel MWR, a cloud radar, a lidar-lidar, RS measurements from the closest station, and measurements of standard meteorological properties with statistics derived from results of a microphysical cloud model, has been developed by *Löhnert et al.* [2004]. IPT has also been used for the retrieval of temperature, WV, cloud Liquid Water Content (LWC) and particularly for the ABL studies *Löhnert et al.* [2008, 2009]. Another variant of OEM, known as 1D-VAR method, was first presented by Hewison (2006) *Hewison* [2006]; *Hewison and Gaffard* [2006]; *Hewison* [2007]. It utilizes short term predictions from the numerical weather prediction model (NWP) instead of RS data, as *a priori* information. 1D-VAR method has been further expanded and used for temperature and WV retrievals by *Cimini et al.* [2010b, 2011]. Another use of OEM to retrieve the temperature profile up to 50 [km] in the stratosphere, has been proposed by *Stähli et al.* [2013].

(RG) Regression methods are based on the application of a set of coefficients on the measurements, to derive a physical quantity of interest. The coefficients can be determined by the previous data records, or data from a collocated instrument. Regression methods have been used by *Güldner and Spänkuch* [2001]; *Solheim et al.* [1998]; *Tan et al.* [2010], along with other methods, for comparison and performance analysis of the retrieval methods.

Recently, another approach has been made towards the retrieval of the ML height, using direct T_B measurements *Cimini et al.* [2013]. This approach uses T_B measurements from the MWR and directly applies a regression coefficients, which have been calculated by the *a priori* information from a collocated lidar data, to retrieve the ML height. The results are then compared with independent lidar-retrieved MLH.

(NN) Similar to the regression methods are the neural networks, whereby the network coefficients are trained by an existing data record. Neural-network-based methods were first used by *Measure et al.* [1992], for the retrieval of atmospheric temperature profiles. Other applications of neural networks can be found in *Churnside et al.* [1994]; *Frate and Schiavon* [1998]; *Crewell et al.* [2001]; *Ware et al.* [2003]; *Chan* [2010].

(KF) Adaptive filtering methods such Kalman filter (KF) have been used in the past for the retrieval of atmospheric temperature profile using MWR data *Ledsham and Staelin* [1978]; *Basili et al.* [1981]. Lately, *Han and Westwater* [1997]; *Basili et al.* [2001] also used KF-based algorithms to retrieve the atmospheric profiles of temperature and humidity. Moreover, *Rocadenbosch et al.* [1998b, 1999]; *Lange et al.* [2014] have used the KF for the retrieval of opto-atmospheric parameters -namely the optical extinction and the backscatter- as well as ABLH from the lidar data.

Some other techniques for the atmospheric profiles (temperature, humidity, IWV) retrieval and comparative studies on retrieval techniques have been discussed in *Troitsky et al.* [1993]; *Trokhimovski et al.* [1998]; *Westwater et al.* [1999]; *Cimini et al.* [2006].

For temperature profiling, the brightness temperature measurements at several frequencies and elevations in the 50-60 [GHz] range (V-band) are correlated *Crewell and Löhnert* [2007]. Consequently, the amount of information corresponding to independent pieces of information, which can be retrieved, is rather low . Considering the RPG HATPRO, when using information from the seven frequency channels as well as elevation scans in the V-band, the DoF comes out to be about four *Löhnert et al.* [2009]; *Löhnert and Maier* [2012]. The low DoF translates to coarse resolution of the retrieved temperature profile which gets poorer as we move up in height. In essence, the retrieved profile, although with high discretization, is rather smooth and thus prone to miss important atmospheric features, in some cases.

2.3.3 Microwave radiometer instrument overview

The function of a radiometer instrument is to receive the brightness intensity in terms of antenna temperature, transduce it in the receiver as detector voltage and then convert the detector voltage to the source brightness temperature through appropriate calibration

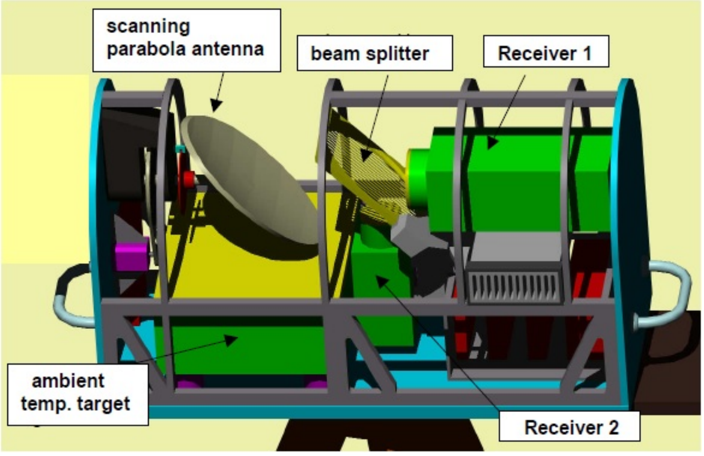

Figure 2.9: Schematic internal structure of RPG HATPRO radiometers *RPG* [2011].

mechanism. The measured source brightness temperature can then be used to retrieve the atmospheric parameters of interest. As an example, Fig. 2.9 shows a schematic layout of the internal structure of a RPG HATPRO MWR. A parabolic scanning antenna collects the incident brightness power from atmosphere and it is split into two through a beam splitter and fed to two receiver chains for further processing. The two receivers correspond to the K (20-30 [GHz]) and V (50-60 [GHz]) bands for temperature and WV retrieval, respectively. There are different types of receiver designs but here we will discuss only the direct detection receiver and the SuperHetrodyne (superhet) receiver, which are the most common type of receiver setups used (RPG HATPRO uses a direct detection receiver design).

2.3.3.1 Receiver systems

Fig. 2.10a shows the schematics of a direct-detection system. A directional coupler is used to inject a precision noise signal. The noise signal is generated by an on/off switching calibrated noise source. The low-noise amplifier (LNA) is used to amplify the input signal before splitting it into 8 channels (currently only 7 are used). Waveguide bandpass filters are used for splitting the input signal.

Fig. 2.10b shows a simple superhet receiver design. A superhet receiver uses the so called heterodyne method in which an incoming radio signal, called RF signal is mixed with a local oscillator signal called, LO signal to create a difference signal at an intermediate frequency, called IF signal. The IF signal is then amplified and filtered to remove the unwanted components. The filtered IF signal is finally fed to a square law detector which converts the current signal into a voltage according to square law. The voltage signal is again amplified and finally the brightness temperature measurement is achieved through the calibration.

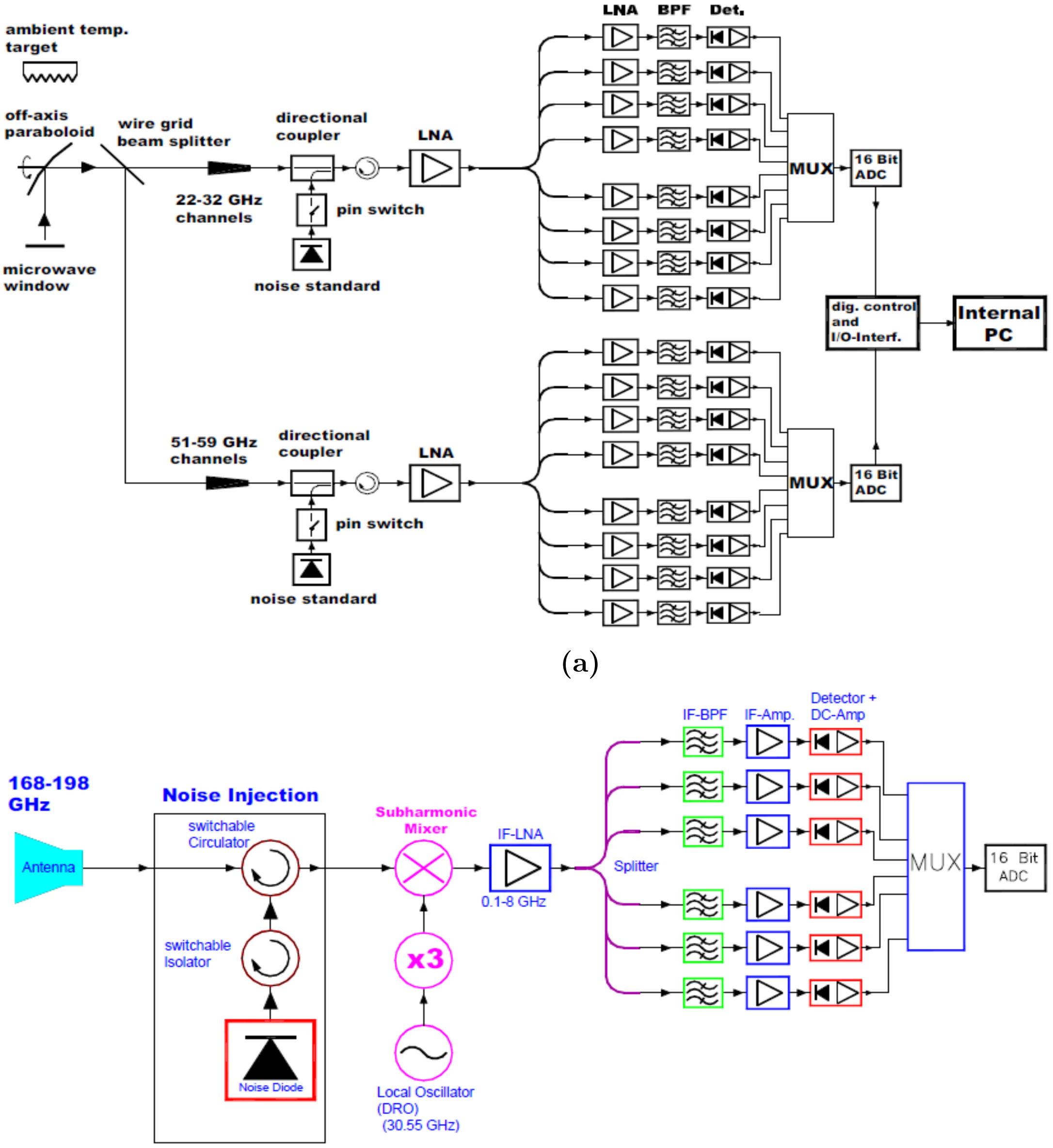

(a)

(b)

Figure 2.10: Commonly used MWR receiver systems *RPG* [2011]. (a) Direct-detection method used in RPG HATPRO systems. (b) Superhet receiver showing all the stages of superhet method.

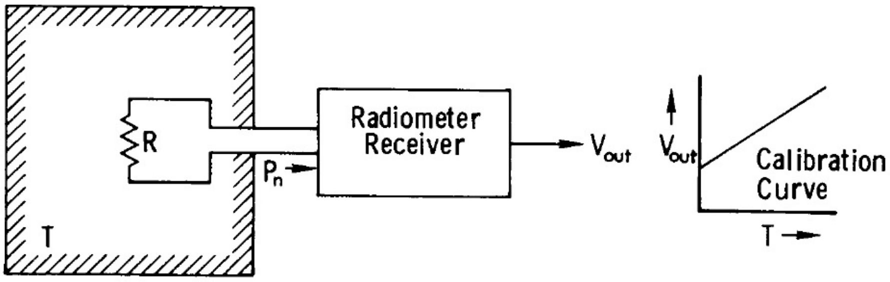

Figure 2.11: Antenna matched resistor inside a blackbody cavity delivers the incident power at antenna via changes in its physical temperature *Ulaby et al.* [1981].

2.3.3.2 Received power and antenna

In order to understand the relationship between the amount of radiation intensity incident at the antenna and the power received, let us consider antenna as a matched resistor which couples the incident energy into the circuit connected to it and vice versa *Janssen* [1993]. Fig. 2.11 shows one such setup whereby an antenna matched-resistor is placed inside a blackbody cavity and acts as a coupler of incident radiation to the receiver circuitry. The amount of incident radiometric power coupled through an ideally non-reflecting and lossless antenna to the circuit in terms of matched-resistor temperature, $T_{incident}$, is given by Johnson-Nyquist's law *Nyquist* [1928b]*Nyquist* [1928a]*Turner* [2007]

$$P_{incident} = kT_{incident}\Delta f. \tag{2.36}$$

k [JK^{-1}] is the Boltzmann's constant, Δf [Hz] is the receiver bandwidth, and $P_{incident}$ [W] is the power incident at the surface of the antenna.

The power incident at the antenna terminal can be determined from the total brightness intensity, $I(\theta,\phi)$ [W $\cdot$ m^{-2} $\cdot$ sr^{-1} $\cdot$ Hz^{-1}], and apparent temperature, T_{AP} [K], which is the brightness-equivalent temperature as seen by the radiometer antenna and includes the contribution from any other sources as well

$$\begin{aligned} P_{incident} &= \frac{1}{2}A_r \iint_{4\pi} I(\theta,\phi)\Delta f F_n(\theta,\phi)d\Omega \\ &= \frac{A_r k \Delta f}{\lambda^2} \iint_{4\pi} T_{AP}(\theta,\phi)F_n(\theta,\phi)d\Omega \end{aligned} \tag{2.37}$$

where A_r [m^2] is the aperture (effective area) of receiving antenna, $F_n(\theta,\phi)$ [.] is the normalized antenna radiation pattern, λ [m] is the wavelength of the incident energy, $d\Omega$ [sr] is the differential solid angle, and $I(\theta,\phi) = \frac{2k}{\lambda^2}T_{AP}(\theta,\phi)$. From Eqs. 2.36 and 2.37 we get the antenna temperature in terms of the apparent temperature

$$T_{incident} = \frac{A_r}{\lambda^2} \iint_{4\pi} T_{AP}(\theta, \phi) F_n(\theta, \phi) d\Omega. \tag{2.38}$$

The antenna aperture and wavelength are related to its radiation pattern through the pattern solid angle, Ω_p, given by

$$\begin{aligned} \Omega_p &= \frac{\lambda^2}{A_r} \\ &= \iint_{4\pi} F_n(\theta, \phi) d\Omega. \end{aligned} \tag{2.39}$$

Combining Eqs. 2.38 and 2.39, we get

$$T_{incident} = \frac{\iint_{4\pi} T_{AP}(\theta, \phi) F_n(\theta, \phi) d\Omega}{\iint_{4\pi} F_n(\theta, \phi) d\Omega}. \tag{2.40}$$

The radiation pattern of a real world antenna is not perfectly directional and hence along with a main-lobe of half antenna bandwidth there are side-lobes as well, which collect the radiation from other sources. The incident antenna temperature can, therefore, be divided into two components i.e. a main-lobe component which is the contribution from the scene of interest and a side-lobe component which comes from other sources.

$$T_{incident} = \frac{\iint_{\text{mainlobe}} T_{AP}(\theta, \phi) F_n(\theta, \phi) d\Omega}{\iint_{4\pi} F_n(\theta, \phi) d\Omega} + \frac{\iint_{4\pi-\text{mainlobe}} T_{AP}(\theta, \phi) F_n(\theta, \phi) d\Omega}{\iint_{4\pi} F_n(\theta, \phi) d\Omega}. \tag{2.41}$$

In an ideal antenna with a narrow beam confined to the main-lobe only, the effective main-lobe apparent temperature can be defined as

$$T_{ML} = \frac{\iint_{\text{mainlobe}} T_{AP}(\theta, \phi) F_n(\theta, \phi) d\Omega}{\iint_{\text{mainlobe}} F_n(\theta, \phi) d\Omega}. \tag{2.42}$$

Using the definition of main-beam efficiency

$$\eta_M = \frac{\iint_{\text{mainlobe}} F_n(\theta, \phi) d\Omega}{\iint_{4\pi} F_n(\theta, \phi) d\Omega}, \tag{2.43}$$

and antenna stray factor

$$\eta_m = \frac{\iint_{4\pi-\text{mainlobe}} F_n(\theta, \phi) d\Omega}{\iint_{4\pi} F_n(\theta, \phi) d\Omega}, \tag{2.44}$$

Eq. 2.41 can be rewritten as

$$\begin{aligned} T_{incident} &= \eta_M T_{ML} + \eta_m T_{SL}, \\ &= \eta_M T_{ML} + (1-\eta_M) T_{SL}, \end{aligned} \tag{2.45}$$

where

$$T_{SL} = \frac{\iint_{4\pi-\text{mainlobe}} T_{AP}(\theta,\phi) F_n(\theta,\phi) d\Omega}{\iint_{4\pi-\text{mainlobe}} F_n(\theta,\phi) d\Omega} \tag{2.46}$$

is effective apparent temperature of the side-lobe contribution.

Real world antennas are lossy and not all the power incident upon their surface is transferred to the underlying receiver stages. The power lost due to Ohmic losses within the antenna is taken into account by defining the radiation efficiency of the antenna

$$\eta_L = \frac{P_{\text{antenna}}}{P_{\text{incident}}}. \tag{2.47}$$

The antenna temperature, T_A, in terms of radiation efficiency and equivalent temperature becomes

$$T_A = \eta_L T_{incident}. \tag{2.48}$$

Now we consider the antenna noise temperature, T_N, which it produces according to Johnson-Nyquist Law by the virtue of its physical temperature T_0. The noise temperature of the antenna in terms of its radiation efficiency and physical temperature is given by

$$T_N = (1-\eta_L) T_0. \tag{2.49}$$

The total received antenna temperature, T_R, which is delivered to the receiver circuitry is then sum of T_A and T_N given by

$$T_R = \eta_L T_{incident} + (1-\eta_L) T_0. \tag{2.50}$$

From Eqs. 2.45 and 2.50 total received temperature can be presented by

$$T_R = \eta_L \eta_M T_{ML} + \eta_L (1-\eta_M) T_{SL} + (1-\eta_L) T_0. \tag{2.51}$$

The quantity of interest in this formulation is T_{ML}, which is the received temperature from the main-lobe of the antenna coming from the scene of interest or target is given by

$$T_{ML} = (\frac{1}{\eta_L \eta_M}) T_R - (\frac{1-\eta_M}{\eta_M}) T_{SL} - (\frac{1-\eta_L}{\eta_L \eta_M}) T_0. \tag{2.52}$$

T_{ML} is linearly related to the total received antenna brightness temperature with a slope of

$(\frac{1}{\eta_L \eta_M})$ and a bias of $-(\frac{1-\eta_M}{\eta_M})T_{SL} - (\frac{1-\eta_L}{\eta_L \eta_M})T_0$.

The received radiation in the form of total received temperature is then converted to a voltage signal by feeding it to a square-law detector. The resulting voltage signal is thus the results of three components which include the source radiation in the form of T_{ML}, side-lobe component in the form of T_{SL} and self radiations of the antenna represented by T_0. Since the relationship between T_{ML}, T_{SL} and T_0 is linear as shown in Eq. 2.52, a simple calibration mechanism can be developed to extract the source brightness temperature.

2.3.3.3 Calibration methods

Following Eq. 2.51, the output of the square law detector which is proportional to the total power fed to it can be represented in the general form given by

$$V_{out} = G T_{ML} + a, \tag{2.53}$$

where G is the total gain and a is the bias term. A simple technique for calibration of the source temperature involves two target sources, one cold and other hot, with known temperature values. Each source is then placed close to antenna in a blackbody container and in the direction of its main beam, thereby resulting in two values of output voltage V_{cold} and V_{hot}. The coefficient G comes out to be

$$G = \frac{V_{hot} - V_{cold}}{T_{hot} - T_{cold}}. \tag{2.54}$$

For cold target liquid Nitrogen is typically used, whereas the hot target is taken to be at room temperature *Janssen* [1993]*Hewison* [2006]*Crewell et al.* [2001]. Recently more advanced techniques for the calibration have been developed *Han and Westwater* [2000]*Schneebeli and Mätzler* [2009]*Maschwitz et al.* [2013] which include tipping-curve method, Kalman filtering method etc. Related to calibration is the subject of errors and bias. A thorough treatment of these topics is covered in *Meunier et al.* [2013]*Cadeddu et al.* [2007]*Hewison* [2006].

2.4 The atmospheric boundary-layer

The development of the ABL over a diurnal cycle is a local phenomenon and shows a typical cycle in clear-sky and low synoptic conditions. During day-time, the ground-surface absorbs solar radiations, and, as a result, near-surface air warms up and starts rising, causing turbulence and a mixing process in the boundary layer. The resulting Convective Boundary Layer (CBL), also called ML, reaches its peak in the afternoon. At the top of CBL, the Entrainment Zone (EZ) acts as a buffer between the CBL and the FT above. During the night, the Earth surface cools radiatively, resulting in a SBL near the surface and

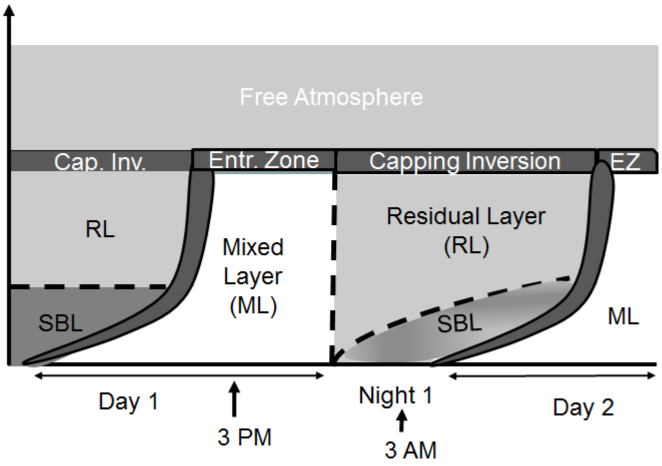

Figure 2.12: A classical model for the development of the ABL over a full diurnal cycle, showing various regimes of the ABL such as ML, SBL and RL. The ML starts developing after sunrise and reaches its peak in the afternoon followed by a quick decrease around sunset (Adapted from Stull,1988 *Stull* [1988]).

an intermittently turbulent Residual Layer (RL) on top of it *Stull* [1988]. The classical development of this phenomenon is shown in Fig. 2.12.

2.4.1 Determination of ABLH

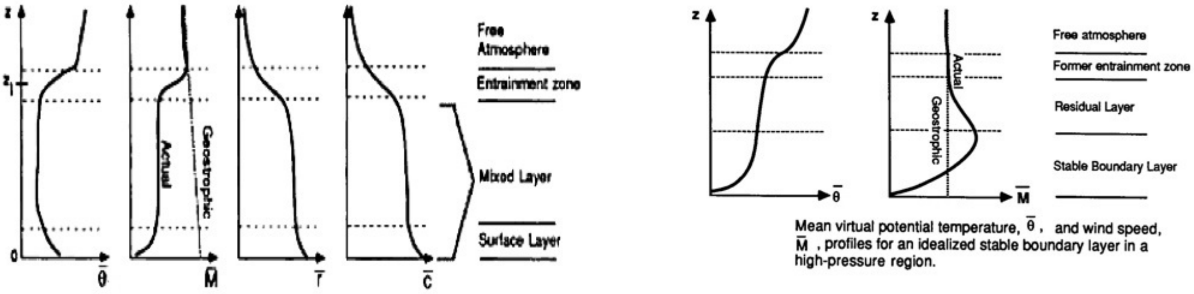

Figure 2.13: Structure of ABL for convective (left) and stable (right) cases with mean profiles of potential temperature, θ, wind speed, m, WV mixing ratio, r, and pollutant concentration, c *Stull* [1988].

The determination of the ABLH is not a straightforward task. Firstly, it depends on the definition of the ABL itself. The common definition of the ABL is based on the turbulence but uncertainties and assumptions are still part of the problem *Seibert et al.* [2000] due to difficulties in identifying the source and magnitude of the turbulence. Secondly, there is no instrument or method which can measure the turbulence, directly and accurately. Instead, as a surrogate, we can measure a proxy or driver of the turbulence. These proxies include *atmospheric temperature profile*, *wind profile*, *energy flux*, and the *profile of the aerosols*. Remote sensing of these parameters, provides a way for the estimation of ABLH.

However, there are always some underlying assumptions. For example, the methods using the temperature profile as the *tracing parameter* for ABL, in essence, give a measure of the *thermally-induced* turbulence. These methods are not well suited for other cases, where the turbulence can be *mechanically-induced*; produced by the frictional drag of the Earth surface as well as the friction between two layers in the atmospheric mass. All of these methods also suffer from the complications of advection *Seibert et al.* [2000]; *Angevine et al.* [2001]; *Angevine* [2008]. Fig. 2.13 shows the structures of different *indicators* of the ABL, as well as, the ABLH based on them. Tab. 2.1 provides an overview of the discussion above, whereby for each indicator its key features, instruments, and their pros and cons are summarized.

2.4.2 ABLH using lidar backscatter

Several methods have been used in the literature to estimate the ABLH using the lidar backscatter data. In general, classical ABLH estimation algorithms can be divided into two categories:

- The *geometrical approach* is based on the existence of a sharp transition or edge between the ML and the FT, in the individual profiles of the ML indicators, i.e., temperature, humidity, wind, and turbulence profiles from *in situ* or remote sensing instruments. A meaningful transition can be detected from the time-averaged profiles by using morphological functions, such as edge detection or gradients.

- The *statistical approach* uses the high variability in the return signal caused by the mixing processes in the EZ; between cells in the EZ and cells in the FT above or in the ML below. This approach requires the analysis of a set of profiles to produce a statistically significant estimate of the MLH, taken as the mean MLH.

Geometrical methods include the threshold method, the gradient method, and the wavelet method. *Statistical* methods include the variance/centroid method. A comparative study of classical methods along with the newly proposed EKF method has been presented in *Lange et al.* [2014]. Therefore, in the following, only a brief summary of these methods is presented.

Threshold method - The threshold method (TM), which is also known as the critical backscatter method, is a simple method in which a threshold value is used to detect the transition between the "high" and the "low" level of the backscatter signal. The transition from higher-to-lower values of the backscatter signal marks the ABL-FT transition, thus identifying the ABLH *Melfi et al.* [1985]; *Batchvarova et al.* [1999]. This method is sensitive to the value of the threshold, which is found by trial and error, as well noise in the backscatter signal. Moreover, *a priori* knowledge of the nominal values of the "high" backscatter level in the ABL and "low" backscatter level in the FT is also required.

Table 2.1: Indicators and instruments used to estimate the ABLH.

Indicator (–)	Instrument (∗)	Pros (•)	Cons (•)
Temperature	– *Temperature as indicator*	• Gives the thermodynamic status of the atmosphere	• Works well only under convective regimes. Detection of ABLH not easy under stable conditions. Multiple inversions often observed
	∗ Radiosonde	• Routinely operated	• Sparse temporal resolution
	∗ Tethered balloon	• Provide *in situ* measurements	• Safety issues, need supervision
	∗ Raman Lidar	• High resolution	• High cost
	∗ MWR	• Continuous measurements 24/7, all weather	• Vertical resolution too coarse beyond 500 [m], to capture temperature inversions
Vertical wind	– *Vertical wind as indicator*	• Direct measurement of vertical motions in the convective and stable boundary layers	• Difficult to measure
	∗ Doppler lidar	• Presence of aerosols needed	• High cost, few measurements currently
	∗ Radar wind profiler	• Continuous operation	• High cost, attribution problem
	∗ Sodar	• Low cost, low minimum range, provides 3D wind field	• Noise pollution, affected by ambient noise
Aerosol	– *Aerosol as indicator*	• Easy to measure with high spatial and temporal resolution	• Presence of aerosol is required Advection or removal complicates the situation
	∗ Ceilometer	• Relatively inexpensive	• Overlap problems for stable layers. Attribution problems
	∗ Research lidars	• Can also measure turbulence by computing the variance of the backscattered signal	• Works well under convective regimes. Need of attended use and analysis
WV	– *WV as indicator*	• Provides almost same results as using aerosols *Hennemuth and Lammert* [2006]	• Difficult to measure remotely Attribution problems
	∗ Raman lidar	• High resolution (space and time)	• Expensive, not operational, needs calibration
	∗ Dial lidar	• Absolute measurement	• Expensive, not operational
	∗ MWR	• Unattended continuous operation, high temporal resolution	• Low vertical resolution, calibration issues, radio interference issues
Radon	∗ Radon meter	• Direct measurement of the status of mixing in the air	• Only *in situ* measurements. Uncertainties related to the radon emission rate
Turbulence	∗ Sodar, wind lidar	• Direct measurement of thermal inhomogeneities at high temporal and spatial resolution	• Low altitude range ($\leq$ 1 km), works well only under stable conditions or weak convection Problems in populated areas

Gradient-based methods - The gradient method (GM) is used to detect the transition from the ABL to the FT by using the gradient (or derivative) of the lidar backscatter profile. ABLH is chosen as the height corresponding to maxima of the first derivative of the backscatter profile. Similarly, another gradient-based method is the logarithmic gradient method (LGM) which utilizes the logrithm of the first derivative to identify the contrast between the ABL and the FT *Martucci et al.* [2004]. The inflection point method (IPM) uses minima of the second derivative of backscatter profile to identify the point of inflection and hence the ABLH. These gradient-based methods still suffer from the random noise fluctuations in the measured backscatter signal and, therefore, different techniques are used to minimize the impact of noise on the estimated ABLH. These techniques include introducing a threshold on the magnitude of the gradient for ABLH identification, smoothing of the backscatter profile using Moving Average (MA) window, and time-averaging of the lidar profiles to average out the random noise. The first two techniques, threshold on gradient and the smoothing using MA window, still suffer from the residual noise due to their arbitrary nature *Flamant et al.* [1997]. The best results are achieved by time-averaging the lidar profile albeit at the cost of reduced time resolution *Menut et al.* [1999].

Variance / centroid method - The variance/centroid method (VCM) relies on the fact that the vertical backscatter profile exhibits a region of maximum variance (the EZ) at the top of the ABL due to updrafts of aerosol-loaded air and downdrafts of clear-air from the FT *Hooper and Eloranta* [1986]. ABLH is defined as the lowest point of maximum variance of the backscatter profile.

Wavelet method - The wavelet method (WM) utilizes the analysis of local gradients using a parametrization in terms of translation and dilation. An example is the Haar wavelet transform which is an edged-shaped function and is well-suited for the detection of local gradients and, consequently, for the identification of ABLH *Cohn and Angevine* [2000]. An improvement over WM is presented in the form of STRAT algorithm *Morille et al.* [2007] which combines a threshold on the Signal-to-Noise Ratio (SNR) with the wavelets of the backscatter signal.

An inter-comparison of the four most commonly used classical methods, i.e., GM, LGM, IPM, and VCM, has been carried out by *Lange* [2014] and it is shown in Fig. 2.14.

Another approach which is a trade-off between geometrical and statistical methods is the use of an adaptive filtering solution based on the KF. The filter estimates the time-dependent profile of an ABL parametric model by combining past estimates of the filter with the actual measurement and basic statistical information on both the atmosphere and lidar-instrument measurement noise.

Extended Kalman method - The EKF-based solution *Lange et al.* [2014] applied to the MLH estimation problem is based on the assumption of a well-mixed convective atmosphere so that the range-corrected backscattered lidar power, $U(z) = z^2 P(z)$ (Eq. 2.8), with z the range, is well approximated by the erf-like profile (Fig. 2.15) *Steyn et al.* [1999].

In the figure, β_{aer} and β_{mol} represent the optical atmospheric aerosol- and molecular-backscatter coefficients, respectively (dependency on z is skipped in the figure for notation simplification purposes). It can be shown that, particularly, towards the near-infrared (NIR) wavelength -as is the case of most ceilometers- or in optically thick atmospheres, the range-corrected lidar signal, $U(z)$, is essentially proportional to β_{aer} (equivalently, the aerosol-mixture number concentration) in the ML, and to β_{mol} (equivalently, the molecular number concentration) in the FT.

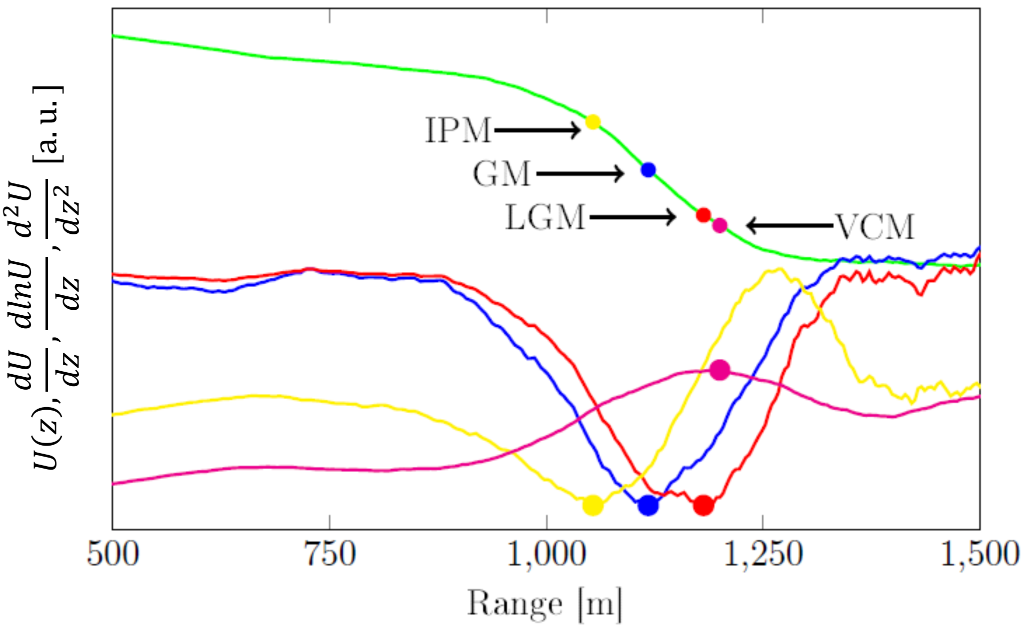

Figure 2.14: Inter-comparison of the four commonly-used classical methods. The figure contains five traces: the range-corrected lidar backscatter, $U(z)$, (green trace), first derivative of $U(z)$, $\frac{dU(z)}{dz}$, (blue trace), second derivative of $U(z)$, $\frac{dU^2(z)}{dz^2}$, (yellow trace), first derivative of the logarithm of $U(z)$, $\frac{dlnU(z)}{dz}$, (red trace), range-dependent variance of $U(z)$ (magenta trace). Corresponding estimates of ABLH are also shown on all the traces *Lange* [2014].

The erf-like profile is modelled by the four parameters of the ML state-vector, which is estimated at each time, t_k, and defined as

$$\boldsymbol{x}_k = [z_{ML,k}, a_k, A_k, c_k]^T, \tag{2.55}$$

where $z_{ML,k}$ is the range position corresponding to the MLH (in what follows, vertical lidar sounding and a horizontally stratified atmosphere can be assumed, so that range is height), a is a scaling factor related to the EZ thickness ($2.77a^{-1}$), A is the total backscatter-coefficient transition amplitude (ML load), c is FT molecular background level, and subindex k is a reminder of discrete time t_k. These four morphological parameters can directly be identified in the erf model of Fig. 2.15.

To sum up, on one hand, all the classical ABLH retrieval methods described above, i.e., the Threshold Method (THM), the Gradient Method (GM), and the Variance Centroid Method (VCM) require reasonable temporal and spatial smoothing on the raw lidar data to reduce noise to acceptable levels, thus, deteriorating the raw-resolution of the data. On the other hand, the EKF adaptively fits the erf-like model-shape function (for the ABL) to the lidar-measured data and minimizes the mean-squared error over time in a statistical sense. The filter, thus, makes the most from the high temporal resolution of curve-fitting geometrical models and the physically-significant estimates output by statistical methods

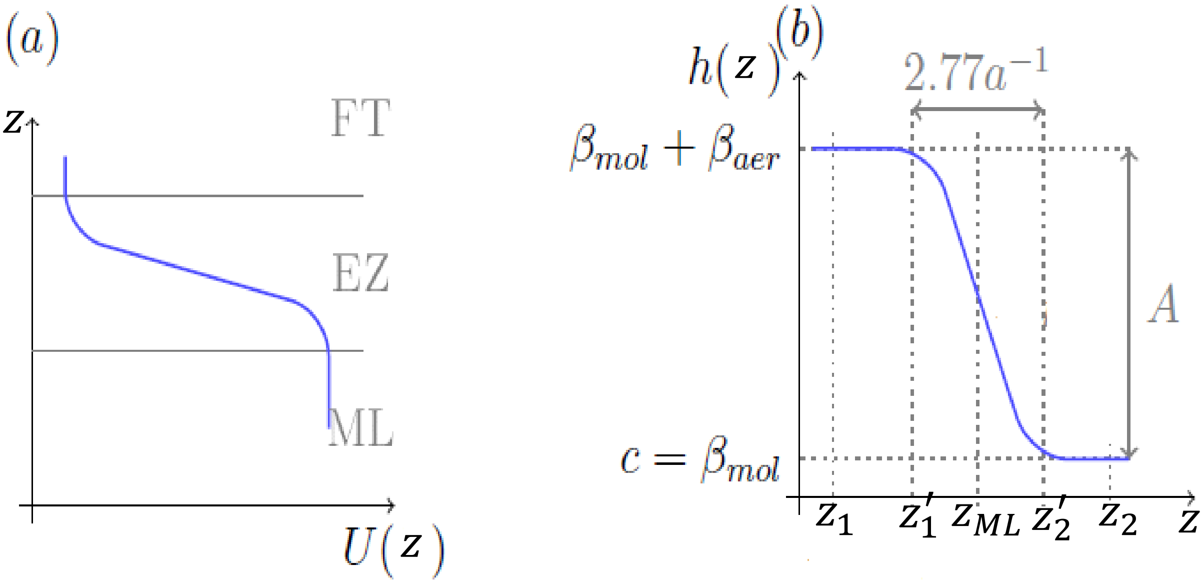

Figure 2.15: Simplified/idealized description of the ML. (a) In the ML model, $U(z)$ is the range-corrected idealized (noiseless) lidar signal. (b) Idealized ML erf-curve transition model, $h(z)$, for the total backscatter coefficient with characteristic parameters, z_{MLH}, a, A, and c. z_1 and z_2 are the start- and end-range limits defining the length of the observation vector passed to the filter. $z_1^{'}$ and $z_2^{'}$ are the start-range and end-range limits of the erf-like ML transition. (Adapted from *Lange et al.* [2014]).

without compromising the raw-resolution of the data.

2.4.3 ABLH using MWR-retrieved temperature

In contrast to lidar, the MWR is not only able to retrieve the vertical profile of atmospheric temperature but also to capture low-height nocturnal temperature inversions. Therefore, it is suitable for for both retrieval of the day-time MLH and the night-time SBLH. However, the resolution of the retrieved-temperature profile is poor and decreases significantly with height.

The most commonly available ABLH (MLH as well as SBLH) estimation methods based on MWR-retrieved temperature data in the literature are summarized below.

2.4.3.1 MLH estimation using MWR-retrieved temperature

Parcel method - The parcel method (PM) *Holzworth* [1964] is based on the thermodynamic stability of the atmosphere. For a given profile of physical temperature, $T(z)$ [K], retrieved from brightness temperature measurements, the MLH is the point for which $\theta(z) \geq \theta_0$, where θ_0 is the surface value of the potential temperature. Though parcel method is a simple and commonly used method for MLH retrieval, it does not provide any information on the uncertainties associated to the MLH estimates. Fig. 2.16a shows an example of parcel method applied on MWR-retrieved potential temperature profile from 18.04.2013, 14:01 [UTC], Jülich, Germany.

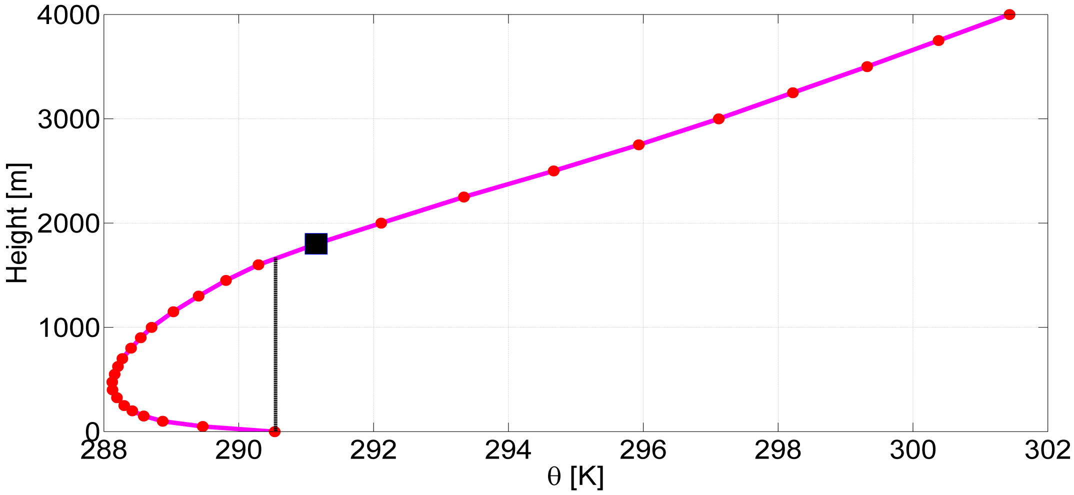

(a)

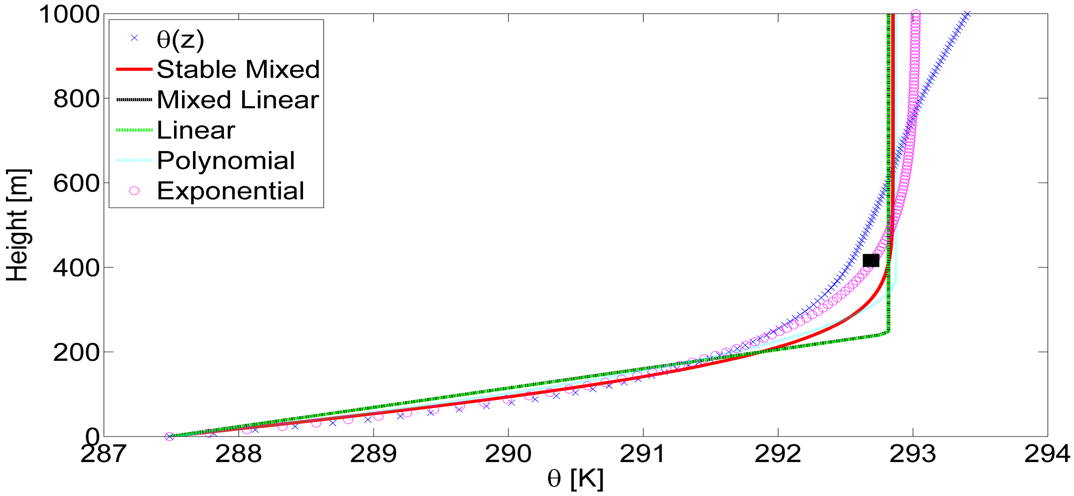

(b)

Figure 2.16: ABLH from MWR-retrieved temperature data. (a) Day-time MLH using parcel method on a MWR-retrieved potential temperature profile. The estimated MLH is set as the first point on height-grid when the atmospheric potential temperature is equal to or higher than the surface potential temperature. (b) SBLH using five physical models applied on MWR-retrieved potential temperature profile. The best fitting, in terms of Minimum Mean-Square Error (mMSE), is achieved by the exponential model.

Bulk Richardson method - The Bulk Richardson (bR) method uses the gradient of the potential temperature and horizontal wind components to compute a turbulence indicator, Ri_b *Garratt* [1992].

$$Ri_b = \frac{gz\left(\theta(z) - \theta(z_0)\right)}{\overline{\theta}\left(U^2(z) + V^2(z)\right)}, \tag{2.56}$$

where $\overline{\theta}$ is the mean value of z_0 and z, and U and V are the two horizontal components of the wind. The ABLH is determined as the first elevation level where Ri_b exceeds a critical value (0.15-0.40) *Jeričević and Grisogono* [2006]. For the critical value set to 0, bR method becomes identical to PM method.

2.4.3.2 SBLH estimation using MWR-retrieved temperature

Idealized physical models - Five idealized physical models for the stable boundary-layer temperature profile are available in the literature *Stull* [1988]. These five models include stable-mixed, mixed-linear, linear, polynomial and exponential models (details in Chap. 4, Sect. 4.1.2). For SBLH estimation, on a given temperature profile these five models are fitted by using a Least-SQuares (LSQ) approach. The best fitting model is chosen as the one which fits with the minimum Root-Mean-Square Error (RMSE). Fig. 2.16b shows an application of the five idealized physical models on a MWR-retrieved potential temperature profile from 24.04.2013, 21:00 [UTC], Jülich, Germany.

Gradient method - Recently, a temperature gradient-based method for the retrieval of SBLH has been presented by *Collaud Coen et al.* [2014]. SBLH is chosen as minimum height where gradient of the MWR-retrieved potential temperature is minimum, thus, signifying transition from the SBL to the RL.

All of these methods, while providing thermodynamically consistent estimates of the ABLH, suffer from high uncertainties due to the poor resolution associated to the MWR-retrieved temperature data. Key features of some of the ABLH estimation methods based on lidar and MWR data are summarized in Table 2.2. An important point to notice is that different methods can output different ABLH estimates with different errorbars (if, at all, available) at a given location and time. The reason for this disagreement can be attributed to inconsistency between the indicators (e.g., potential temperature profile vs. aerosol concentration profile) *Seibert et al.* [2000]; *Hoff et al.* [2012]; *Illingworth et al.* [2013]. Moreover, the minimum altitude for reliable detection associated with the instrument and sounding techniques, is also a limiting factor.

Table 2.2: Overview of the ABLH estimation methods.

Method	Indicators	Instruments	Characteristics
Parcel Method (PM) *Holzworth* [1964]; *Fisher and Thomson* [1998]	• Temperature	• RS, MWR	• PM works by following a dry adiabatic line from the surface temperature until it intersects the measured temperature profile • Computes the height to which an air packet at the ground will adiabatically rise (neglecting advection, subsidence and air humidity)
Bulk Richardson Number Method (bR) *Praz* [2013]; *Fisher and Thomson* [1998]; *Jeričević and Grisogono* [2006]; *Szintai* [2010]	• Temperature, horizontal wind components	• RS, MWR	• Uses the gradient of the potential temperature and horizontal wind component to compute a turbulence indicator, bR. • The ABLH is determined as the first elevation level where bR exceeds a critical value (0.15-0.40) • For the critical value set to 0, bR becomes identical to PM method.
Gradient method (GM), Logarithmic gradient method (LGM), Threshold method (THM), Inflection point method (IPM), Centroid/variance method (VCM), Wavelet method (WM), STRAT method *Martucci et al.* [2004]; *Melfi et al.* [1985]; *Hooper and Eloranta* [1986]; *Cohn and Angevine* [2000]; *Haeffelin et al.* [2012]; *Morille et al.* [2007]	• Backscatter profile	• Backscatter lidar, ceilometer	• Are based on the fact that a high concentration of well mixed aerosols exist in the ML, whereas a significantly lower concentration of aerosols is found in the FT • Given this sudden change in concentration, the ABLH is determined using different derivative and morphological variants: GM, LGM, THM, IPM, VCM
EKF based Method *Lange et al.* [2014]	• Backscatter profile, Temperature	• Backscatter lidar	• ABLH is estimated by means of an adaptive procedure combining present and past estimates, given the backscattered lidar signal profile, ABL shaping model, and covariance information • Successful ABLH estimation using backscatter lidar signals

2.4.4 Motivation for synergy

Considering the lidar and the MWR, both instruments have their own strengths and limitations, as shown in Tab. 2.3. By comparison, it becomes clear that a synergetic method which exploits the strengths of the two instruments is expected to provide physically consistent and highly-resolved estimates of the ABLH with low uncertainty.

Table 2.3: Strengths and limitations of lidar and MWR instruments for ABLH estimation.

Lidar	MWR
(+) Provides *highly-resolved* (spatial: 25 [m] on average, temporal: from seconds to a couple of minutes) estimates of the ABLH.	(+) Provides *physically consistent* estimates of ABLH since temperature is closely related to the actual thermodynamic state of the atmosphere.
(+) ABLH estimates are *consistent with RS* only under well-mixed atmospheric conditions.	(+) *Good temporal resolution* (a couple of minutes, typically).
(-) *Lacks physical consistency*, meaning aerosols under certain atmospheric conditions are not reliable indicators of the ABLH, especially at night and during morning/evening transitions times.	(+) Is able to *follow the nocturnal SBLH* and morning/evening transitions reasonably well.
(-) *Limited* in cloudy and rainy conditions.	(+) Can work under *cloudy and rainy conditions*, in principle.
(-) *Incomplete overlap* (several hundred meters for bi-axial systems).	(-) Is limited by the *high spatial uncertainty* (400 [m] on average) associated to the ABLH estimates.

2.5 Conclusions

This chapter has summarized the basic principles of lidar and MWR remote sensing with focus on ABLH retrieval. Sect. 2.2 has revisited the elastic lidar equation along with the concepts of extinction and backscatter coefficients from the perspective of the ceilometer instrument. Sect. 2.3 has reviewed the foundations of the RTM from MWR brightness temperature measurements and its related instrument architecture. Finally, Sect. 2.4 has presented the ABLH in the context of the diurnal cycle and it has briefly outlined different ABLH estimation methods from the lidar and the MWR perspective.

Chapter 3

Daytime mixing-layer and morning/evening transition boundary-layer

This chapter reviews the estimation of daytime MLH and morning/evening transition boundary-layer height. Special attention has been paid to the analysis of uncertainties associated to the estimation of MLH from lidar and MWR data, as well as highlighting the strengths and limitations of the two instruments. In this context, a simple synergetic MLH estimation method is presented along with a first test of its operation.

The contents of this Chapter are part of the papers *Saeed and Rocadenbosch* [2016a] submitted to IEEE Transac. Geosc. Rem. Sensing, and *Saeed et al.* [2015b] published in Proc. of SPIE, 2015. Systematic or multiple reproduction or distribution to multiple locations via electronic or other means is prohibited and is subject to penalties under law.

3.1 Introduction

There are several ground-based instruments and methods for the estimation of MLH. Some of the commonly used instruments include active ones such as the lidar, the radar, and the sodar, and passive ones like the MWR. The EKF is a recent and robust method for MLH estimation *Lange et al.* [2014] using backscattered lidar signals. The parcel method *Holzworth* [1964] is commonly used with MWR-retrieved potential temperature data.

Most of the previous work done for MLH retrieval using backscattered lidar signals or temperature data has been focused on retrieval methods only *Haeffelin et al.* [2012]; *Lange et al.* [2014]; *Cimini et al.* [2013]. However, the uncertainty associated to the estimated MLH has not been paid much attention. Hence, the impact of instrumental measurement errors and retrieval errors on MLH estimates needs to be assessed for the purpose of comparison and reliability of the instruments and methods.

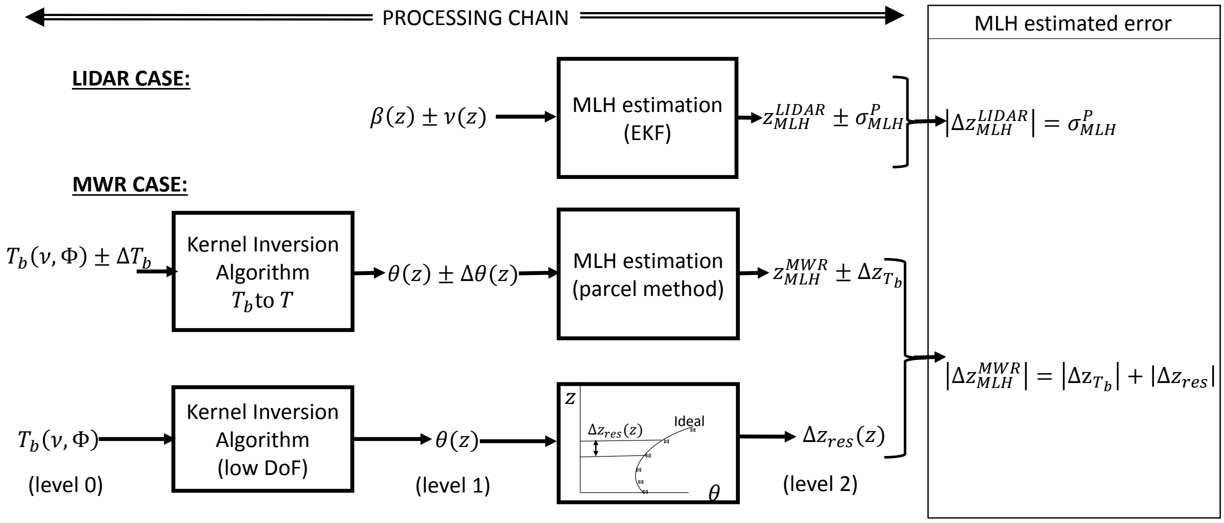

Figure 3.1: Block diagrams illustrating the lidar- and MWR-processing chains used to estimate the MLH and related errors. Top and bottom diagrams stand for the lidar and MWR instruments, respectively. $\beta(z)$ is the attenuated backscatter, $\nu(z)$ is the related corrupting noise, z_{MLH}^{LIDAR} is the lidar-EKF estimated MLH, σ_{MLH}^{P} is the estimated MLH error. $T_b(\nu, \phi)$ is the MWR brightness temperature measured at frequency ν and elevation angle ϕ, $\theta(z)$ is the retrieved potential-temperature profile, Δz_{T_b} is the MLH error component due to brightness temperature errors, ΔT_b, Δz_{res} is the MLH error component due to coarse vertical resolution in the brightness-temperature-to-absolute-temperature retrieval process. z stands for the vertical range. Δz_{MLH}^{LIDAR} and Δz_{MLH}^{MWR} stand for the total estimated error on the MLH for the lidar and MWR instruments.

In this chapter, we aim to study the impact of measurement and retrieval errors on MLH estimates from ground-based lidar and MWR instruments by using EKF estimation and parcel-method schemes, respectively, as well as the potentialities of both instruments for MLH retrieval. The simplified processing chain of Fig. 3.1 is considered.

Concerning the lidar sensor, the noise-corrupted backscattered lidar signal (level-0 product) is background-subtracted and range-corrected (level-1) *Measures* [1992] before the MLH is estimated (level-2). In the lidar case, assessment of MLH estimation errors is, in principle, simpler than for the MWR because MLH lidar-estimation algorithms always depart from the clean range-corrected data (level-1) to estimate it. As a result, the error-propagation law in response to noisy lidar raw data is dictated by the MLH estimation algorithm. In the present application, an EKF estimator is used for this purpose and it will be seen in Sect. 3.2.1 that this estimator provides a convenient way to assimilate measurement errors via covariance matrix information *Rocadenbosch et al.* [1999]; *Lange et al.* [2014].

In the case of the MWR, brightness-temperature measurements (level-0 product) are converted into a potential-temperature profile (level-1) by means of a statistical retrieval algorithm *Löhnert and Crewell* [2003]; *Crewell and Löhnert* [2003] and auxiliary atmospheric temperature and pressure data. Ultimately, the retrieved potential-temperature profile is used to estimate the MLH (final level-2 product).

For the purpose of MLH estimation from MWR measurements at least two different types of error sources can be outlined *by origin*: (i) MLH errors originating as *brightness-temperature measurement errors* (ΔT_b in Fig. 3.1), which account for random errors associated to instrumental thermal (Johnson) noise and systematic errors (e.g., biases and calibration offsets) *Löhnert and Maier* [2012]. Crewell et. al. (2007) *Crewell and Löhnert* [2007] have successfully assessed the impact of brightness temperature measurements on the retrieved absolute temperature atmospheric profile. Since, as mentioned, the MLH is directly estimated from the temperature profile (in fact, converted into a potential temperature profile, $\theta(z)$), errors on the retrieved temperature profile need to be related to the uncertainty on the estimated MLH. All considered, brightness-temperature errors incur an error Δz_{T_b} in the estimated MLH. And (ii) MLH errors originating as *retrieval errors* (i.e., errors associated to the brightness-temperature-to-absolute-temperature retrieval algorithm), which roughly show up as a decreasing spatial resolution with height. Ultimately, this is a consequence of the low DoF -or correlation- among the different frequencies and elevation-scanned profiles. In what follows, and for the purpose of this work, this kind of errors will simply be called *resolution errors* because they ultimately translate into a resolution uncertainty in the estimated MLH $\big(\Delta z_{res}(z)\big)$.

When comparing both instruments, on one hand, lidar sensors have better spatial resolutions (e.g., 15 [m] for Jenoptik CHM 15k Nimbus ceilometer). Yet, because they rely on attenuated backscatter returns from the atmosphere (i.e., intensity echoes) they lack physical consistency with the thermodynamic state of the atmosphere. On the other hand, MWR sensors have a much poorer vertical resolution (evidenced by a typical discretization of 50-to-250 [m] from ground level up to 4 [km] in height for a HATPRO MWR). In contrast, because the MWR measures brightness temperatures, which are consequence of atmospheric blackbody radiation, these measurements are physically consistent with the true thermodynamic state of the atmosphere. In this context, a synergetic MLH estimation combining data from the two instruments is motivated and a first test of a simple synergetic approach is presented.

3.2 Overview of MLH estimation: Lidar- and MWR- observation cases

3.2.1 Lidar MLH-estimation method

There are different methods and approaches for MLH estimation using lidar backscatter data. Classical methods such as the gradient method *Endlich et al.* [1967]; *Flamant et al.* [1997], the inflection point method *Menut et al.* [1999], the variance method *Hooper and Eloranta* [1986], and the threshold method *Melfi et al.* [1985]; *Boers and Eloranta* [1986] are either based on the geometry of the profile or the statistics of a set of profiles. All of these methods require some form of averaging to improve the SNR which means that temporal resolution of the MLH estimates is usually low (typically, 30-min). These classical methods, therefore, try to average out the random noise. In contrast, the EKF-based MLH estimation method *Lange et al.* [2014, 2015], which departs from previous works of *Rocadenbosch et al.* [1998b, 1999], does not require averaging of the profiles to improve SNR. Instead, it assimilates noise statistics into the noise covariance matrix to provide optimal estimation. Therefore, the original resolution of the data is preserved.

In the following, a summary of the EKF method for MLH estimation from lidar backscatter data is presented *Lange et al.* [2014]:

The ground of adaptive estimation is to model the phenomenon under study (in this case the ML) with a set of appropriately chosen parameters, the so-called the state-vector, and which are allowed to change with time. Its roots come from the military industry in which the $\left[x(t_k), y(t_k), z(t_k)\right]$ coordinate position of a target plane at discrete time t_k is to be acquired and tracked with time from e.g., a missile, with minimum least-squared error over time.

In the UPC KF solution applied to MLH estimation, a convective atmosphere is assumed so that the range-corrected backscattered lidar power, $U(z)$, with z the range, is well approximated by the erf-like profile of Fig. 2.15 (Chap. 2, Sect. 2.4).

The EKF is based on two main models, namely, the *state-vector model* and the *measurement model* along with related covariance matrices.

The *state-vector model* is representative of the transition of state-vector from time t_k to t_{k+1}. It is approximated by a simple Gauss-Markov model of the form

$$\boldsymbol{x}_{k+1} = \boldsymbol{x}_k + \boldsymbol{w}_k, \tag{3.1}$$

where $\boldsymbol{w}_k$ is the state-noise vector with diagonal covariance matrix modelled as $\boldsymbol{Q}_k = diag[\sigma^2_{z_{MLH}}, \sigma^2_a, \sigma^2_A, \sigma^2_c]$ with σ_x, x=z_{MLH}, a, A, c representing “guessed” standard deviations associated to the state-vector components, z_{MLH}, a, A, and c, which are approximately input from the user’s side.

The measurement model relates the lidar measurement vector, $\boldsymbol{z}_k$, with the state-vector,

$$\mathbf{z}_k = h(\boldsymbol{x}_k) + \boldsymbol{v}_k, \tag{3.2}$$

where h is the erf-like ML-to-FT transition model, given by

$$h(z; z_{MLH}, a, A, c) = \frac{A}{2}\left\{1 - erf\left[\frac{a}{\sqrt{2}}(z - z_{MLH})\right]\right\} + c, \tag{3.3}$$

and $\boldsymbol{v}_k$ is the observation noise at time t_k and z is the vertical range. The observation noise, $\boldsymbol{v}_k$, is modelled by its noise covariance matrix, $\mathbf{R}_k$ (See [Barlow, 1999, p. 215]). The nonlinear model of Eq. 3.3 is linearized through its Jacobian and passed to the filter.

The input to the EKF ($\mathbf{z}_k$ in Eq. 3.2) is the noisy range-corrected background-subtracted backscattered lidar signal, $U'(z) = z^2 P'(z)$ or, equivalently, the noisy attenuated backscatter coefficient measured by the ceilometer, $\beta'(z)$, if $U'(z)$ is scaled by the ceilometer system constant (see details in Eq.(3) [Lange et al., 2014]). For conceptual reasons, we will use here the term "attenuated backscatter" instead of "range-corrected power".

The noise term, $v(z)$, in Eq. 2.11 assimilates into a single body different types of noises, namely, photo-induced-signal shot noise, dark shot noise, and thermal noise. However, if the count numbers are high enough ($>$ 50 counts/s) -as it is usually the case- and according to the central-limit theorem *Barlow* [1989a], the statistics of $v(z)$ can be modelled as equivalent Gaussian process (App. A in *Rocadenbosch et al.* [1998a]).

3.2.2 MWR MLH estimation method

The parcel method is normally used for MLH estimation using potential temperature data *Holzworth* [1964]. This method is based on the thermodynamic stability of the atmosphere. For a given profile of physical temperature, $T(z)$ [K], retrieved from the brightness measurements, the first step is to convert it to a potential temperature profile, θ(z) [K], using

$$\theta(z) = T(z) \left(\frac{p_0}{p(z)} \right)^{\frac{R}{C_p}}, \tag{3.4}$$

where $R = 287 \left[\mathrm{J} \cdot \mathrm{K}^{-1} \cdot \mathrm{kg}^{-1} \right]$ is the universal gas constant, and $\mathrm{C_p} = 1004 \left[\mathrm{J} \cdot \mathrm{K}^{-1} \cdot \mathrm{kg}^{-1} \right]$ is the specific heat capacity at a constant pressure, thereby, $\frac{R}{C_p}$ is 0.286 [$\cdot$] *Wallace and Hobbs* [2006].

The potential temperature profile, θ(z), is then followed from the surface along the vertical direction and any changes in θ(z) with respect to height, $\frac{d\theta(z)}{dz}$, are indicative of the stability of the atmosphere as follows: The atmosphere is stable when $\frac{d\theta(z)}{dz} > 0$, neutral when $\frac{d\theta(z)}{dz} = 0$, and unstable when $\frac{d\theta(z)}{dz} < 0$.

Since the mixed layer during day-time is characterized by continuous surface driven convective mixing, it is an unstable atmosphere and, hence, $\frac{d\theta(z)}{dz} < 0$. The height of the ML is the point in a given potential temperature profile for which $\theta(z) \geq \theta(0)$ where $\theta(0)$ is the surface value of the potential temperature. However, since the potential temperature profile from MWR measurements is subject to errors, there is an range of uncertainty associated with the MLH estimated by the parcel method. In order to determine this uncertainty, measurement and retrieval uncertainties associated to the potential temperature profile must be taken into account.

3.3 The need of a synergetic MLH retrieval method

3.3.1 Uncertainties on MLH estimation from lidar and MWR data

3.3.1.1 Lidar-retrieved MLH error estimation

The recursive loop of the EKF provides by itself convenient error estimates for the estimated state vector and, therefore, for the estimated MLH at each discrete time t_k. These approximate error estimates are obviously subordinated to filter convergence.

In detail, the uncertainty associated to the initial state-vector guess is supplied by the user in the form of the *a priori* error-covariance, matrix, $\mathbf{P}_0^-$,

$$\mathbf{P}_0^- = E\left[\mathbf{e}_0^- \mathbf{e}_0^{-T}\right], \tag{3.5}$$

where $e_0^- = x_0 - \hat{x}_0^-$ the *a priori* error (here, x_0 represents the true atmospheric state (unknown) and $\hat{x}_0^-$ is the initial state-vector estimated by the user).

A priori and *a posteriori* error covariance matrices (i.e., "previous" to and "after" assimilating the current measurement, $\mathbf{z}_k$) are updated at each successive time instant during the EKF processing cycle as a function of the current information available to the filter (actual Kalman gain or projection gain, linearised Jacobian, and state-vector- and noise-covariance matrices).

Of importance is correct estimation of the measurement noise. Towards this end, the observation or measurement noise, v_k, is taken into account through the noise-covariance matrix,

$$\mathbf{R}_k = E\left[\mathbf{v}_k \mathbf{v}_k^T\right], \tag{3.6}$$

where $E(.)$ is the expectancy or ensemble operator. The N-component vector, $\mathbf{v}_k$, ($v(z)$ in Eq. 2.11 analog form) corresponds to heights $1, \ldots, N$. To estimate the noise-covariance matrix at each successive t_k we assume a main diagonal matrix, where each element along the diagonal represents the noise variance along the vertical range dimension (i.e., height), and we use the methodology exposed in [Lange et al., 2015, Sect. III. C]. Here, ergodicity is used to estimate the time statistics of noise (which requires an ensemble of time observables) by means of the spatial statistics along adjacent height intervals of the current measurement (which requires just the current observable, instead).

Fig. 3.2 shows the *a priori* error, *a posteriori* error, and state-noise estimated variances computed as the standard deviation of these variables as a function of time ($\sigma_{MLH}^{P^-}$, σ_{MLH}^{P}, σ_{MLH}^{Q}, respectively) from Jenoptik CHM 15k Nimbus ceilometer measurements on 18.04.2013 at Jülich, Germany. The *a priori* error always remains slightly higher (or very close to as time goes on) than the *a posteriori* error meaning that the error reduces with each

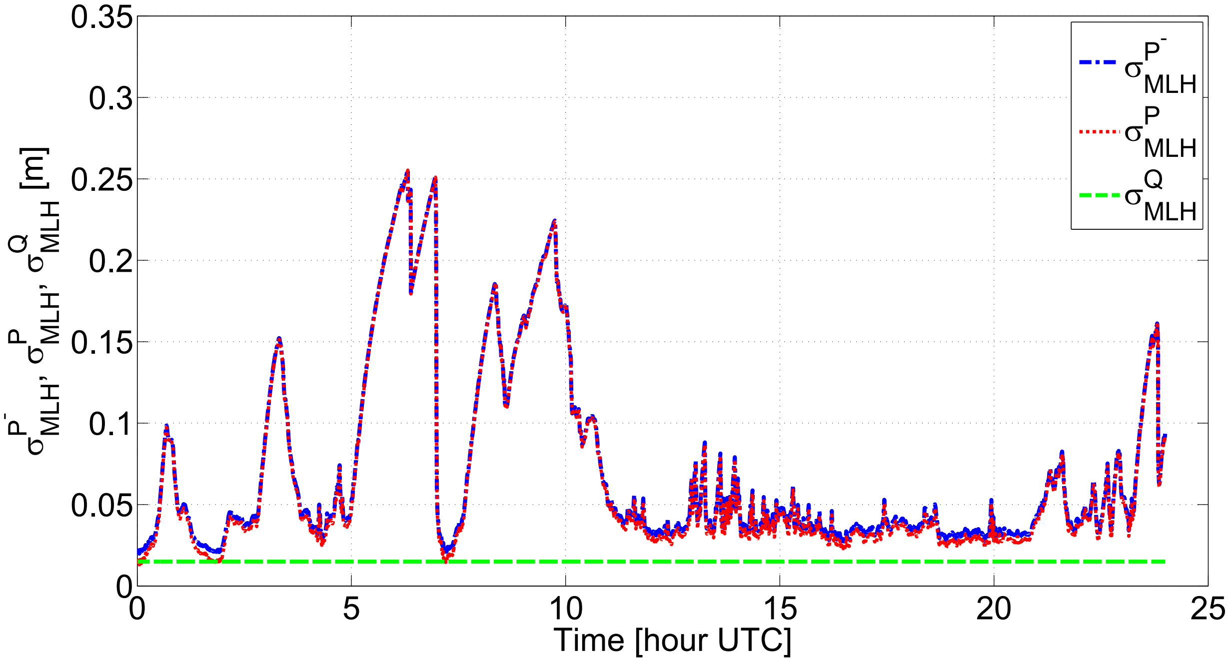

Figure 3.2: Lidar-EKF estimated MLH error as a function of time. $\sigma^{P^-}_{MLH}$, σ^{P}_{MLH}, σ^{Q}_{MLH} stand for the estimated *a priori* error, *a posteriori* error, and state-noise standard deviations on the MLH, respectively. Case study: 18.04.2013, Jülich, Germany.

new measurement assimilated. These error indicators approach at specific time intervals the lower bound σ^{Q}_{MLH}, representative of the estimated atmospheric MLH variability.

3.3.1.2 MWR-retrieved MLH error estimation

The uncertainty associated to the MLH estimates from MWR has two underlying error sources that include: (i) the instrumental uncertainty due to the *brightness-temperature measurements* and consequent propagated errors on the retrieved potential temperature, Δz_{T_b}, and (ii) the uncertainty due to the *coarse vertical resolution* (a consequence of the low DoF in the measurement data *Löhnert et al.* [2009]; *Löhnert and Maier* [2012]) of the retrieved potential temperature profiles, Δz_{res}. Fig. 3.1 depicts a block-diagram representation of these two error sources and their propagation to the final MLH estimate, which is discussed next:

Assessment of brightness-temperature errors on the estimated MLH, Δz_{T_b} - A study on the impact of measurement errors on the retrieved temperature profile has been done by Crewell et al. (2007) by using a statistical retrieval algorithm trained on a long-term dataset of representative atmospheric profiles *Crewell and Löhnert* [2007]. A synthetic brightness-temperature dataset was used to test the performance of the retrieval algorithm that, in response, output altitude-dependent temperature uncertainties, $\Delta T(z)$, which varied from 0.44 [K] on the ground to 1.60 [K] at 4 [km].

In order to study the uncertainty on MLH estimates due to temperature retrieval errors, Δz_{T_b}, we adopt the following approach: At each time instant, retrieved height-dependent

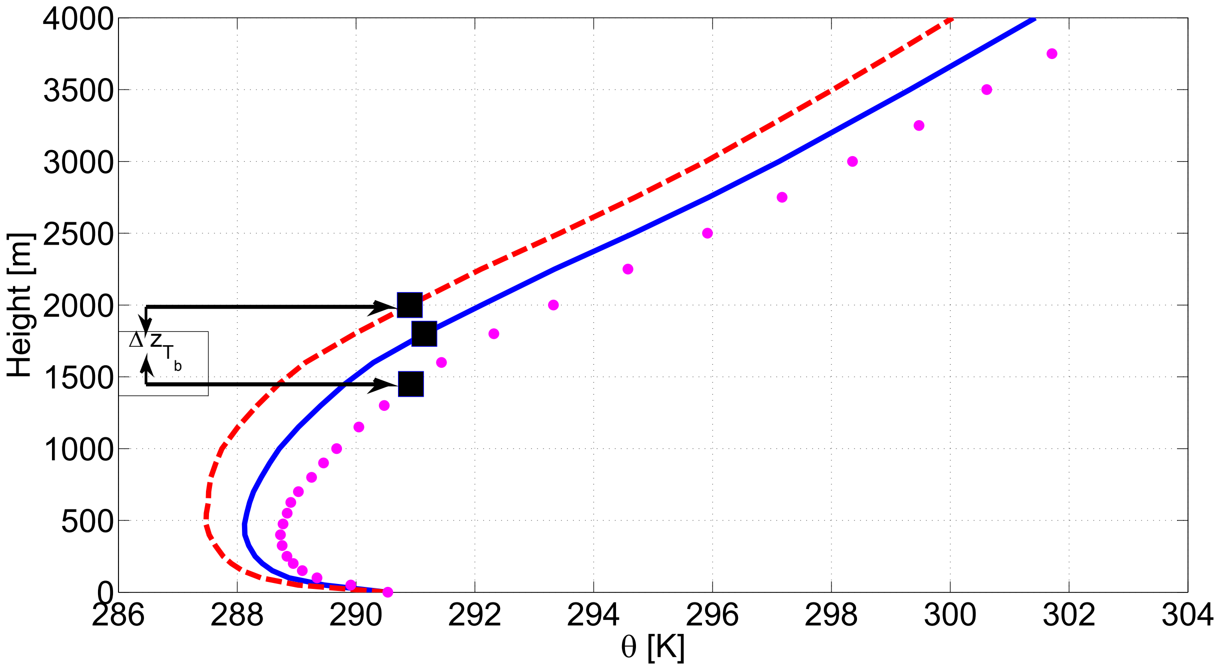

Figure 3.3: Estimation of the MLH error due to brightness-temperature measurement errors, Δz_{T_b}. Upper (dashed)- and lower (dotted)-bound profiles are obtained by adding and subtracting the height-dependent temperature error-perturbation profile, $\Delta\theta(z)$, to the nominal potential-temperature profile, $\theta(z)$. Black squares indicate the estimated MLH for each profile according to the parcel method. Measurement data from 18.04.2013, 14:01 UTC, Jülich, Germany.

temperature errors, $\Delta T(z)$, or equivalently, potential-temperature errors -in our case-, $\Delta\theta(z)$, are added and subtracted to/from the given potential temperature profile resulting in "upper" and "lower" bounds. Parcel method is then applied to the three perturbed profiles of such potential temperature profile (Fig. 3.3): (i) $\theta_{MWR}(z)+\Delta\theta(z)$ or upper error-bound profile for the potential temperature, (ii) $\theta_{MWR}(z)$ or nominal profile, and (iii) $\theta_{MWR}(z)-\Delta\theta(z)$ or lower error-bound profile. Three independent estimates for the MLH are derived from the three profiles and hence an error-bar for the MLH is obtained. Fig. 3.3 shows error-bar calculation for the temperature profiles retrieved from measurements on 14:01 UTC, 18.04.2013 using the HATPRO MWR at Jülich, Germany. It can be observed that retrieval errors on the order of less than 2 [K] throughout the vertical profile introduce an uncertainty of about 300 [m].

Assessment of vertical resolution errors on the estimated MLH, Δz_{res} - Along with measurement errors, MWR-based temperature retrieval suffers from the limited information content within the measurements. Measurements at several frequencies and angles are correlated meaning the DoF of the data is low and, therefore, the retrieved temperature profiles have coarse vertical resolution.

The discretization grid of Tab. 3.1, which has been used for the retrieval of temperature profiles in this work, increases with height in accordance with the true decreasing vertical resolution of the temperature retrievals from the instrument. Therefore, for simplicity, Δz_{res}

Table 3.1: Discretization of vertical temperature retrieval grid upto 4 [km].

Height [m]	Discretization step [m]
$0 \leq z \leq 250$	50
$250 < z \leq 700$	75
$700 < z \leq 1000$	100
$1000 < z \leq 1600$	150
$1600 < z \leq 2000$	200
$2000 < z \leq 4000$	250

is roughly approximated as a function of height by the value of the discretization steps of Tab. 3.1. This assumption is just a very rough approximation of the true vertical resolution of the temperature retrieval and it is still a matter of investigation (see Chap. 6, Fig. 6.7, where preliminary results for temperature retrieval errors using LES data provide further insight).

After determining the uncertainty on MLH due to measurement errors, Δz_{T_b}, and retrieval errors, Δz_{res}, the total uncertainty associated to the MLH estimates, Δz_{MLH}^{MWR} can simply be calculated by using standard error propagation laws *Barlow* [1989a]; *Rocadenbosch et al.* [2012] as $\left|\Delta z_{MLH}^{MWR}\right| = \sqrt{\left|\Delta z_{T_b}\right|^2 + \left|\Delta z_{res}\right|^2}$ (alternatively, and considering the rough degree of approximation involved, $\left|\Delta z_{MLH}^{MWR}\right| = \left|\Delta z_{T_b}\right| + \left|\Delta z_{res}\right|$).

3.3.2 Results and discussion

Following the methods described in Sect. 3.2.1 and Sect. 3.2.2, MLH estimates from lidar and MWR data along with errorbars are respectively discussed next for a day with typical ML development. Lidar backscatter data from a Jenoptik CHM-15k Nimbus ceilometer and potential temperature data retrieved from a RPG HATPRO MWR, on 18.04.2013 during the HOPE campaign at Jülich, Germany, are used.

It is a day with classic mixing layer development and weak or negligible synoptic conditions. In the morning, after sunrise at 04:30 UTC, the Earth surface starts to warm-up due to the absorption of solar heat, which is followed by convection-driven turbulence. The mixing layer starts developing at around 06:00 UTC and, after going through a morning transition between 06:00-11:00 UTC, reaches its maximum height in the afternoon at around 14:00 UTC. The process is reversed in the evening where the mixed layer starts its decay sometime around the sunset which is at about 18:45 UTC. The evening transition between 15:00 UTC and 19:00 UTC is marked by a quick fall of the convection-driven turbulence at the surface.

Fig. 3.4a and Fig. 3.4b, respectively, show the color-plot of the ceilometer backscattered signal and MWR-retrieved potential temperature for the 24-h cycle of the day. MLH esti-

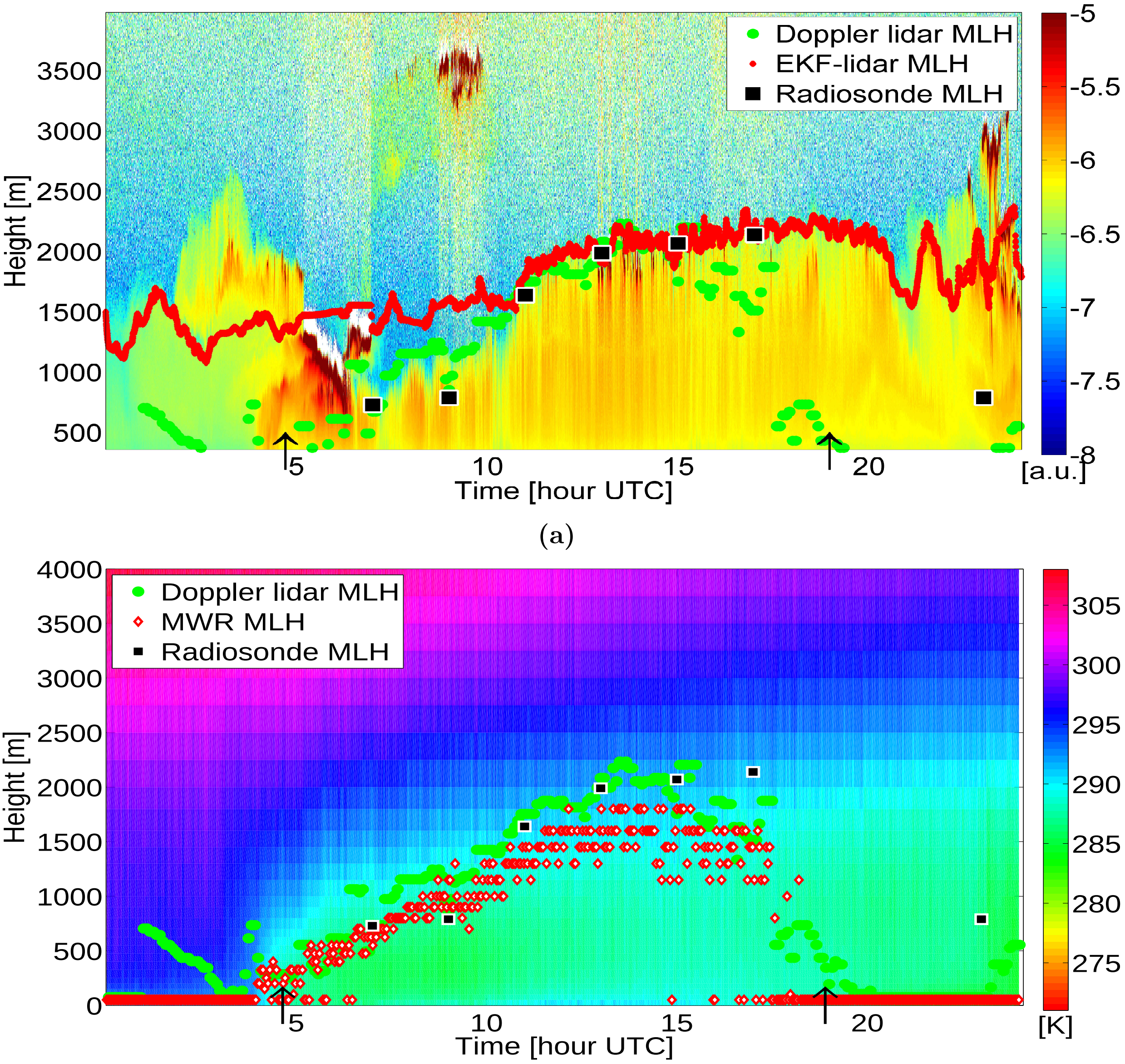

(a)

(b)

Figure 3.4: Measured ceilometer backscatter and potential temperature data along with MLH estimates (18.04.2013, Jülich, Germany). (a) Colorplot of the attenuated backscatter profile measured by the Jenoptik CHM 15K Nimbus ceilometer (colorbar in [a.u.]). (b) Colorplot of the MWR-retrieved potential temperature (colorbar in [K]). (Both panels) Vertical arrows mark sunrise and sunset times. Doppler-lidar measured MLH (green dots). Radiosonde derived MLH (black squares).

mates from the *lidar-EKF method* using ceilometer backscatter data (Sect. 3.2.1) and from the *MWR-parcel method* using potential temperature data (Sect. 3.2.2) are also shown. By comparing Fig. 3.4a and Fig. 3.4b it becomes clear that the lidar-EKF method (Fig. 3.4a) follows well the ML to FT transition. However, it is unable to follow the morning and evening ML transitions (06:00-11:00, 15:00-19:00 UTC) and, it tracks the RL, instead. A lofted aerosol layer, possibly due to synoptic advection, is also visible between the time interval 02:00-05:00 UTC at the height range 1500-2500 [m]. In contrast, the MWR-parcel method (Fig. 3.4b) not only provides MLH estimates for the mixed layer during the day-time but it also follows morning/evening ML transitions. The potential-temperature color-plot of Fig. 3.4b also correlates well with the idealized development of the mixed layer. However, and more importantly, the two MLH estimation methods also need to be compared in terms of the uncertainty on the MLH estimates and associated spatial and temporal resolutions.

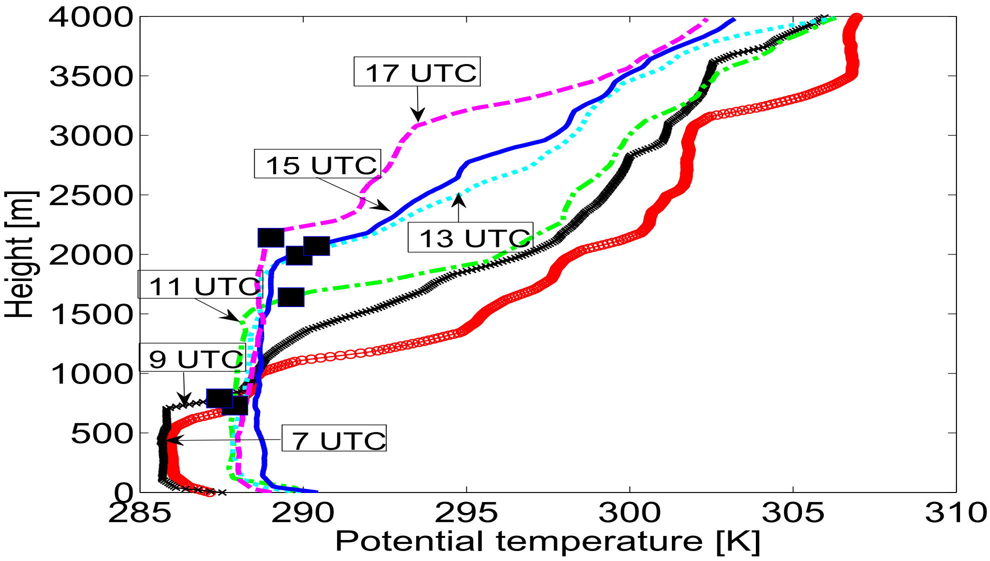

Figure 3.5: Profiles of the potential temperature and MLH estimates (parcel method) in response to radio-soundings at 07:00, 09:00, 11:00, 13:00, 15:00, and 17:00 UTC, 18.04.2013, Jülich, Germany.

Towards this end, the time intervals corresponding to morning/evening ML transitions and the fully-developed ML need to be determined. Radiosonde MLH and Doppler lidar MLH estimates are used for this purpose. Fig. 3.5 shows potential temperature profiles for six radiosonde launches at 07:00, 09:00, 11:00, 13:00, 15:00, and 17:00 UTC, along with indication of the MLH estimated by the parcel method. At 07:00 and 09:00 UTC the MLH lies between 700 and 800 [m] in height and then quickly rises to 1640 [m] by 11:00 UTC. The sudden rise in the MLH during the early morning is a characteristic of the morning ML transition, which in this case is between 06:00 and 11:00 UTC. From 11:00 to 17:00, the MLH varies between 1640 to 2140 [m], a moderate change over a 6-h time interval. However, when comparing with MLH-Doppler lidar (Fig. 3.4), it appears that turbulence started to cease by 15:00 UTC which makes the start of the evening ML transition.

In order to discuss the uncertainty associated to the EKF MLH estimates in Fig. 3.4, we focus on the time interval 06:00-19:00 UTC. To process this time interval, the lidar-EKF method was re-initialized at 06:00 UTC with default values for the state-vector and the error covariance matrices. This re-initialization was necessary for two reasons: The presence of an early morning cloud at the height of 1 [km], and to avoid the assimilation of past-time estimates and related error statistics corrupted by the cloud intrusion at around 05:00 UTC.

Thus, Fig. 3.6a shows MLH and related error-bar estimates from the lidar-EKF method (Sect. 3.3.1.1) along with MLH estimates from the six RS launches at the times mentioned above and MLH estimates from the Doppler lidar. It emerges that the EKF follows the MLH in excellent agreement with the Doppler lidar reference for the ML time interval between 11:00-15:00 UTC, where the ML is well developed but slightly apart in the transition times (06:00-11:00 UTC and 15:00-19:00 UTC), where the ML experiences fast changes in height. The computed RMSE is 105 [m] (excluding the transition times). During part of the early-morning transition time (06:00-09:00 UTC), the EKF is still somehow ambiguated by the presence of the cloud layer (around 1 [km] in height) and its reminiscence in the assimilated statistics. In the 15:00-19:00 UTC transition time the EKF is ambiguited by the RL, instead.

The uncertainty on the MLH estimates from the lidar-EKF method is shown as 3-σ error-bars. As mentioned, the EKF formulation provides the *a posteriori* error associated to the state-vector estimates and, therefore, the calculation of the uncertainty on MLH is inherent to the method. For this study case, the 3-σ uncertainty on the MLH is on average ±91 [m] in the time interval 11:00-15:00 UTC.

In Fig. 3.6b corresponding MLH estimates using the MWR-parcel method are shown. Following the approach of Sect. 3.3.1.2 MLH error-bars are also shown. Here, it is pertinent to notice that error-bars, in the time interval 11:00-15:00 UTC (fully developed mixed layer) are ±483 [m] on average, a much higher figure than EKF error-bars for the lidar case.

Following the discussion above, it becomes clear that both instruments have their own strengths and limitations. On one hand, the lidar-ceilometer provides highly resolved (±91 [m] 3σ average) estimates of the MLH but it lacks physical consistency, especially at morning/evening ML transitions times. On the other hand, the MWR is able to follow morning/evening ML transitions reasonably well but is limited by the high uncertainty (±483 [m] on average) associated to its MLH estimates.

Therefore, a synergetic method which exploits the strengths of the two instruments is expected to provide highly resolved estimates of the MLH with low error-bars. In this context, MWR estimates can be used to narrow and disambiguate the search interval of the lidar-based MLH-estimation method to be used (e.g., any morphological method like the threshold method *Melfi et al.* [1985] or more sophisticated ones like the EKF in this paper, still a matter of research). Such an approach would provide physically consistent estimates of MLH while also disambiguating multiple layers scenarios, in which sometimes it is difficult to come up with a correct estimate of the MLH.

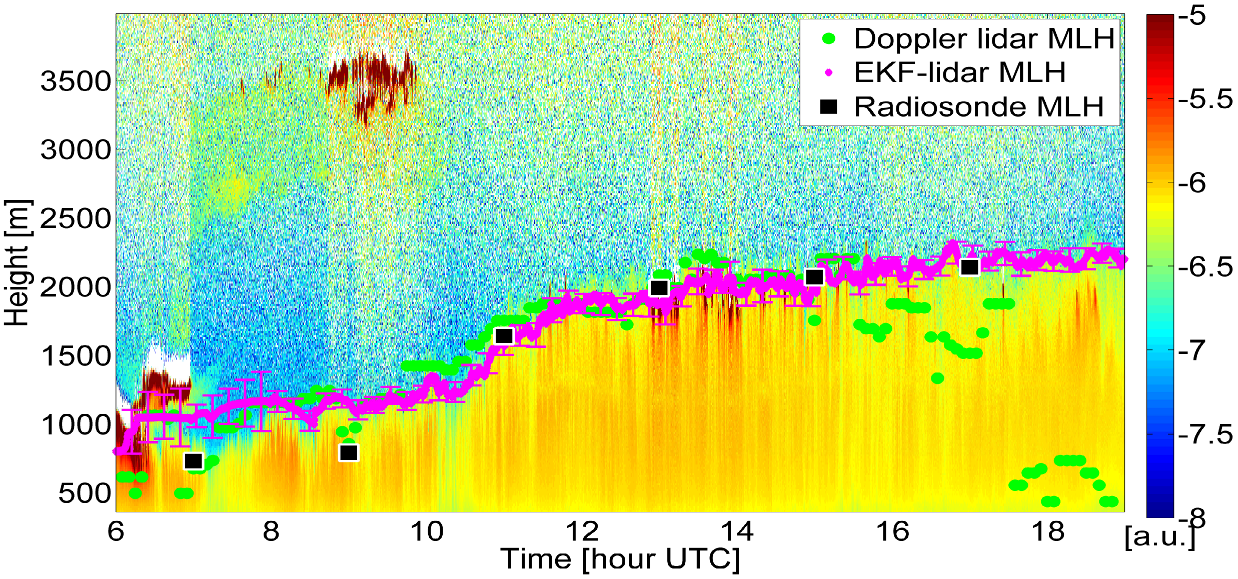

(a)

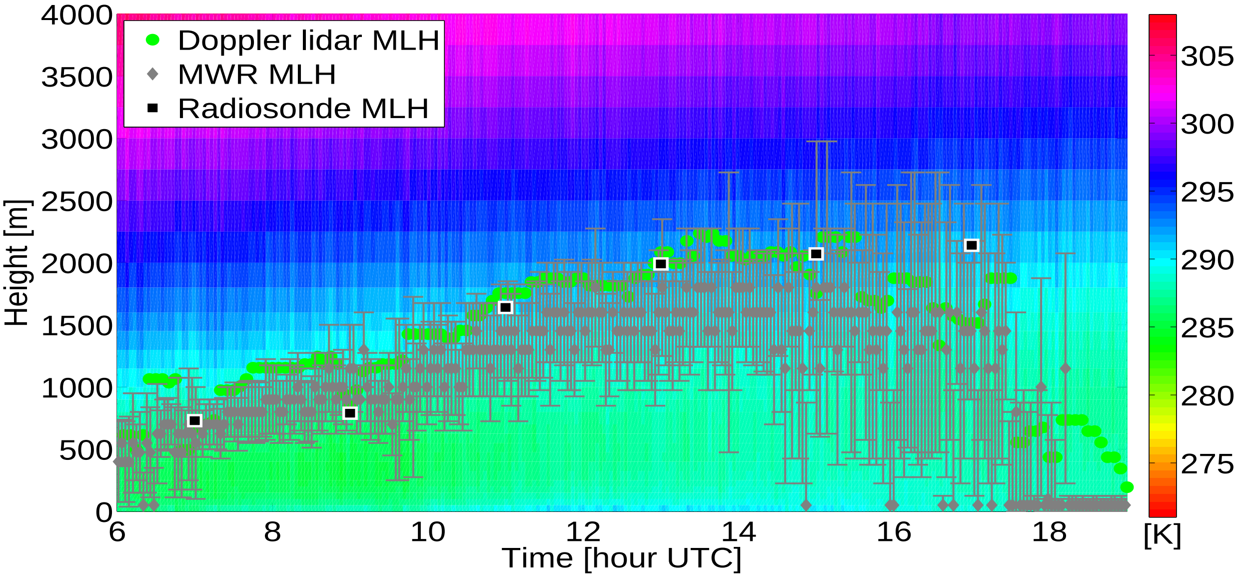

(b)

Figure 3.6: Detail of Fig. 3.4 during day-time (06:00-19:00 UTC) along with estimated error-bars. (a) Lidar-EKF MLH estimates and related errorbars (magenta trace). Doppler-lidar measured MLH (green dots). Radiosonde derived MLH (black squares). (b) MWR-parcel-method MLH estimates and related errorbars (grey trace). Radiosonde derived MLH (black squares). Colorbars same as in Fig. 3.4.

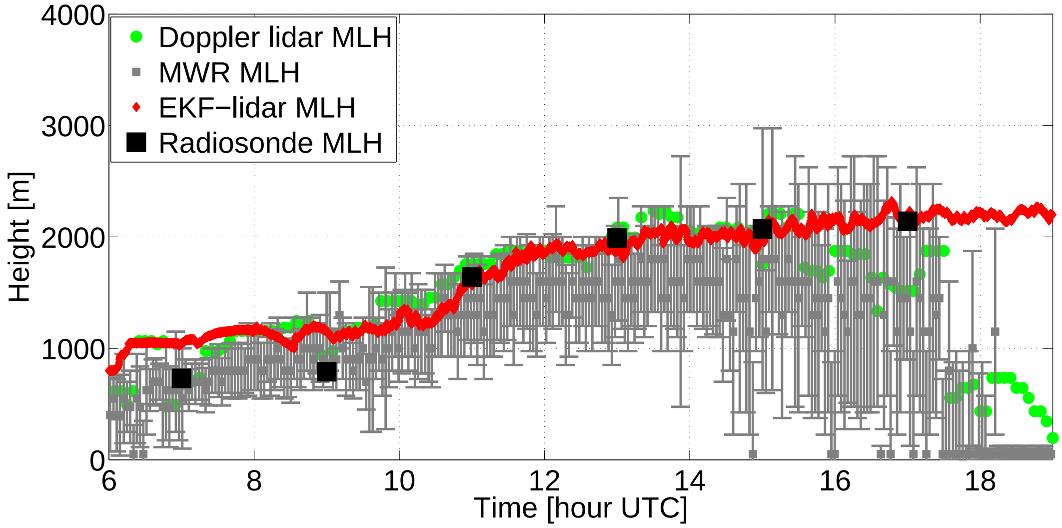

Figure 3.7: MLH error-bars obtained from lidar-EKF and MWR-parcel methods are superimposed on each other. Proposed scheme for lidar-MWR synergy is based on the fact that coarse MWR-parcel error-bars define the search interval for lidar-based MLH estimators.

Fig. 3.7 tentatively shows the proposed scheme where MLH estimates from the two methods along with related error-bars are super-imposed on each other. As it can be observed, MLH estimates from the lidar-EKF and MWR-parcel methods agree well with each other and with MLH-radiosonde and MLH-Doppler lidar estimates (truth references in this study) when the ML is fully developed (11:00-15:00 UTC). However, during morning and evening ML transition times (06:00-09:00 UTC and 15:00-19:00 UTC) the lidar-EKF method follows the RL, instead. In the ML transition times, only the MWR-parcel method yields correct MLH estimates.

3.4 First test of the synergetic use of lidar and MWR observations for MLH detection

3.4.1 Synergetic MLH estimation method

In order to come up with a synergetic method for the estimation of the MLH it is important to identify the morphological features associated to the development of ML over the course of a day. Fig. 3.8a shows a color-plot of the standard deviation of the vertical wind velocity, σ_w, measured by the Doppler lidar for a 24-hr period on 24.04.2013. MLH estimates (green circles) are also plotted on top of the color-plot. Sunrise time (vertical arrow at around 04:30 UTC) and sunset time (vertical arrow at around 18:45 UTC) as well as start time of the development of the ML and the end of the fall (vertical red lines) are indicated. The development of the ML starts at 8:00 UTC and reaches its peak at around 16:00

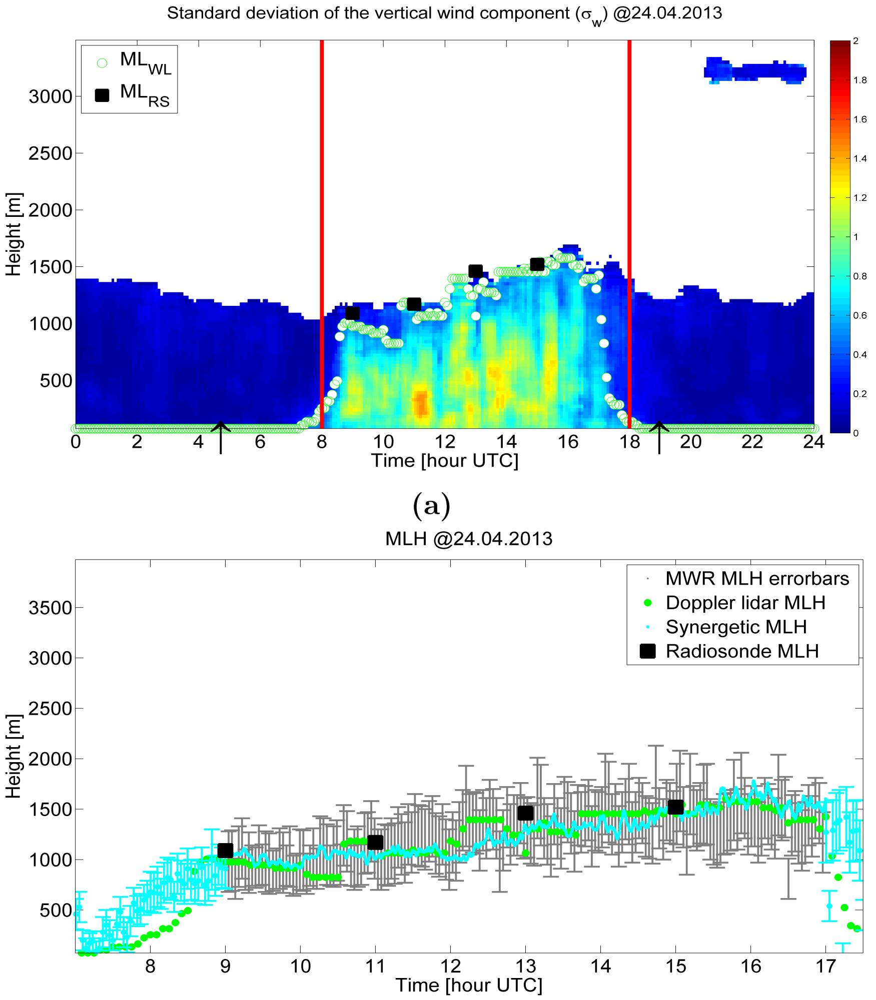

(a)

(b)

Figure 3.8: Synergetic MLH estimation using ceilometer and MWR instruments. (a) Color-plot of the standard deviation, σ_w, of the vertical wind velocity measured by the Doppler lidar along with MLH estimates (green circles) for 24-hours of measurements on 24.04.2013. MLH estimates from radiosondes (black squares) are also shown. Sunrise (04:30 UTC) and sunset (18:45 UTC) times as well as the test data range (07:00-18:00 UTC) are marked by the vertical arrows and the red vertical lines, respectively. (b) Synergetic MLH estimates in the daytime, 09:00-17:00 UTC, (cyan trace) obtained by the Lidar-MWR synergy, and transition regions (cyan error-bars) using parcel method on MWR potential temperature only. Reference MLH estimates from Doppler wind lidar (green circles) and radiosondes (black squares).

UTC. There is a sudden drop of the ML with almost no mixing at about 18:00 UTC. The transition regions in the morning (8:00-9:00 UTC) and evening (16:00-18:00 UTC) are also clearly identified.

Therefore, two distinct regions of ML are identified, the daytime ML from 9:00-16:00 UTC and the transition regions in the morning 8:00-9:00 UTC and evening 16-18 UTC. In the transition region, the ML changes significantly from one value to other in a short period of time. The aerosols are limited in following the quick changes in the atmosphere mainly due to the fact that when a ML layer starts developing in the morning it is topped by a SBL from the previous night as well as a RL from the previous day *Wang et al.* [2012]; *Schween et al.* [2014]. Similarly, in the evening transition ML when the mixing ceases and a SBL starts developing the RL from the daytime is present on top of it. However, MWR captures the changes in the thermodynamic structure of the atmosphere well and thus is able to follow the transition of the ML in the morning and evening *Wang et al.* [2012].

Therefore, two different strategies are adopted for the estimation of the MLH for these two regions.

3.4.1.1 MLH in transition-time regions

MLH estimates for the morning/evening transitions are available only from MWR data due to the lack of aerosol signatures. Parcel-method estimates of the MLH are used for this purpose. At low heights, during the rise of the ML transition in the morning and the ML fall in the evening, the resolution of the MWR-retrieved temperature profile is good enough to provide reasonably good estimates. However, towards the culmination of morning transition and start of the evening transition, high uncertainty (about the same order as for fully mixed-layer) is associated to the transition-MLH due to the coarse resolution of the MWR which decreases with height.

3.4.1.2 Daytime MLH

As discussed in Sect. 3.1, for the daytime ML aerosols provide a clear signature in the backscatter signal for most of the cases. However, aerosols are not always good indicators of the underlying turbulence in the boundary layer since their response to the changes in the extent of the boundary layer is delayed. MWR temperature measurements are directly linked to the thermodynamic state of the atmosphere and they are a physically consistent indicator of the ML. However, as mentioned, MWR retrievals suffer from coarse spatial resolution than lidar ones. The foundations of the synergetic method presented next exploit the strengths of the two instruments.

We propose to assimilate the coarse MWR estimates into the Lidar-EKF ML formulation from ceilometer backscatter data described in Sect. 3.2.1. At each time instant, t_k, the fitting ranges for the EKF, $z_{1,k}$, $z_{1,k}^{'}$, $z_{2,k}^{'}$ and $z_{2,k}$ are re-defined as

$$\begin{aligned} z_{1,k} &= \hat{z}^{l}_{\theta,k} \\ z_{1,k}^{'} &= \hat{z}_{ML,k-1} - \frac{z_{EZ,k-1}}{2} \\ z_{2,k}^{'} &= \hat{z}_{ML,k-1} + \frac{z_{EZ,k-1}}{2} \\ z_{2,k} &= \hat{z}^{u}_{\theta,k}, \end{aligned} \tag{3.7}$$

where $\hat{z}^{l}_{\theta,k}$ and $\hat{z}^{u}_{\theta,k}$ are the lower and upper bounds from the MWR at discrete time t_k, and $\hat{z}_{ML,k-1}$ and $\frac{z_{EZ,k-1}}{2}$ are the MLH and EZ width estimated by the EKF from ceilometer data at time t_{k-1}.

The formulation described in Eq. 3.7 presents a methodology whereby thermodynamic information about the atmosphere, from the MWR, is assimilated into the EKF (attenuated backscatter signals from the ceilometer).

3.4.2 Results and discussion

Fig. 3.8b shows MLH estimates from the EKF method (ceilometer backscatter data) and parcel method (MWR-retrieved potential temperature profile). During the daytime ML, MWR coarse estimates (grey errorbars) guide the EKF. Moreover, MLH estimates from the Doppler lidar and the radiosonde are also plotted for comparison purposes.

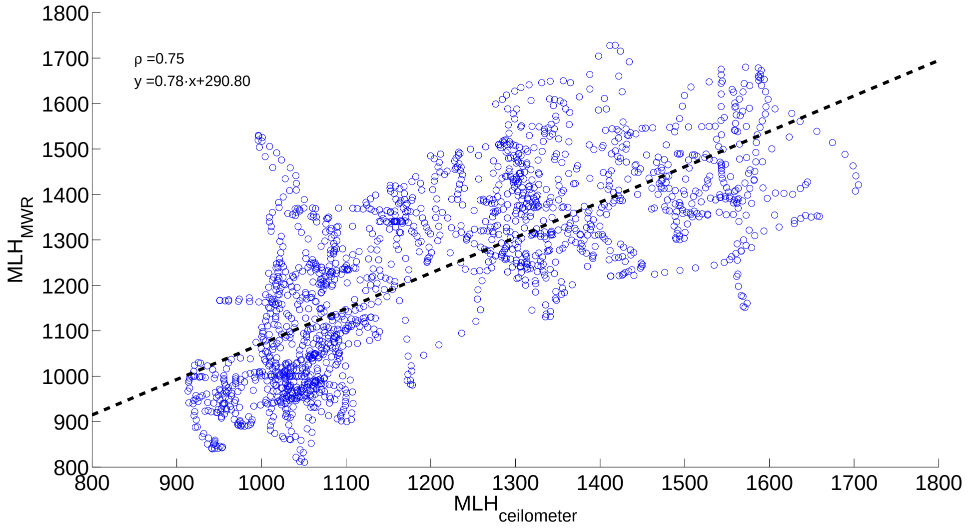

Figure 3.9: Scatter-plot relating the MLH, estimated by the EKF (ceilometer backscatter data), horizontal axis, and the parcel method (MWR-retrieved potential temperature), vertical axis. Regression line (black dashed trace). Correlation and regression coefficients are also indicated. Data used: 09:00-16:00 UTC, 24.04.2013, Jülich, Germany.

Fig. 3.9 shows the scatter-plot relating the daytime convective MLH (09:00-16:00 UTC) estimated from the EKF (ceilometer) and the parcel method (MWR). In order to achieve a one-to-one correspondence between the estimates from the two instruments, MLH estimates from the MWR have been interpolated to match the time-stamps of ceilometer data. The fitting is far from the ideal straight line (dashed black) and still there is considerable mismatch between the MLH estimates from the two instruments. Quantitatively, with a slope of 0.78 and an offset of 290.80 m and a correlation coefficient of 0.75, the two instruments disagree with each other to some extent. One of the key reasons associated to this disagreement lies on the physical nature of the parameters measured by each instrument. Thus, while a ceilometer measures the aerosol backscatter, which does not instantaneously follow the thermodynamic state of the ABL (delay with which the aerosols respond to the turbulent forcings), the MWR measured T_b. The bias in the retrieved MLH (≈ 290) can, in part, be explained by the fact that the potential temperature retrieved from the MWR is always associated to a coarse estimate of the MLH and, therefore, representing it with a single value in the scatter-plot (the center value of this coarse estimate) introduces a bias.

During the transition times in the morning and evening the MWR follows well the rise and fall of the MLH. EKF estimates from the ceilometer backscatter data provide the RL height in the transition regions.

3.5 Conclusions

Two commonly used indicators for MLH retrieval, namely, the attenuated backscatter coefficient from ceilometer measurements and atmospheric potential temperature from MWR measurements have been compared. The EKF has been used to estimate the MLH from the lidar backscatter data and the parcel method from the MWR-retrieved potential temperature profile.

Measurement and retrieval errors from both lidar and MWR instruments have also been assessed in order to estimate the MLH uncertainty. The impact of the measurement noise associated to the ceilometer backscatter signal has been assimilated into the noise-covariance matrix of the EKF, which yields the MLH estimation error (σ^P_{MLH}) via the *a posteriori* error covariance matrix. In the case of the MWR, first, brightness-temperature measurement errors have been linked to the MLH uncertainty by using classic perturbation and error-propagation theory. Second, vertical-resolution errors (a consequence of the low DoF during the brightness-temperature-to-absolute-temperature retrieval) have been assimilated by using the discretization grid of the temperature profile as the proxy for the height-decreasing vertical resolution of the profile.

The methods have been validated on a measurement day with typical mixing-layer development. Ceilometer backscatter data was gathered by a Jenoptik CHM 15k Nimbus ceilometer. Potential temperature data was retrieved from brightness measurements performed by a RPG HATPRO MWR during HOPE campaign at Jülich, Germany.

When comparing both methods, on one hand, the lidar-EKF method provides highly-resolved estimates of the MLH but lacks physical thermodynamic consistency in the RL or in instances with multiple layers (e.g., cloud-topped ML). On the other hand, the parcel-MWR method provides physically consistent estimates of MLH albeit with coarse vertical resolution.

In this context, a simple synergetic MLH retrieval scheme for the estimation of the daytime mixed-layer as well as morning/evening transition times has been proposed. Data from the two instruments, a ground-based ceilometer and a MWR, has been combined in a physically consistent approach. For the morning/evening transitions ML estimates from the MWR data alone are used. For the daytime ML, coarse estimates of the ML from the MWR guide the EKF based algorithm for the aerosol backscatter data from the ceilometer. The method thus exploits highly-resolved aerosol measurements by the ceilometer as well as thermodynamic information of the atmosphere from the MWR-retrieved temperature data. For comparison/validation purposes, ML estimates from a Doppler lidar as well as from radiosonde (whenever available) are used. The method has been applied on real measurements from 24.04.2013, 07:00-18:00 UTC collected during the HOPE campaign. Comparison with the Doppler lidar and radiosondes has revealed a good degree of agreement. The RMSE of the synergetic method with respect to Doppler-lidar MLH estimates is 197.46 [m] (computed over 07:00-18:00 UTC, Fig. 3.8b, which encompasses daytime ML as well as morning/evening transition boundary-layer). This represents an error reduction of about 178 [m] when compared with the error associated to the Lidar-EKF method (RMSE = 375.66 [m]) and an error reduction of about 45 [m] over MWR-parcel method (RMSE = 242.32 [m]).

Chapter 4

Stable boundary-layer height estimation

This chapter summarizes basic concepts and principles for nocturnal Stable Boundary-Layer Height (SBLH) estimation using attenuated lidar backscatter and MicroWave-Radiometer (MWR) temperature measurements. It is shown that temporal and spatial variance of the attenuated lidar backscatter signal are related with the stratification of aerosols in stable boundary-layer. Two different minimum variance estimators (local minima detection and an Extended Kalman Filter) are introduced for SBLH estimation. MWR-retrieved potential-temperature profile is also discussed along with idealised SBL models from literature.

The contents of this Chapter are part of the papers *Saeed and Rocadenbosch* [2016b] to be submitted to IEEE Transac. Geosc. Rem. Sensing, *Saeed et al.* [2015a] published in IGARSS, 2015, and *Saeed and Rocadenbosch* [2015] published in Proc. of SPIE, 2015.

4.1 Introduction

The structure of the Nocturnal Boundary Layer (NBL) mainly depends upon three underlaying physical processes namely, turbulent mixing, radiative cooling and heat exchange with the soil *Steeneveld et al.* [2004]; *Qiang and Sheng* [2009]. The type of the NBL which develops at a particular location and time depends upon the relative strength of these processes and, therefore, there can be three types of the NBL: fully turbulent (also known as the night-time ML), intermittently turbulent, and non-turbulent (also known as the SBL). Fully turbulent NBL occurs when wind shear becomes the dominant force, whereas in the case of the non-turbulent NBL or SBL *Hyun et al.* [2005]; *Angevine et al.* [2006], radiation and heat exchange with the soil become dominant and turbulence is almost non-existent resulting in horizontal stratification of the aerosols in the atmosphere through a process known as *fanning Stull* [1988]. The intermittently turbulent NBL occurs when there are alternating cycles of turbulence and non-turbulence.

From the modelling perspective, it is a big challenge to capture these three types of NBL. Whereas models do capture the turbulence and related mixing processes quite well, the modelling of stable boundary conditions is still poor *Seidel et al.* [2012]. Nevertheless, the accurate modelling of the SBL is highly important for correctly predicting night-time temperatures and the dispersion of pollutants and, therefore, it is of much interest and relevance in the ABL research community to study the SBL and its correct estimation *Cuxart et al.* [2006].

4.1.1 Foundations of SBLH estimation from lidar data

During the night time, especially when there is minimum to nil convection and the turbulence due to mechanical wind shear is negligible, a SBL develops near the ground surface. As a result, in the absence of any external forces, aerosols in the atmosphere gets stratified in a layered fashion. This layering of aerosols can result in a single or multiple layers depending on the location and type of the atmospheric aerosols.

Fig. 4.1a shows an idealized sketch of the atmospheric aerosols as seen by a profiling backscatter lidar. The layered structure of aerosol stratification during the night-time is in clear contrast to the day-time mixed layer, where aerosols are more or less homogeneously mixed due to convection-driven turbulence. Multiple layers of aerosol span over the horizontal dimension and with varying widths in the vertical dimension. These layers align at different heights depending upon the type and characteristics of the local aerosol species. The nocturnal SBL is topped by a residual mixed layer from the preceding day-time. The EZ and the CI act as buffers for the day-time mixed layer and night-time SBL, respectively.

Fig. 4.1b colorplot is a 24-h *attenuated backscatter* measurements (in what follows "the backscatter") showing the distribution of atmospheric aerosols on 24th April 2013. A sketch of the idealized ABL structure is superimposed on the colorplot. Comparing day- and night-time regions of the colorplot it is evident that the atmosphere is under stable conditions during night-time and in a well-mixed state during the day-time. However, the stratification of aerosols is not clearly visible and, therefore, it needs further investigation.

If a backscattered lidar signal is plotted versus time, each layer of aerosol is seen as a strong, and more or less constant, backscatter signature within the aerosol layer boundaries (Fig. 4.2). As a result, regions with a relatively constant backscatter level in the height-dependent backscatter profile correspond to MVRs in the backscatter variance profile. MVRs mark a sharp decrease of the variance below and above an aerosol layer.

For estimation purposes, a MVR is modelled by an inverted Gaussian-like function as shown in Fig. 4.2. The bulk of the inverted Gaussian bell lies in the height interval $\left[z_1', z_2'\right]$ whereas its ending tails lie in the range intervals $\left[z_1, z_1'\right]$, and $\left[z_2', z_2\right]$, characterized by an approximately constant high variance level. The inverted Gaussian-like profile shown corresponds to an idealized aerosol layer which is represented as a uniform backscatter

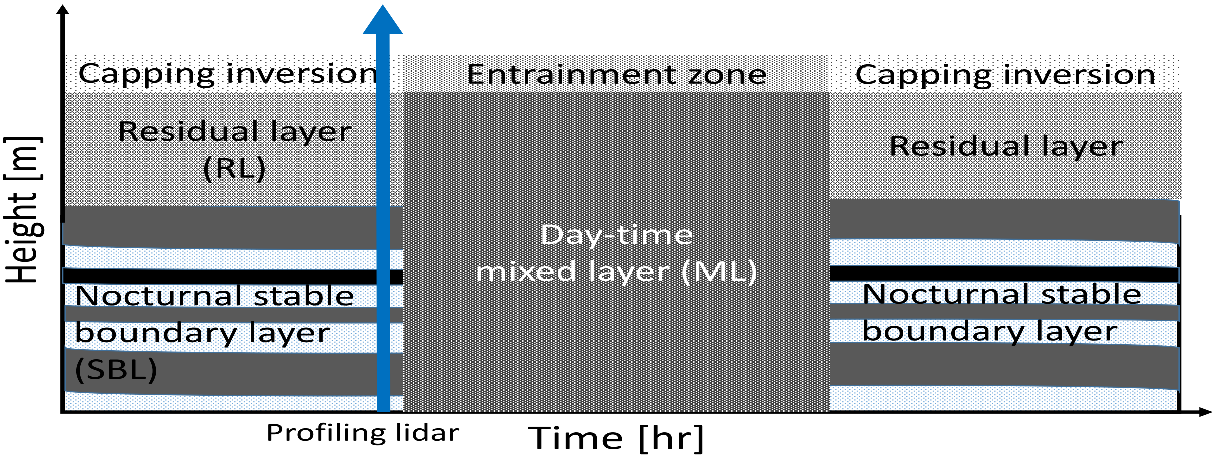

(a)

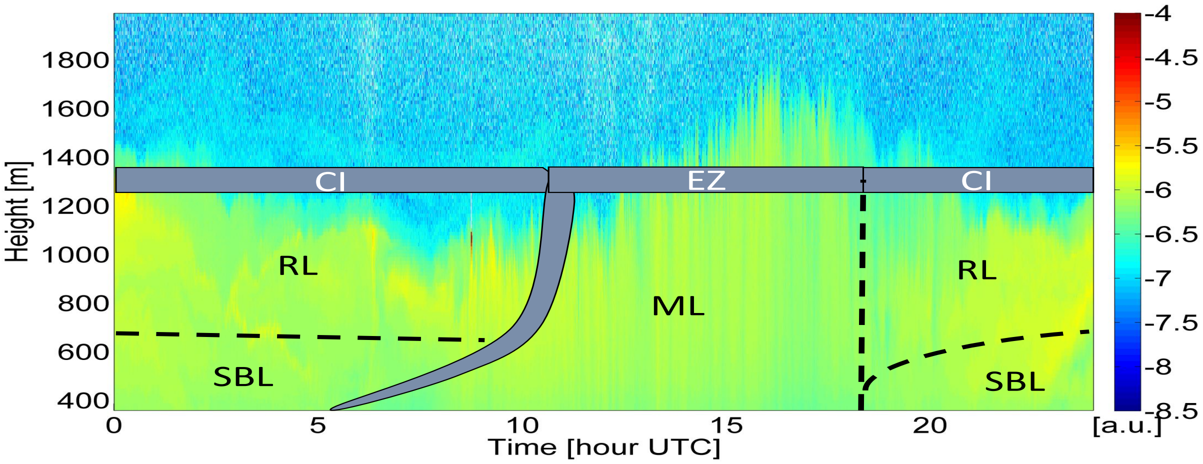

(b)

Figure 4.1: The ABL structure. (a) Idealized sketch of the daily evolution of the ABL in terms of the distribution of atmospheric aerosols (as seen by a profiling backscatter lidar). During the day time aerosols are well-mixed due to convection-driven turbulence. However, during the night aerosols stratify by forming layers. (b) Color-plot of the attenuated backscatter signal from a Jenoptik CHM 15k ceilometer for 24-hr of data on 24.04.2013. Idealized sketch of the evolution of ABL, marking different regimes of boundary-layer, namely, the day-time ML topped by the EZ, and the nocturnal SBL topped by the RL and the Capping Inversion (CI) (superimposed). The well-mixed atmosphere during the day-time is well reflected by the backscatter signal. However, the stratification of aerosols during the night-time is not clearly visible. This is typically the case, since the stratification of aerosols never happens in an idealized way as shown in Fig. 4.1a.

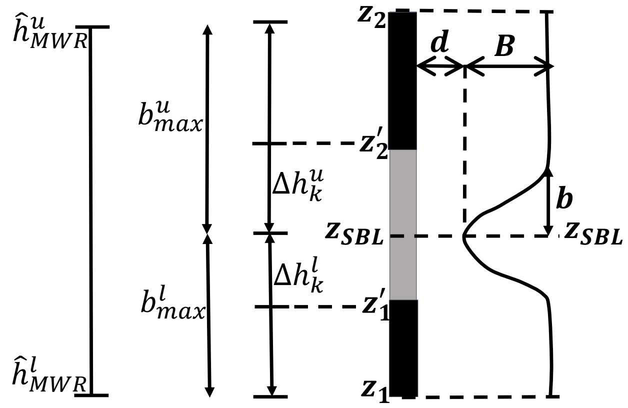

Figure 4.2: Backscatter model variance profile. Conceptual sketch of a MVR modeled by an inverted Gaussian function along with fitting boundaries, z_1, $z_1^{'}$, $z_2^{'}$, and z_2. The inverted Gaussian bell on the right shows a MVR within the height interval, $\left[z_1^{'}, z_2^{'}\right]$. The center of the MVR corresponds to the SBLH given by z_{SBL} and its width is represented by parameter b. Parameter "d" stands for the background variance and parameter "B" indicates the variance amplitude above the background. Interval $\left[z_1, z_1^{'}\right] U \left[z_2, z_2^{'}\right]$ corresponds to the tail of the Gaussian outside the MVR. On the right, the fitting boundaries are labelled in terms of the parameters $h_{MWR}^{u,l}$, $\Delta h_k^{u,l}$, and $b_{max}^{u,l}$ (see Sect. 5.2.3).

signal across its vertical extent. The center of the idealized bell represents the height of the SBL and its spread or standard deviation roughly corresponds to the width of the aerosol layer. The constant variance levels of the Gaussian model correspond to the background variance outside of the aerosol layer. Mathematically, the backscatter variance model is formulated as

$$h(\mathbf{x}) = Be^{-\frac{1}{2}\left[b(\mathbf{z}-z_{SBL})\right]^2} + d, \tag{4.1}$$

where $\mathbf{x} = [z_{SBL}, b, B, d]^T$ is the state vector, $\mathbf{z}$ is the height vector, z_{SBL} is the SBLH, $b = \frac{1}{\sigma}$ (being the standard deviation of the Gaussian distribution) is the width parameter, B is the variance amplitude, and d is the background variance level. As customary, bold font is used to represent vectors. These four parameters can be estimated either adaptively by using an EKF or non-adaptively by using a Non-linear Least SQuares (NLSQ).

4.1.2 Foundations of SBLH estimation from MWR data

The development of the SBL is directly linked to the thermodynamic state of the atmosphere. As the convection-driven turbulence starts to cease towards the early evening, a SBL starts to develop from the surface *Stull* [1988]. This SBL keeps on developing during the night until reaching its peaks towards late night/early-morning.

The SBL is marked by an increasing potential temperature up to an inversion *Bradley et al.* [1993]; *Liu and Liang* [2010]; *Angevine et al.* [2006], where typically it smoothly merges into the RL. It is important to mention here that the SBLH is well above the temperature inversion since it extends up to the height where the temperature lapse-rate becomes adiabatic *Stull* [1988]; *Bradley et al.* [1993]; *Collaud Coen et al.* [2014].

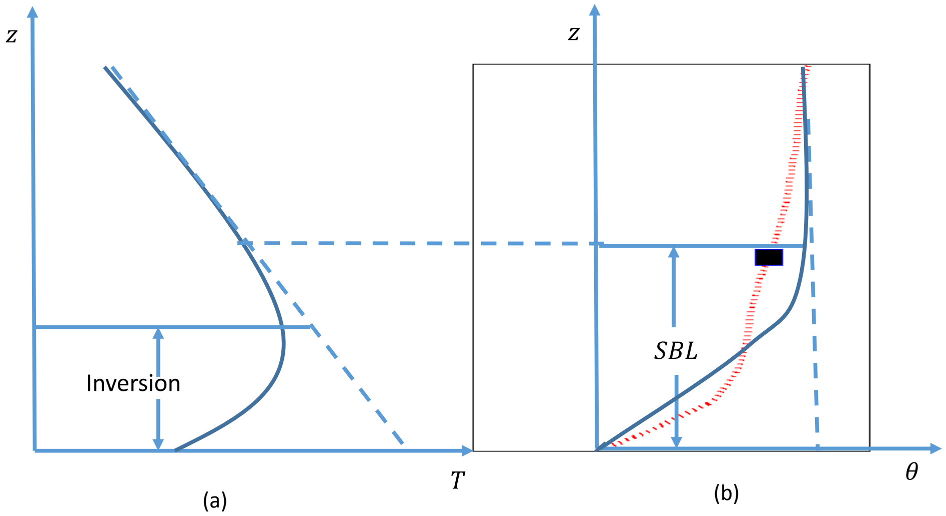

Figure 4.3: Idealized structures of the physical temperature and potential temperature profiles (adapted from Stull, 1988 *Stull* [1988]). (a) Physical temperature increases until an inversion occurs where it starts decreasing ultimately achieving the adiabatic lapse-rate. (b) Potential temperature increases in the SBL and smoothly merges into the RL, where it stays constant. Potential temperature profile based on measurements from a radiosonde (dotted trace) launched on 24.04.2013, 23:00 UTC at Jülich during HOPE campaign is plotted on top of the idealized potential temperature profile. SBLH estimate (black square) from the radiosonde-measured potential temperature is also shown.

Fig. 4.3a and Fig. 4.3b show the idealized physical temperature and potential temperature profiles under stable atmospheric conditions *Stull* [1988]. The temperature of the atmosphere in stable conditions first increases until an inversion occurs where it starts decreasing until the inversion smoothly merges into the RL where the dry adiabatic lapse-rate of about 10 C/km is achieved. This behavior is reflected in terms of the potential temperature as increasing trend until the point where inversion occurs. A gradual decrease after that merges the inversion smoothly into the RL where the change in the potential temperature is almost negligible ($\frac{\partial \bar{\theta}}{\partial z} \approx 0$). For comparison with real data, potential temperature profile measured by a radiosonde as well as the SBLH estimate are also shown in Fig. 4.3b.

With a view to estimate SBLH in Sect. 4.3 five idealized potential-temperature model profiles *Stull* [1988] are fitted measured ones from MWR. Model profiles are based on two key parameters $\bar{\theta}_0$ and $\bar{\theta}_s$, which are the RL and near-surface potential temperature, respectively. The idealized profiles incorporate the SBLH, noted here as h, and θ_0 as the main parameters along with auxiliary parameters.

1. Stable mixed

$$\theta(z) = \begin{cases} \theta_s, & \text{for } z \leq h \\ \theta_0, & \text{for } z > h \end{cases} \tag{4.2}$$

2. Mixed linear

$$\theta(z) = \begin{cases} \left(1 - \frac{z}{h}\right)\theta_s + \frac{z}{h}\theta_{\Delta h}, & \text{for } z \leq h \\ \theta_0, & \text{for } z > h \end{cases} \tag{4.3}$$

   where $\theta_{\Delta h}$ is the temperature step at the top of the SBL.

3. Linear

$$\theta(z) = \begin{cases} \theta_s + (\theta_0 - \theta_s)\frac{z}{h}, & \text{for } z \leq h \\ \theta_0, & \text{for } z > h \end{cases} \tag{4.4}$$

4. Polynomial

$$\theta(z) = \begin{cases} \theta_0 - \left(1 - \frac{z}{h}\right)^{\alpha}(\theta_0 - \theta_s), & \text{for } z \leq h \\ \theta_0, & \text{for } z > h \end{cases} \tag{4.5}$$

   where α is the model order (typical value 2-3).

5. Exponential

$$\theta(z) = \theta_0 - (\theta_0 - \theta_s)\, e^{-\frac{z}{H_{\Delta\theta}}} \tag{4.6}$$

   where $H_{\Delta\theta} = \frac{\int_0^h [\theta_0 - \theta(z)] d\theta}{\theta_0 - \theta_s}$ is the *accumulated cooling* within the SBL.

4.2 SBLH estimation using variance processing and backscatter lidar data

In Sect. 4.1, the relation between the stratification of aerosols and MVRs in the backscatter lidar vertical profile has been introduced. A given lidar attenuated backscatter dataset takes the form of a measurement matrix, where each row represents the backscatter at a given height as a function of time, and each column represents a time observation of the backscatter as a function of height (i.e., a time observation of the vertical backscatter profile). For a given backscatter measurement matrix, the variance matrix can be calculated in two ways: 1) As a temporal variance, where each discrete height is processed using MA time window; 2) As a spatial variance, where each time instant is processed using a MA window in the height domain. The window is chosen such that it provides a reasonable tradeoff between the resulting resolution and the noise rejection. In the following, backscatter data from Jenoptik CHM15k Nimbus ceilometer is used. The high SNR of this ceilometer is well suited for detecting backscatter signal variantions in terms of its variance. However, the drawback of Jenoptik CHM15k Nimbus ceilometer is its high overlap range (≈350 [m]), limiting the application to aerosols stratification above this height.

4.2.1 Height and time clustering

Prior to computing the MA variance, be it in temporal or spatial fashion, the lidar backscatter dataset is clustered according to the prevailing characteristics of ABL. This clustering is done in height and time domains for temporal and spatial variances, respectively.

Concerning temporal variance, the dataset is clustered into three height intervals, 360-644 [m], 1259-1543 [m], and 1558-1993 [m]. The first height interval, 360-644 [m], covers the usual heights associated to the SBL during the night-time and the lower part of the ML during day-time. The second interval, 1259-1543 [m], covers the top of the ML during the day-time and RL during night-time. Finally, the third interval, 1558-1993 [m], lies in the FT. Fig. 4.4a shows height clustering of backscatter data on 24.04.2013. It is evident that the first interval involves most morphological structures during night-time correlating with the stratification of aerosols in the SBL. The second interval shows sharp changes in the backscatter data during day-time, thus confirming the existence of updrafts and downdrafts in the EZ. The third interval shows no changes in the backscatter meaning there are almost nil aerosol changes in the FT. The three representative profiles corresponding to the center of each height interval, i.e., at 509 [m], 1409 [m], and 1783 [m] are highlighted in thick black trace.

Similarly, spatial processing requires clustering the dataset into five time intervals, 00:00-05:00 [UTC] corresponding to early morning SBL, 05:00-10:00 [UTC] to morning-to-day transition boundary-layer, 10:00-16:00 [UTC] to day-time mixed-layer, 16:00-21:00 [UTC] to day-to-evening transition boundary-layer, and finally 21:00-24:00 [UTC] to night-time SBL. Fig. 4.4b shows these five clusters and the corresponding five time intervals. The homogeneity of lidar backscatter in the well-mixed atmosphere during day-time is evident when compared to the layered structures in night-time. The five representative profiles at the center of each time interval, i.e, at 2.5 [UTC], 7.5 [UTC], 13 [UTC], 18.5 [UTC], and 22.5 [UTC] are highlighted in thick black trace.

As a second step, the length of the MA window is computed. Towards this end, the Power Spectral Density (PSD) of the representative profiles in each temporal and spatial cluster above is calculated. The PSD reveals the distribution of the signal and noise power over the frequency spectrum. The PSD enables to identify the cut-off frequency where signal becomes buried into noise and which provides the MA window length.

Fig. 4.5a shows the block-diagram depicting the main steps involved for temporal variance processing. After height clustering and PSDs, the temporal MA window is estimated and used for temporal variance processing. Once the temporal variance matrix is computed, MVRs can be identified and, finally, the SBLH estimated. The processing steps for spatial

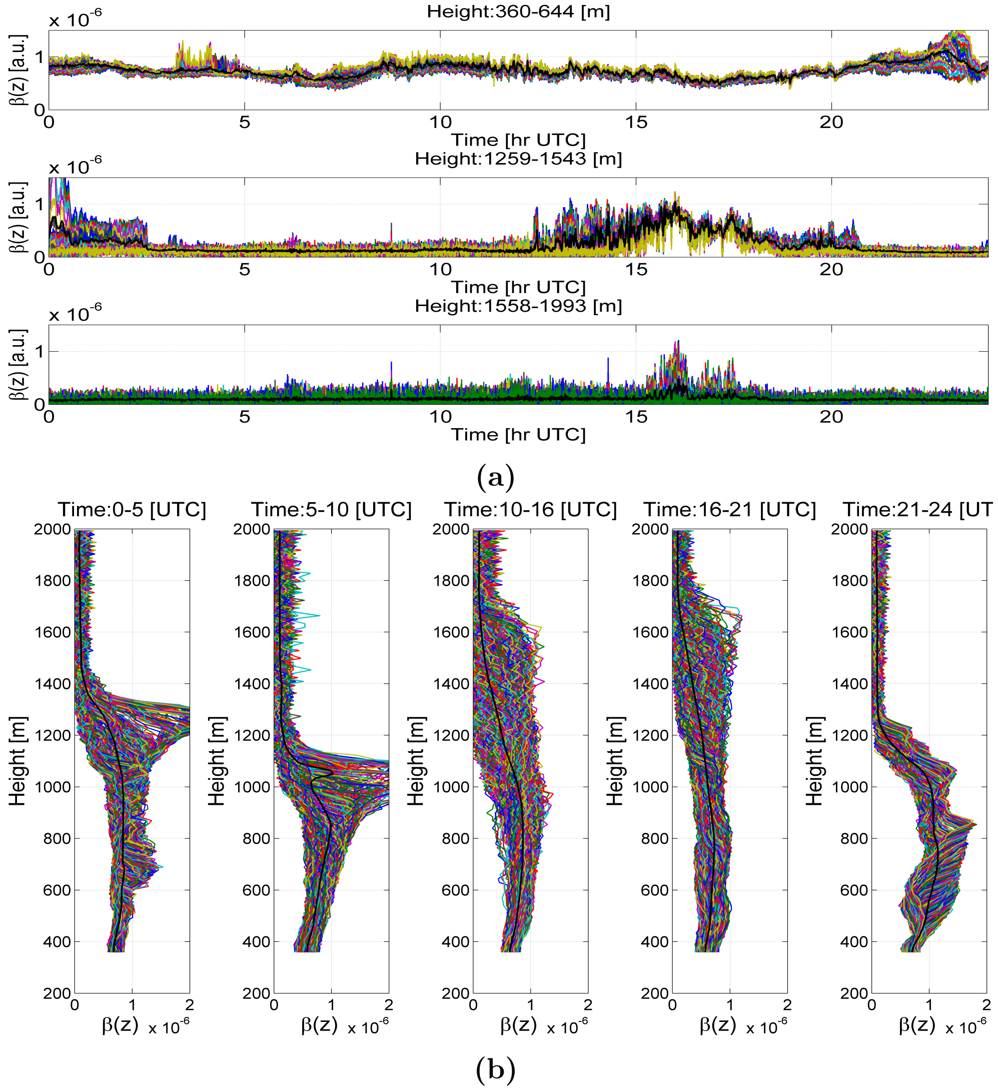

Figure 4.4: Clustering of backscatter data in height and time domain for further processing. (a) *Height clustering used in temporal processing:* The raw backscatter data is clustered in the height domain based on the prevailing atmospheric conditions at those height ranges. Three clusters have been defined: 360-644 [m] for stable conditions; 1259-1543 [m], which cover the top of the ML (including the EZ) during the *day-time* as well as the top of the RL (including the CI) during the *night-time*; 1558-1993 [m] spanning exclusively over free troposphere heights. The backscatter time series at the middle height of each interval is highlighted in thick black trace and will be used as the representative series of each cluster for temporal processing. (b) *Time clustering used in spatial processing:* Five clusters for spatial processing have been identified as follows: 0-5 [hr UTC] for early-morning SBL, 5-10 [hr UTC] for morning SBL-ML transition, 10-16 [hr UTC] for day-time ML, 16-21 [hr UTC] for evening ML-SBL transition, and 21-24 [hr UTC] for night-time SBL.

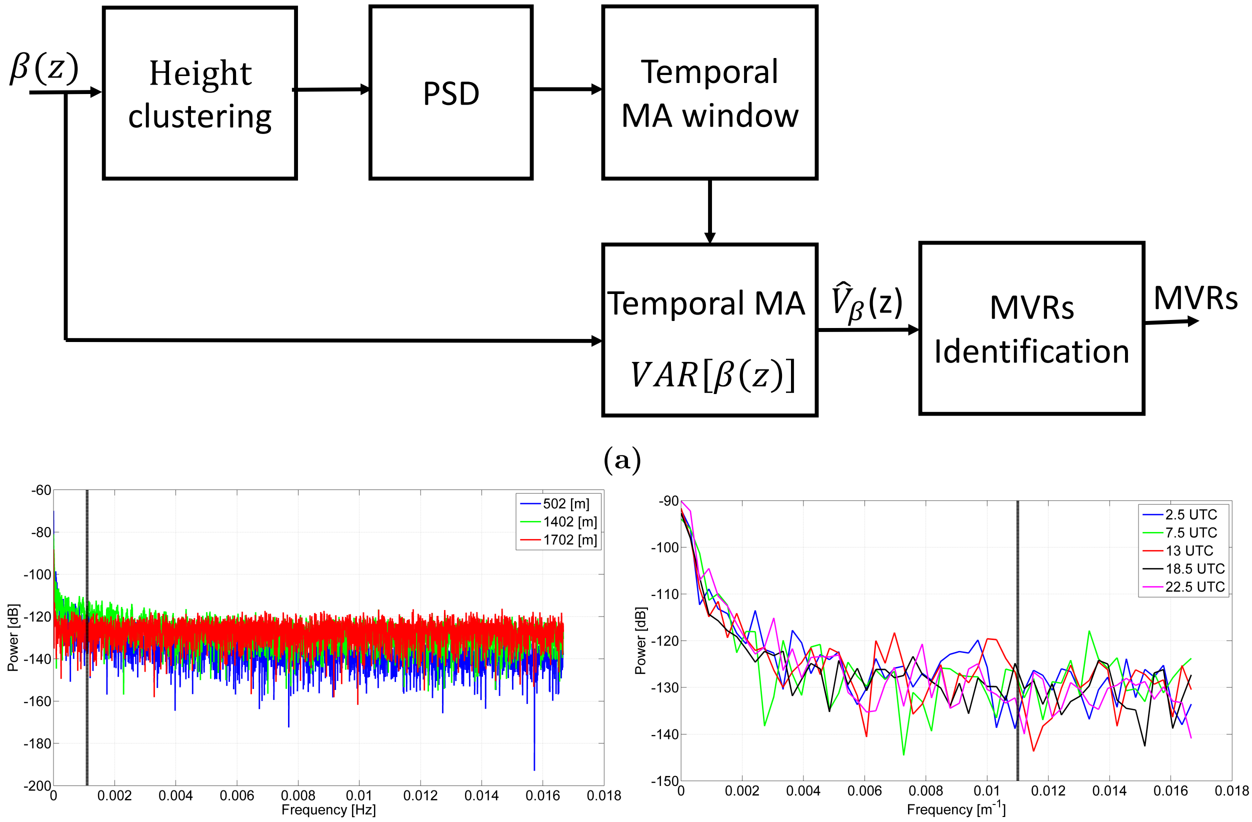

(a)

(b) **(c)**

Figure 4.5: (a) Block diagram outlining the signal processing steps in temporal variance processing for SBLH estimation. Input backscatter data, $\beta(z)$, is first divided in height clusters (Fig. 4.4a). Next, the representative time series of each cluster is used to estimate its PSD and from this the MA window length. Temporal variance of the raw backscatter signal at each point in the height grid is calculated using a rectangular MA window. Finally, MVRs are identified and used as proxies for SBLH. (b) PSD of the three representative profiles (center of each height cluster) of Fig. 4.4a. The PSDs at each height (509, 1409, and 1783 [m]) are different at the lowest frequencies (f_c=0.0011 [Hz]) because they contain different atmospheric information related to the three distinct clusters. However, these three PSDs start overlapping each other above f_c, where the noise power is dominant. The cutoff frequency, thus chosen, is marked by the dotted vertical line at f_c=0.0011 [Hz]. (c) Following similar approach as for temporal PSD, the spatial PSD for the five representative profiles at the center of the five time clusters is calculated and the spatial MA window is determined to be at 0.011 [m^{-1}].

variance follows similar steps.

4.2.2 Power spectral density

The PSD, which is the distribution of the signal over frequency spectrum, can be determined from the auto-correlation function, $R_x(\tau)$, of the signal. The auto-correlation function of a signal provides information about the PSD of the signal via its change with respect to the time difference variable, τ. This is due to the fact that the when auto-correlation function of a signal changes slowly with respect to τ, the signal also experiences slow changes over time. Similarly, when the auto-correlation function changes rapidly with respect to τ, it signifies a signal with rapid changes over time *Brown and Hwang* [1997].

For a stationary signal, the PSD can be expressed as

$$S_x(jw) = \int_{-\infty}^{\infty} R_x(\tau) e^{-j\omega\tau} d\tau, \tag{4.7}$$

where $\omega = 2\pi f/fs$, with fs being the sampling frequency, is the normalized frequency, and

$$R_x(\tau) = E\left[x(t)x(t+\tau)\right], \tag{4.8}$$

and τ is the time difference variable.

Fig. 4.5b shows the PSDs of the three representative profiles used for temporal processing (Fig. 4.4a). As evidenced by the three PSDs, most of the signal power is concentrated in frequencies below $f_{tmp} = 1.1$ [mHz], which translates to a temporal window, $w_{tmp} = 1/f_{tmp}$ $= 15$ [min]. Similarly in Fig. 4.5c, the PSDs of the five representative profiles used for spatial processing (Fig. 4.4b) result in a spatial window length, w_{spa}=90 [m] ($f_{spa} = 0.0111$ [m^{-1}]).

4.2.3 Variance processing

Once the MA window length has been estimated the next step is to calculate the MA variance. In the following, the formulation is presented for the temporal variance, only. Since spatial processing follows similar approach, the formulation for spatial variance is omitted for brevity.

For a given time series of backscatter data, $\beta(t, z_p) = \left[\beta(t_1, z_p), \beta(t_2, z_p), \ldots, \beta(t_N, z_p)\right]$ where N is the total number of time samples and $z_p, p = 1, \ldots, P$ is a p-th discrete height in the height grid, the temporal variance is calculated as

$$Var[\beta_p(k)] = \frac{1}{M} \sum_{k-\frac{M-1}{2}}^{k+\frac{M-1}{2}} \left[\beta_p(k) - \mu_p(k)\right]^2, k = \frac{M-1}{2}, \ldots, N - \frac{M-1}{2}, \tag{4.9}$$

Table 4.1: Comparison of temporal and spatial variances.

Feature	TVAR	SVAR
Raw time resolution (Jenoptik)	15 s	15 s
Raw spatial resolution (Jenoptik)	15 m	15 m
Effective time resolution	15 min	15 s
Effective spatial resolution	15 m	90 m
No. of samples for processing	60	6
Online processing	No	Yes

where M is the window length (in samples), $\mu_p(k)$ is the MA mean given by

$$\mu_p(k) = \frac{1}{M} \sum_{k-\frac{M-1}{2}}^{k+\frac{M-1}{2}} \left[\beta_p(z)\right], k = \frac{M-1}{2}, \ldots, N - \frac{M-1}{2}. \qquad (4.10)$$

Repeating the same calculation for all points P time series are obtained.

Fig. 4.6a and Fig. 4.6b show the temporal and spatial variance for the time intervals 00:00-05:00 [UTC], 10:00-16:00 [UTC], and 21:00-24:00 [UTC] corresponding to the early morning SBL, the day-time ML, and the night-time SBL, respectively. To compose Fig. 4.6a we plot the temporal variances $Var[\beta_p(k)]$ as a function of the discrete heights, $p = 1, \ldots, P$ and for the time clusters indicated. It is pertinent to point out that both temporal/spatial variance methods capture fairly well the morphological features of atmospheric aerosols almost matching each other (compare variance behaviour in Fig. 4.6a, 4.6b). On one hand, the day-time variance (10-16 UTC panel) remains almost constant near the surface ($\leq$ 600[m]) due to the strong mixing process and becomes higher towards the EZ. On the other hand, the night-time variance (0-5, 21-24 UTC panels) shows MVRs right from near the surface ($\geq$ 400 [m]). There are also some differences between the temporal and spatial variance profiles mainly due to the different temporal and spatial resolutions involved (Tab. 4.1).

In order to cross-examine temporal and spatial variances in more detail, Fig. 4.7c analysis these two variances in terms of time-series at specific heights and at time-instants.

Fig. 4.7a and Fig. 4.7b show temporal and spatial variances time-series, respectively, along with associated error-bars at three representative heights (509 [m], 1409 [m], 1783 [m] as defined in Fig. 4.4a). It emerges that the two variance methods follow the backscatter changes in good agreement with each other when looked over time.

Fig. 4.7c shows the five vertical profiles (2.5, 7.5, 13, 18.5, 22.5 UTC) of temporal and spatial variances corresponding to the five representative profiles defined in Fig. 4.4b. It can be noticed that the vertical profiles of two variance methods agree well within each of the five time panels.

Following the discussion above, the ergodicity of the lidar backscatter signal can be

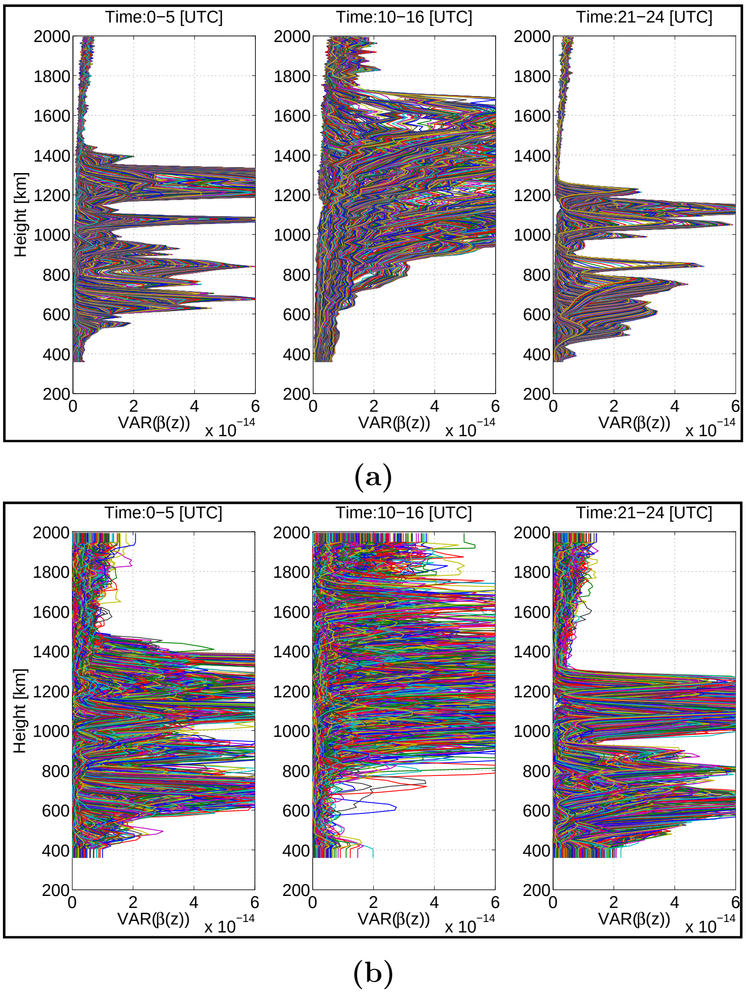

Figure 4.6: Comparison of temporal and spatial variance profiles at three different time clusters corresponding to the early morning SBL (0-5 [UTC]), day-time ML (10-16 [UTC]), and night-time SBL (21-24 [UTC]). (a) Temporal variance profiles at each time-instant corresponding to the raw backscatter data. Focusing on the lowest 800 [m] of the variance profiles it is clear that variance changes during the nocturnal SBL are well pronounced marking MVRs. However, during the day-time and due to mixing of aerosols, these variance profiles do not exhibit such behavior and remain more or less constant. Moreover, considering the heights corresponding the ML top, it reveals that there is a maximum variance before it drops to low values in the free troposphere. Note that the profiles within the span of window-length correlate and, therefore, for SBLH calculations one profile from the center of intervals corresponding to the temporal window length is used. (b) Following the similar line of reasoning, the behaviour of spatial variance is observed to be consistent with the temporal variance albeit the magnitudes are different sometimes.

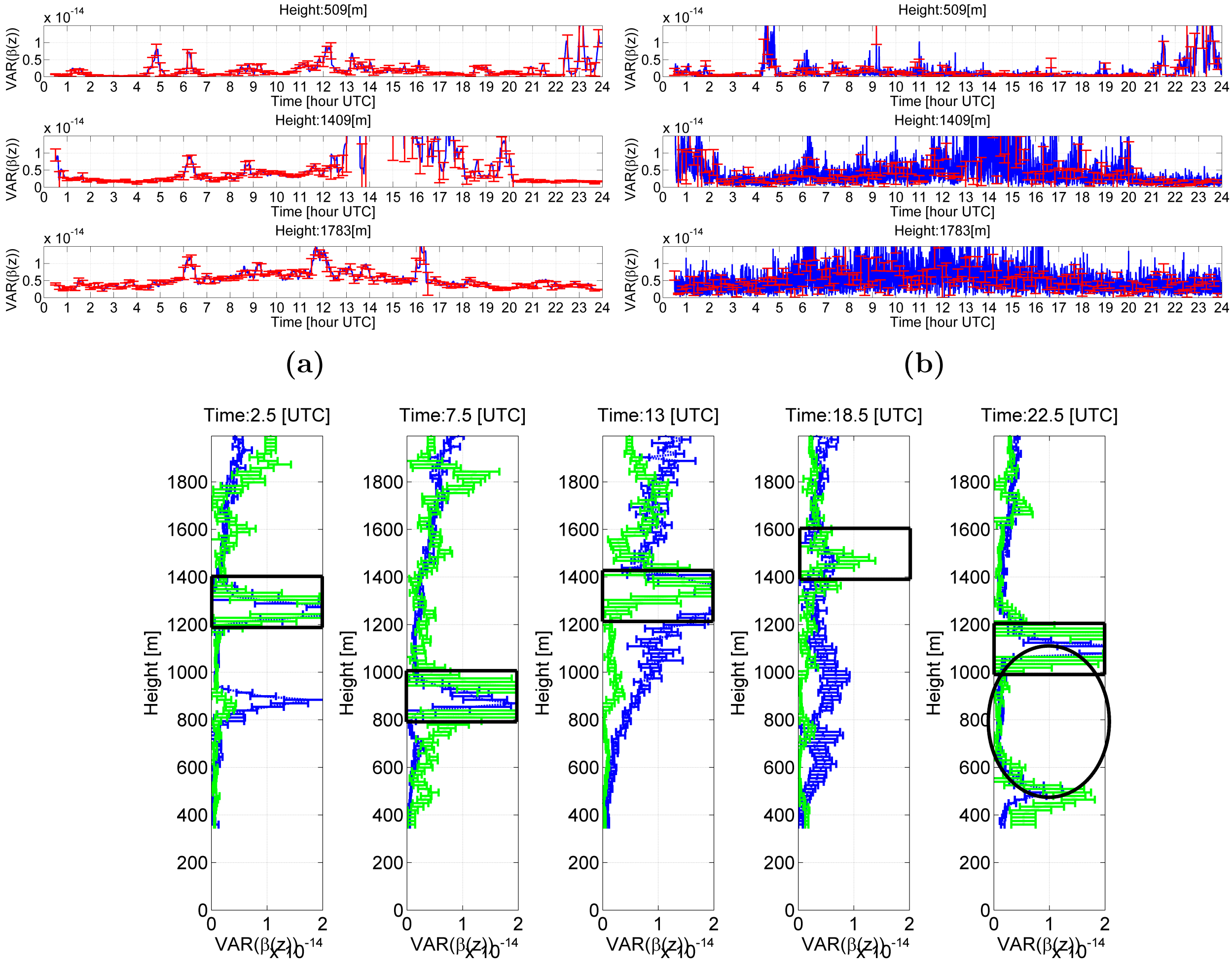

(a)

(b)

(c)

Figure 4.7: An in-depth look at the temporal and the spatial variance in terms of their behaviour in time and height domain. (a) 24-h time series for the temporal variance of Eq. 4.9 along with error-bars at three representative heights corresponding to the center of the three clusters shown in Fig. 4.4a. (b) 24-h time series for the spatial variance (spatial counterpart of Eq. 4.9, $\beta_k(p)$) along with error-bars at the same three height levels as in Fig. 4.7a. (c) Temporal variance (blue trace) and spatial variance (green trace) profiles at time instants corresponding to the center of the time clusters presented in Fig. 4.4b. It is observed that MVRs (as proxies for SBLH stratification) exist only during night-time whereas maximum variance is attained at the top of the ML during the day-time (10-16 UTC) and RL layer during the night-time (0-5, 21-24 UTC).

established by comparing temporal and spatial variance time-series and vertical profiles shown in Fig. 4.7a, Fig. 4.7b, and Fig. 4.7c. By observing the changes of variance in these three figures at specific heights and times, it is clear that the two variance methods identify similar physical behaviour in time and height domains.

4.2.4 SBLH retrieval from MVRs

The first step towards SBLH estimation is to identify MVRs in the backscatter variance profiles of Fig. 4.7c. In the following, only the temporal variance will be discussed, since the method to estimate the SBLH is completely analogous for the spatial case.

The simplest way to identify MVRs within a given temporal variance profile is -what we call in this PhD thesis- ***threshold minima***. A user-defined threshold is introduced to avoid false minima due to noise. The search for MVRs can be limited to the first one km of the variance profile since the SBLH is almost always lower than 1 km *Stull* [1988]. Mathematically, the determination of a height interval associated to a MVR, I_{MVR}, can be expressed as

$$I_{MVR} = z\Big|_{\left[Var^{tmp}(z)-Var^{tmp}_{min}\right]\geq\gamma}, z\epsilon[z_1, z_2] \tag{4.11}$$

where $Var[\beta_p(k)]$ is the temporal variance of Eq. 4.9 re-written as a function of height z (continuous rather than discrete notation has been used to simplify notation), Var^{tmp}_{min} is the minimum of the variance in the search region, and z_1 and z_2 are the lower and the upper boundaries, and γ is a threshold usually chosen about 5-10 times the Var^{tmp}_{min}.

Following Eq. 4.11, a MVR is encircled in the Fig. 4.7c at 23:00 UTC at the height range of 500-1000 [m]. Similarly, maximum variance regions, indicative of the top of ML and RL, have also been highlighted by rectangular boxes.

Once MVRs, usually several ones are identified in a given variance profile, the next step is to estimate the SBLH. In case of a single MVR, the SBLH is estimated as the height corresponding to the *absolute minimum of the variance* within the MVR.

In case of multiple MVRs the initial guess for the SBLH is helped by the RS estimate. Subsequent time estimates of the SBLH take into account the difference between the actual MVRs and past SBLH estimates.

In Chap. 5 we will see that a more advanced algorithm to do this is the Variance-EKF.

4.2.5 Results and discussion

Two study cases have been considered to test the approach described above. The first case, 22.04.2013, is a pre-dominantly clear-sky day with an early morning cloud at the top of the RL. Fig. 4.8a shows the backscatter colorplot along with SBLH estimates using the

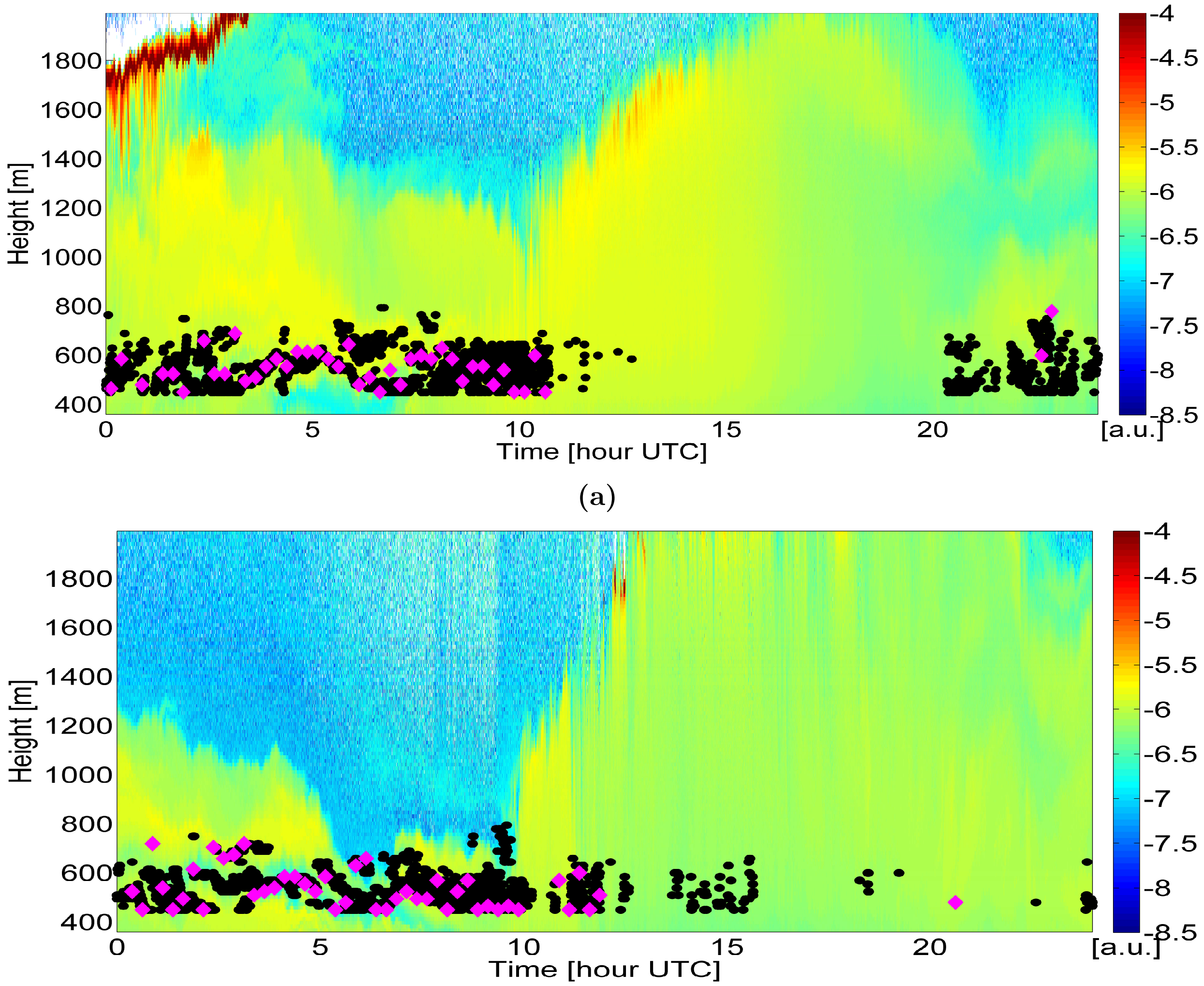

(a)

(b)

Figure 4.8: Study cases for SBLH estimation using the threshold-minima method to identify MVRs. (a) Case-1 (22.04.2013): A predominantly clear-sky day with only a short time (0-4 UTC) early morning cloud at the top of the boundary-layer. Color-plot of attenuated backscatter for 24-h of data along with SBLH estimates using temporal (magenta diamonds) and spatial (black circles) variance processing. SBLH estimates lie within the range of 400-600 [m]. For temporal processing, an estimate of SBLH is available every 15 min and for spatial processing every 15 s. (b) Case-2 (25.04.2013): Synoptic condition in the evening with mixing prevailing during the night-time. Attenuated backscatter color-plot, along with SBLH estimates using temporal and spatial processing. SBL only exists in the early morning time extending from the night of the previous day. Due to synoptic mixing in the evening and night-time, SBL doesn't form and no MVRs exist.

temporal and spatial variance processing. Since temporal variances are calculated with a MA window of 15 [min], SBLH estimates are shown every 15 [min]. In contrast when spatial variances are calculated, SBLH estimates are available with the raw time resolution of 15 [s]. Another important distinction is that temporal variance processing provides only a few SBLH estimates in the evening as compared to spatial variance processing. This may be due to the fact that since only one temporal variance profile is used for SBLH estimation every 15 [min], it is possible that in those profiles it is difficult to discern the right variance minima due to relative magnitude of noise or that no MVR exists at all.

The second study case (25.04.2013) is also a clear-sky day but with synoptic mixing conditions prevailing in the evening and sustaining during night-time. Fig. 4.8b shows the backscatter color-plot along with SBLH estimates for this day. Because of the synoptic mixing in the evening, stable conditions do not develop and the SBLH estimates from both, temporal and spatial variance processing do not detect any MVR.

The SBLH estimation method presented above works reasonably well, though with a high RMSE (about 100 [m] in Fig. 4.8a, and Fig. 4.8b), only under simple atmospheric conditions and when the atmosphere (MVRs) do not change quickly with time. In more complex cases and for better tracking of SBLH (lower RMSE) a more involved processing algorithm such as the EKF is necessary (Chap. 5, Sect. 5.2.1). For physical consistency and reliability of SBLH estimates a cooperative instrument such as a MWR can also be incorporated (Chap. 5, Sect. 5.2.3).

For the sake of completeness with the aim of this Chapter (non-synergetic SBLH estimation) next we present a more sophisticated method for SBLH estimation than the *THRESHOLD MINIMA METHOD* discussed in Sect. 4.2.4. This alternative method is the EKF-based estimation algorithm (to be discussed in Chap. 5).

The ***EKF-based SBLH estimation algorithm*** is applied to the lidar data collected by a *Vaisala CT25K* ceilometer during the HOPE campaign at Jülich, Germany. Two experimental cases are discussed next:

Case 1. - The first case comes from 20th of April, 2013, 22.9-24.0 UTC corresponding to a day with typical stratification of the aerosols in the SBL and thus, it serves as a good study case. A radio-sonde was launched at 23:00 UTC. The filter is initialized with the SBLH estimate obtained by the potential temperature gradient method *Collaud Coen et al.* [2014] from the temperature profile measured by the radio-sonde. The SBLH EKF estimates over one-hour period (22.9-24.0 UTC) are shown in Fig. 4.9a. SBLH estimates from the MWR *Stull* [1988] along with their uncertainty are also plotted in the form of error-bars. Visual inspection of the figures reveals a good agreement between the lidar and MWR-based estimates of the SBLH. The sudden jumps between 22.9-23.3 UTC in the SBLH estimates from the MWR (right-hand side of the black vertical line), where the agreement with the ceilometer-EKF estimates is not so good, can be attributed to the limitations of the SBLH estimation method from the MWR (Sect. 4.3) and its poor vertical resolution.

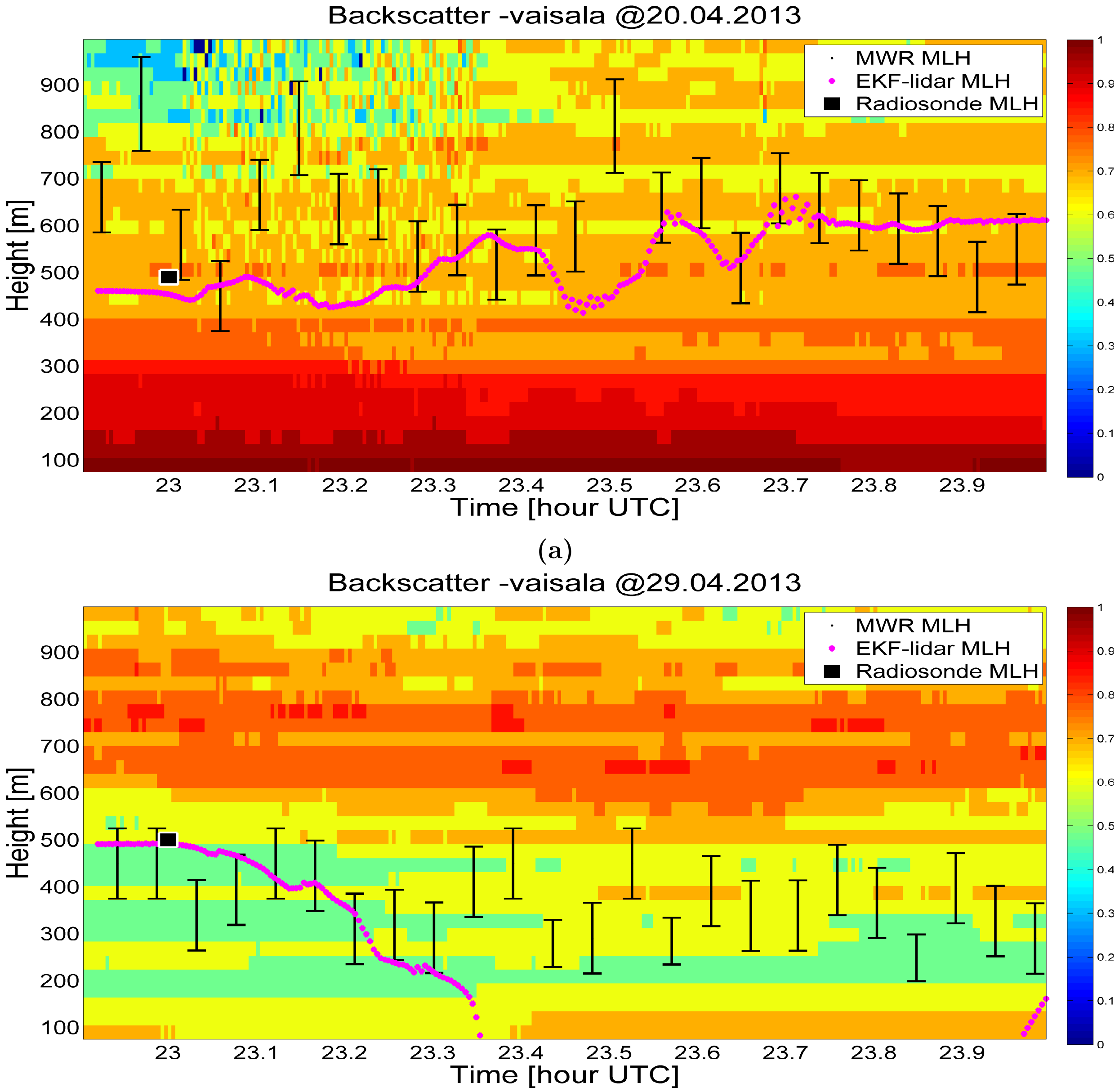

(a)

(b)

Figure 4.9: (a) Color-plot of the backscattered signal from Vaisala CT25k ceilometer during the HOPE campaign, on 20th of April, 2013. ABLH estimate from radiosonde (black square) and MWR (black error-bars) are also shown. (b) A limiting-case example for the presented method involving shallow mixing and a lack of aerosol stratification in the SBL (29th of April, 2013). Color traces as in Fig. 4.9a.

Case 2. - The EKF method presented in this work becomes limited under weakly stable conditions or in cases where aerosol stratification is not so uniform. In such conditions the variance profile of the backscatter signal does not provide a clear signature of the MVRs owing to the lack of clearly resolved aerosol layers. Fig. 4.9b shows the color-plot of the backscatter data for 29th April, 2013, 22.9-24.0 UTC. As it can be observed from the radiosonde and MWR SBLH estimates, the SBL mostly lies in the range between 250-500 m. This yields a nearly flat MVR (small "b" parameter in Eq. 4.1), equivalently, a wide Gaussian bell) where the KF cannot decide. Because, in this height range the aerosol load is very low the EKF fails after a few iterations. It is, therefore, concluded that under low aerosol load conditions a cooperative instrument, such as the MWR, can be used in a synergetic way by combining the physical temperature profile provided by the MWR with the good spatial and temporal resolution of the lidar. This will be tackled in Chap. 5.

4.3 SBLH estimation using MWR observations

From the five idealised model profiles (Sect. 4.1.2), the problem of SBLH estimation from MWR data can be stated as a Least SQuares (LSQ) problem as follows: Given (i) the profile of the raw potential temperature [i.e., the retrieved potential temperature from MWR measurements, in what follows, $\theta_{MWR}(z)$] and, (ii) surface potential temperature, θ_s, from the MWR, one wishes to estimate: (a) the model SBLH, h, and (b) the model RL potential temperature, θ_0, by using the objective function

$$\min\left\{\left\|\theta_{MWR}(z)-\theta\left(z,\theta_s,\vec{\mathbf{x}}_k\right)\right\|^2\right\}\Big|_{\vec{\mathbf{x}}=[h,\theta_0,aux]}. \qquad (4.12)$$

In Eq. 4.12, $\vec{\mathbf{x}}$ is the objective vector to be solved, and "aux" denotes auxiliary solving parameters such as temperature jump at the top of the SBL, $\theta_{\Delta h}$, for the mixed-linear model, model order, α (typical value of $2-3$), for the polynomial profile, and *integral depth scale* within the SBL, $H_{\Delta\theta}=\frac{\int_0^h[\theta_0-\theta(z)]d\theta}{\theta_0-\theta_s}$, for the exponential model.

MWR data processing - MWR-retrieved potential-temperature profiles, $\theta_{MWR}^{raw}(z)$, are non-uniformly sampled along the height dimension due to the coarse vertical resolution of the instrument, which decreases with height. As a first processing step, $\theta_{MWR}^{raw}(z)$, is interpolated to obtain a uniformly sampled profile, $\theta_{MWR}(z)$. Here, it is pertinent to mention that this interpolation step does not alter the inherent height-varying resolution of the potential temperature data retrieved from MWR measurements. For interpolation purposes a cubic spline interpolation is used. The second processing step is fitting the five SBL model profiles (Eqs. 4.2-4.6) to the uniformly-sampled potential-temperature profile, $\theta_{MWR}(z)$, by using a LSQ approach. The best model is selected based on a mMSE criterion.

Fig. 4.10 shows an example of MWR-retrieved potential temperature profile (blue crosses), $\theta_{MWR}(z)$, from the HOPE campaign data, 24.04.2013 at 21:00 UTC. The five idealized mod-

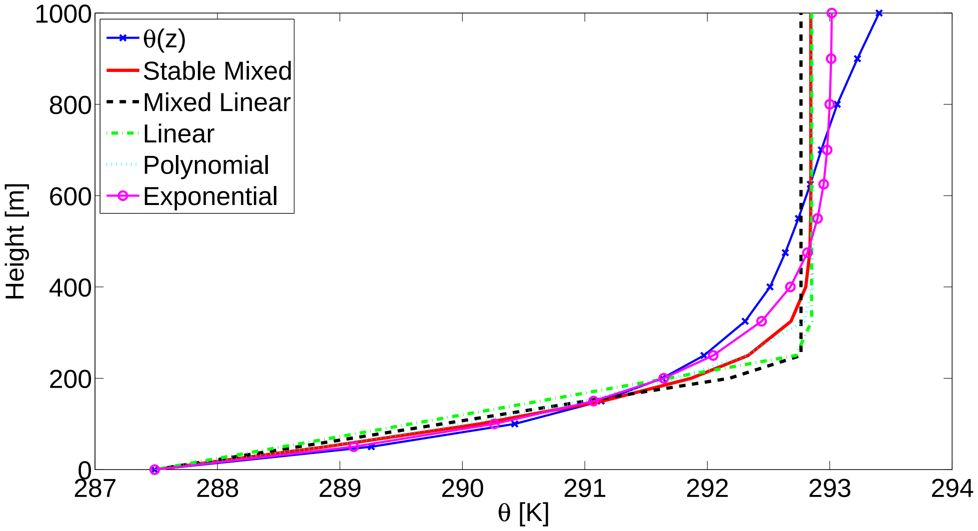

Figure 4.10: MWR-retrieved potential temperature profile at 21:02 UTC (24.04.2013, HOPE campaign, Jülich, Germany), fitted with the five idealized physical models. Exponential model fits best with the mMSE.

els of Eqs. 4.2-4.6 are also plotted. It is observed that the polynomial and the exponential models provide best fits with a mMSE of 0.29 [K] and 0.15 [K], respectively. The *polynomial model* is chosen in-spite of a slightly higher RMSE since the parameter α can be user-defined and made consistent across a set of all profiles/data-sets. Note, that all the five idealized model profiles significantly deviate from the retrieved potential-temperature profile at the RL heights as the real atmosphere hardly ever behaves in an idealized way. Furthermore, MWR coarse vertical resolution and limited accuracy of the retrieved temperature profile contribute to add-on uncertainty, Δz_{MWR}, especially at higher altitudes where the information content degrades.

4.4 Conclusions

Aerosol stratification in the SBL has been related and formulated in terms of MVRs in the lidar backscatter signal. For this purpose, two variants of the variance estimation method, temporal and spatial variance processing, have been introduced. A detailed study and comparison of the two methods has been presented. A simplistic method for SBLH estimation using MVRs has also been presented. Two study cases were considered: A typical clear-sky day with an early-morning boundary-layer cloud at the top of the RL, and a another clear-sky day with synoptic mixing condition prevailing in the evening and night time. It has been concluded that the SBLH estimation could benefit from noise filtering and more involved signal processing methods such as an EKF.

Next, application of a novel method for the estimating the SBLH, EKF-based SBLH estimation, from ceilometer-lidar data has been presented. Height-resolved temporal variance of the backscatter lidar data has been used as the proxy to account for the variations on the atmospheric aerosols content. The minimum variance regions in the vertical profiles of this variance are representative of the aerosol layers in the SBL and are modelled by an inverted Gaussian-like function with the SBLH as the key parameter to estimate. An EKF filter has been used to retrieve and track the SBLH and MVR model parameters over time. Two cases highlighting the strengths and limitations of the method have been discussed. The estimates of the SBLH have been validated by comparison with MWR SBLH estimates. A good agreement between the two instruments has been shown.

Finally, five idealized models from the literature (Sect. 4.1.2), which model the temperature profile in SBL conditions, have been applied to MWR-retrieved temperature profiles for the SBLH estimation. These five idealized models are fitted to the measured one by using the LSQ approach.The best fitting model is chosen based on mMSE criteria. It has been observed that the exponential model provides the best fitting for majority of the cases.

Chapter 5

Synergetic estimation of the stable-boundary-layer height

A synergetic approach for the estimation of Stable Boundary-Layer Height (SBLH) using lidar and Microwave Radiometer (MWR) data is presented. Vertical variance of the backscatter signal from a ceilometer is used as an indicator of the aerosol stratification in the nocturnal stable boundary-layer. This hypothesis is supported by a statistical analysis over one month of observations. Thermodynamic information from the MWR-derived potential temperature is incorporated as coarse estimate of the SBLH. Data from the two instruments is adaptively assimilated by using an Extended Kalman Filter (EKF). A first test of the algorithm is performed by applying it to collocated Vaisala CT25K ceilometer and Humidity-and-Temperature Profiler (HATPRO) MWR data collected during the HOPE campaign at Jülich, Germany. The application of the algorithm to different atmospheric scenarios reveals the superior performance of the EKF compared to a non-linear least-squares estimator especially in non-idealized conditions.

The contents of this Chapter are part of the paper *Saeed et al.* [2016b] submitted to IEEE Transac. Geosc. Rem. Sensing.

5.1 Introduction

Measurements of ABLH make use of the typical vertical structures of temperature, humidity, wind and aerosol. While aerosol distribution as probed by ground-based lidars is well suited for the estimation of the Convective Boundary Layer Height (CBLH), the estimation of the SBLH is more complex. Many of the techniques presented for the lidar data are a variant of the gradient detection method *Eresmaa et al.* [2006]; *Haeffelin et al.* [2012] and, therefore, suffer from multiple-aerosol-layer attribution problems. This means that under the conditions of multiple aerosol-layers in the boundary-layer these methods are limited in terms of providing a consistent solution due to their non-adaptive nature and lack of physical basis for layer attribution. Some more advanced techniques such as the "Peaks" and "Wavelets" *Haij et al.* [2007], which utilize advanced signal processing, and the Bayesian Selective Method (BSM) *Giuseppe et al.* [2012], which combines data from lidar, a physical boundary-layer model and a climatological data-set in a statistically optimal way, do improve the estimation performance. However, they are still limited by the starting height of full overlap of lidar and the unavailability of lidar data under cloudy and rainy conditions. Furthermore, cooling leads to a higher relative humidity and since the size of the aerosols varies with the moister content *Eresmaa et al.* [2006] due to hygroscopic effects, the higher backscatter coefficient is linked to a higher amount of humidity in the atmosphere.

Most of the previous work for SBLH estimation from temperature data are based on the measurements from RS *Hyun et al.* [2005]; *Angevine et al.* [2006] mainly exploiting temperature profiles. Though MWR can provide continuous time series of temperature profiles *Crewell and Löhnert* [2007], few studies have exploited these data for SBLH estimation. Recently, an approach based on the gradient of the retrieved-potential temperature from a MWR been presented by *Collaud Coen et al.* [2014]. One of the main limitation of MWRs is their low vertical-resolution, thereby the large uncertainty associated with the estimates. Moreover, the temperature profile is over-smoothed especially at higher altitudes, hence missing important features within the retrieved profiles. As a result, MWRs are unable to give accurate indication of the SBLH and the residual boundary-layer height.

Departing from these previous efforts to estimate the SBLH, in this paper we present a combined lidar-MWR approach using an EKF. The approach is based on the hypothesis, whereby stable aerosol layer corresponds to a MVR in the variance profile of the lidar backscatter signal. The hypothesis is based on the fact that during the stable conditions prevailing in the night-time, with minimal to nil convection, and in the absence of mechanical turbulence, which usually results in horizontal stratification of the aerosol layers *Stull* [1988]; *Giuseppe et al.* [2012]; *Haeffelin et al.* [2012]; *Münkel et al.* [2007], the backscatter signal remains almost constant across the layer's vertical span. This minimum variance-behavior is opposite to the maximum variance behavior defining the EZ and CBL *Hennemuth and Lammert* [2006]; *Hooper and Eloranta* [1986].

As discussed earlier, MVRs are not unique due to the presence of multiple layers of aerosols. Moreover, MVRs also get corrupted by the instrument noise (added to the backscatter signal) essentially distorting its shape. In order to overcome the limitations associated with the use of MVRs from the lidar backscatter data alone, the proposed approach is based on the synergy between the lidar and the MWR, whereby the MWR plays a role of layer attributor. Nevertheless, the boundary containing the temperature inversion information should be sufficient to correctly segregate the most relevant MVR within the lidar backscatter variance profile. An estimation algorithm based on an EKF is then applied on the selected MVR to calculate the SBLH with low uncertainty. Unlike the Bayesian Selective Method mentioned earlier, the use of EKF provides statistically optimal estimates by minimizing the mean-square-error over time without the need of averaging the observation data.

Fig. 5.1 illustrates the development of the ABL on 24.04.2013 via the observed potential temperature and backscatter time-height structure over the full diurnal course. Because this day was characterized by weak synoptic forcing and nearly no clouds, ABL development is close to the idealized cases described in the introduction. Since the SBL prevailed until about one hour past sunrise, the aerosol mixing process did not start until about 06:00 UTC when the convection became significant and the convective ML developed. This can well be seen by the neutral conditions, i.e. vertically constant potential temperature. Around sunset (18:30 UTC) mixing recedes and thus aerosol stratification occurs. The extent of aerosol stratification in the SBL is directly linked to the amount of thermal stability in the boundary-layer. Case studies from this day are shown in Sect. 5.2.4. Since CT25k is an old first-generation ceilometer by Vaisala, it has low pulse energy (1.6 μJ/pulse) and low pulse repetition rate (4369 [Hz]) as compared to modern second-generation systems such as CL31 with slightly lower pulse energy (1.2 μJ/pulse) but with almost double pulse repetition rate (8192 [Hz]) *Münkel et al.* [2007]. This explains a poorer SNR from the CT25k side, which causes that the structure of the boundary layer at higher altitudes especially the top of the mixing layer during the day-time is not clearly identifiable (e.g., blurred noisy pattern between 5-18 UTC and 0.5-1.5 km in height).

5.2 Adaptive SBLH detection method

This section tackles the problem of SBLH estimation from lidar and MWR data by following a progressive signal-processing approach: Sect. 5.2.1 and 5.2.2 formulate the problem from the non-synergetic perspective, i.e., estimation of the SBLH from *stand-alone* lidar data (Sect. 5.2.1) and estimation of the SBLH from *stand-alone* MWR data (Sect. 5.2.2). These two formulations are not exclusive but complementary as they pave the way to the topic of synergetic SBLH estimation by using lidar and MWR data (Sect. 5.2.3). Thus, Sect. 5.2.3 merges into a single body the formulations presented in Sects. 5.2.1-5.2.2 to come up with a unified estimation framework that combines both remote sensing instruments.

5.2.1 SBLH estimation from backscatter lidar data and an EKF

In Sect. 4.1.1, the formulation of an inverted Gaussian-like model profile representative of an idealized MVR for stable aerosol layer in the night-time has been presented. In contrast to estimation of the MLH (convective boundary layer, Chap. 3), where the “inputs” or “observables” to the estimator were attenuated backscatter profiles, estimation of the SBLH requires the variance of the backscatter profiles as observables. This is to say that the

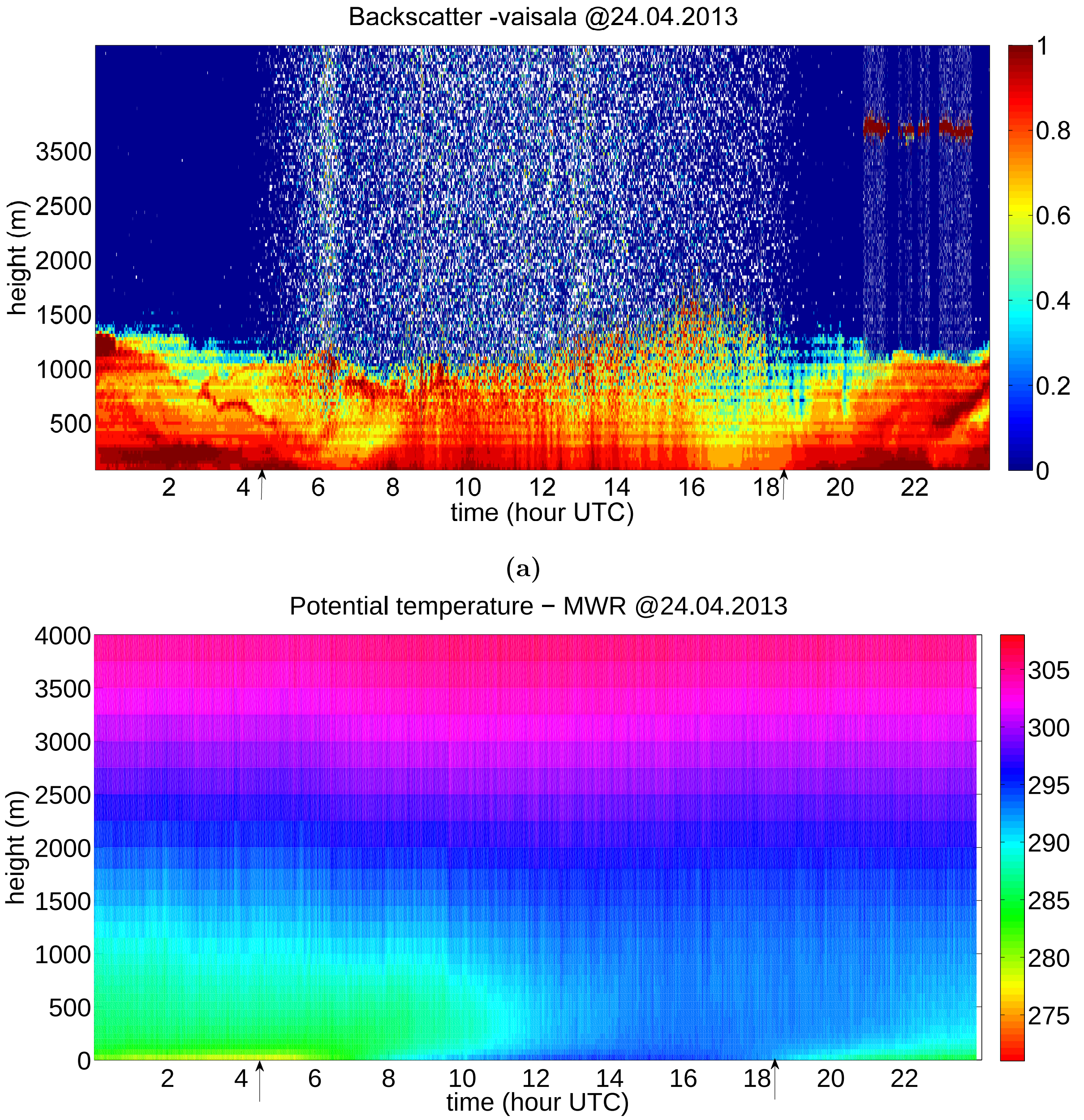

(a)

(b)

Figure 5.1: Measured aerosol backscatter and potential temperature data from 24.04.2013, Jülich, Germany. Vertical arrows mark the sunrise and sunset times. (a) Colorplot of the backscatter profiles measured by the Vaisala CT25k ceilometer. (b) Colorplot from the MWR-retrieved potential temperature data.

model profile of Fig. 4.2 is used to adaptively fit the height-variance profile of the measured lidar data. Towards this end, in the following, we revisit signal pre-processing practicalities associated to computation of the height-dependent variance profiles to be presented to the SBLH estimator. Later, the grounds of SBLH using an EKF are formulated. The EKF is chosen as the adaptive estimator because it minimizes the mean-square-error over time and thus it assimilates the temporal information of the signal optimally. For comparison, a simplified NLSQ formulation is also presented.

Variance of the attenuated backscatter lidar profile as observable: Pre-processing practicalities. - The practicalities presented here are a simplified alternative to the block diagram of Chap. 4, Fig. 4.5a with the exception that a simple rectangular filter is used for vertical (spatial) processing, instead.

Similarly, and as a first step, the noisy attenuated backscatter coefficient, $\beta'(z)$, (Chap. 2, Eq. 2.11) is low-pass filtered to remove the high-frequency noise. Fig. 5.2a shows the basic signal-processing block diagram to estimate the backscatter variance profile, $\hat{V}_{\beta}(z)$, from the noisy attenuated backscatter coefficient profile, $\beta'(z)$. The first step in the processing of $\beta'(z)$ is to denoise it by low-pass filtering (LPF). This gets rid of the high-frequency content of $\beta'(z)$, which is associated to instrumental noise, while retaining the low-frequency content. The later is associated to the noiseless atmospheric backscatter, $\beta(z)$, and related low-frequency atmospheric fluctuations of interest for this study. Formally,

$$\hat{\beta}(z) = \beta'_{LP}(z), \tag{5.1}$$

where a hat "$\hat{\cdot}$" indicates "estimate of" and subscript "LP" indicates low-pass filtering.

The LPF is implemented by using a moving-average filter with a rectangular window length, w. The appropriate window-length is obtained by monitoring kurtosis (K) of the residual high-frequency noise,

$$\hat{v}(z) = \beta'(z) - \beta'_{LP}(z), \tag{5.2}$$

as signal-processing indicator. Thus, the window-length yielding a kurtosis figure closest to 3 (K=3 for a pure Gaussian random process) *Barlow* [1989b] is chosen as the filtering window-length.

Fig. 5.2b1 shows plots of the measured noisy backscatter, $\beta'(z)$, along with the estimated backscatter profile, $\hat{\beta}(z)$, for different window lengths. The estimated backscatter profile using the largest window length (300 [m]) becomes over-smoothed and, as a result, misses detailed atmospheric features. Likewise, the residual high-frequency noise, $\hat{v}(z)$ (Fig. 5.2b2) is far from the typical shape of a Gaussian process as evidenced by an asymmetric distribution of positive/negative noise spikes (K=2.2). On the contrary, the shortest window length tested (60 [m]) significantly leaks noise into $\hat{\beta}(z)$ and also yields K=2.2. A window

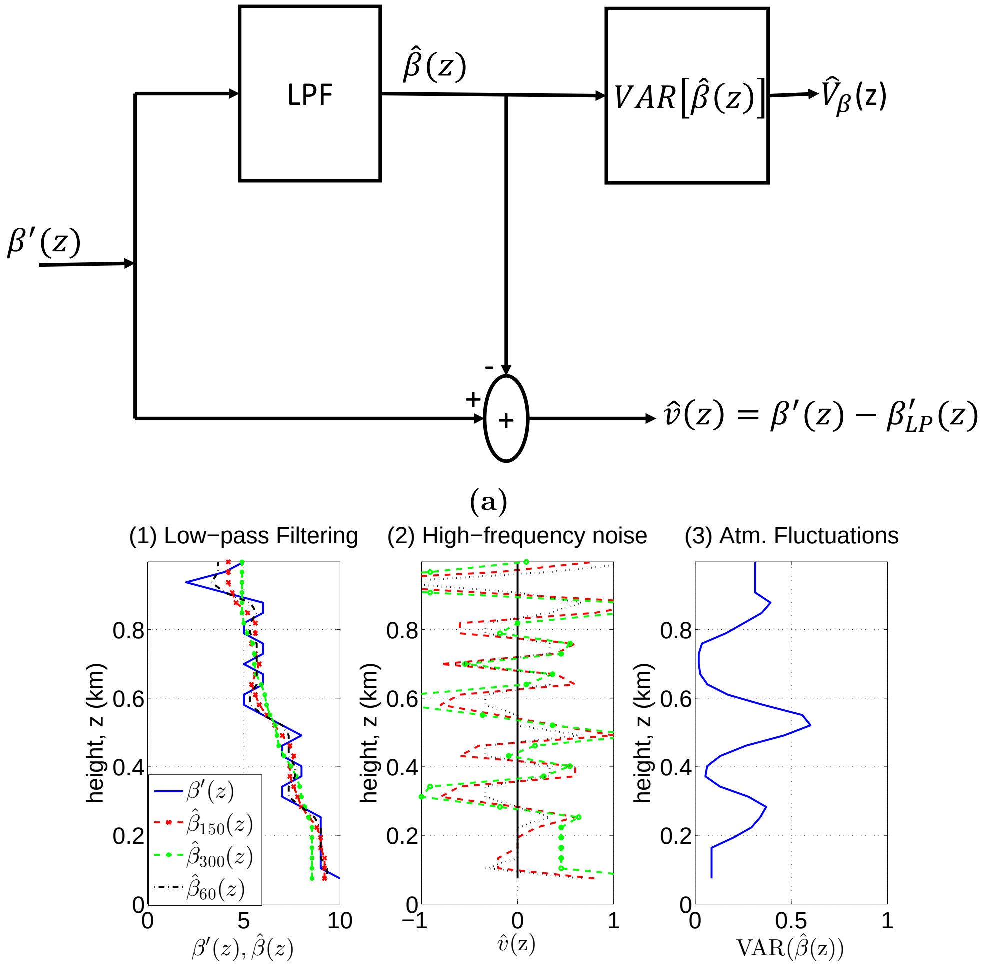

(a)

(b)

Figure 5.2: Ceilometer signal-processing. (a) Block diagram to estimate the variance profile associated to the atmospheric backscatter, $V_{\hat{\beta}}(z)$. (b) Selection of the vertical smoothing window length and calculation of the backscatter variance, 24.04.2013, 21:00 UTC. (1) Vertical profiles of the de-noised backscatter coefficient, $\hat{\beta}_w(z)$, for different window lengths, w=60 [m] (black line with circular markers), 150 [m] (red dashed line), and 300 [m] (green trace with dot markers) (rectangular-window smoothing as low-pass filter (LPF)). (2) High-pass residual noise, $\hat{v}_w(z)$, for the different window lengths chosen. (3) Estimated variance, $\hat{V}_\beta(z)$, for window length chosen (150 [m]) with two MVRs between the height ranges of approximately 300-500 [m] and 550-900 [m].

length of 150 [m] gives the best results for $\hat{\beta}(z)$ as it filters most of the high frequency instrumental noise along with preserving the atmospheric features of the signal and yielding a fairly symmetric noise distribution for the residual noise with K=3.1 (i.e., approximately Gaussian).

The next processing step to estimate the height-dependent variance profile in Fig. 5.2a is associated to the atmospheric backscatter, $\hat{V}_\beta(z)$, given the estimated backscatter profile, $\hat{\beta}(z)$. At this point we use that

$$\hat{V}_\beta(z) \cong V_{\hat{\beta}}(z), \tag{5.3}$$

where $V_{\hat{\beta}}(z)$ represents the vertical variance of $\hat{\beta}(z)$ (see block diagram in Fig. 5.2a). For simplicity, the window length associated to this moving-variance calculation centered at height z has been kept the same as that of the denoising LPF. Fig. 5.2b3 shows the variance profile calculated using the selected window length of 150 [m]. Example variance profiles (Fig. 5.3a) reveal the occurrence of up to two to three MVRs within one profile. During the course of two hours in the evening of 24.04.2013 MVRs between 300-600 [m] can be detected.

In order to further investigate and validate the existence the of MVRs and to prove their relation with the nocturnal SBL, a data-set of 28 days from HOPE campaign starting from 15.04.2013 until 14.05.2013 is used. Cloudy and rainy conditions are filtered out with a resolution of 30 min. Vertical variance of the filtered backscatter data in the first km in height is calculated and averaged over bins of 30-min in time and 200-m in height. MVRs within each time-height bin are determined by the local minima in the averaged vertical variance profiles. Considering up to two MVRs in one profile, the diurnal cycle of frequency of occurrence (Fig. 5.3b) reveals frequent MVR occurrence in the altitude range between 200 and 800 [m] during night-time which fades out towards daytime. The similarity of the MVR diurnal cycle with the typical behaviour of the SBL supports our hypothesis to use MVRs as proxy for SBL.

SBLH estimation using an EKF. - The formulation of EKF for SBLH estimation is based on similar approach as for MLH (Chap. 3, Sect. 3.2.1). From this background, the four characteristics parameters of model Eq. 4.1 are assembled into the state vector,

$$\mathbf{x}_k = [z_{SBL,k}, b_k, B_k, d_k]^T, \tag{5.4}$$

which is to be estimated at each successive discrete time, t_k.

An EKF is essentially based on two models, the *measurement model*, and the *state-vector model*:

Measurement Model - The measurement model relates the atmospheric state vector, $\mathbf{x}_k$,

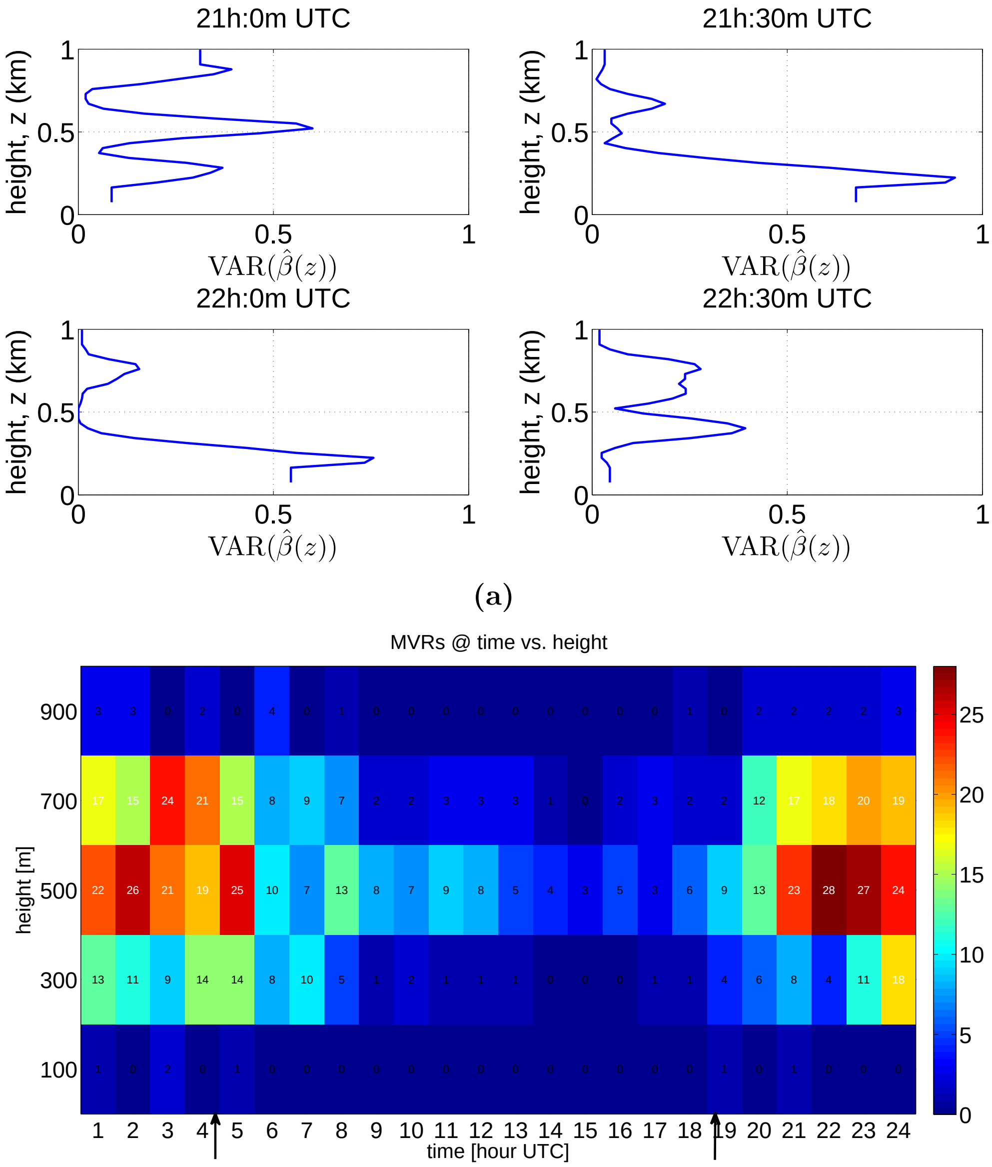

height [m]	1	2	3	4	5	6	7	8	9	10	11	12	13	14	15	16	17	18	19	20	21	22	23	24
900	3	3	0	2	0	4	0	1	0	0	0	0	0	0	0	0	0	1	0	2	2	2	2	3
700	17	15	24	21	15	8	9	7	2	2	3	3	3	1	0	2	3	2	2	12	17	18	20	19
500	22	26	21	19	25	10	7	13	8	7	9	8	5	4	3	5	3	6	9	13	23	28	27	24
300	13	11	9	14	14	8	10	5	1	2	1	1	1	0	0	0	1	1	4	6	8	4	11	18
100	1	0	2	0	1	0	0	0	0	0	0	0	0	0	0	0	0	0	1	0	1	0	0	0

(a)

(b)

Figure 5.3: (a) Vertical variance profiles based on the ceilometer measured aerosol backscatter data showing MVRs in the height range of $300 - 600$ m, 24.04.2013, 21:00-22:30 UTC. (b) Diurnal cycle of MVR occurrence based on one month of observations in April/May 2013. Number of MVR occurrence within 1 hr and 200 m is color coded. Vertical arrows mark the mean sunset and sunset times.

to the measurement vector, $\mathbf{z}_k$,

$$\mathbf{z}_k = h(\mathbf{x}_k) + \mathbf{v}_k, \tag{5.5}$$

where h is the SBL measurement function given by Eq. 4.1, and $\mathbf{v}_k$ is the observation noise which consists of measurement noise as well as modelling errors. In Eq. 5.5 above, $\mathbf{z}_k$ refers to the observables formed from the estimated backscatter variance (Eq. 5.3) at each time t_k, that is,

$$\mathbf{z}_k = \hat{V}_\beta(\mathbf{z})\Big|_{t=t_k} = \Big[\hat{V}_\beta(z_1), \hat{V}_\beta(z_2), \ldots, \hat{V}_\beta(z_N)\Big]_k . \tag{5.6}$$

At this point it is worth noticing that while z stands for the height variable, $\mathbf{z}_k$ and $\hat{\mathbf{z}}_k$ are the actual and the estimated observation vector (also called *measurement* vector).

In the extended Kalman filter (EKF), the non-linear model function h is linearized by calculating its Jacobian (or observation matrix $\mathbf{H}_k$) with respect to the state vector. The filter output at time instant k can then be written as

$$\hat{\mathbf{z}}_k = \mathbf{H}_k \hat{\mathbf{x}}_k^-, \tag{5.7}$$

where

$$\begin{aligned} \mathbf{H}_k(z;\mathbf{x}) &= \left[\frac{\delta h(z)}{\delta z_{SBL}} \; \frac{\delta h(z)}{\delta b} \; \frac{\delta h(z)}{\delta B} \; \frac{\delta h(z)}{\delta d} \right]\Bigg|_{\mathbf{x}=\hat{\mathbf{x}}_\mathbf{k}^-}, \\ &= \Big[\mathbf{H}_k^1 \; \mathbf{H}_k^2 \; \mathbf{H}_k^3 \; \mathbf{H}_k^4 \Big]_{N\times 4}, \end{aligned} \tag{5.8}$$

and

$$\mathbf{H}_k^1(z_{SBL}, b) = \frac{\delta h(z)}{\delta z_{SBL}} \tag{5.9}$$

$$= Bb^2 \left(z - z_{SBL}\right) e^{-\frac{1}{2}\left[b(z-z_{SBL})\right]^2}, \; z \in [z_1', z_2'], \tag{5.10}$$

$$\mathbf{H}_k^2(z_{SBL}, b) = \frac{\delta h(z)}{\delta b} \tag{5.11}$$

$$= -Bb \left(z - z_{SBL}\right)^2 e^{-\frac{1}{2}\left[b(z-z_{SBL})\right]^2}, \; z \in [z_1', z_2'], \tag{5.12}$$

and

$$\mathbf{H}_k^3(B, d) = \frac{\delta h(z)}{\delta B} \tag{5.13}$$

$$= e^{-\frac{1}{2}\left[b(z-z_{SBL})\right]^2}, \; z \in [z_1, z_1') \cup (z_2', z_2], \tag{5.14}$$

$$\mathbf{H}_k^4(B,d) = \frac{\delta h(z)}{\delta d} = 1,\ z \in [z_1, z_1') \cup (z_2', z_2]. \tag{5.15}$$

In Eq. 5.7, above, $\hat{\mathbf{x}}_k^-$ is the state-vector estimate prior to assimilation of the measurement at time t_k and $\hat{\mathbf{z}}_k$ is the "projected" measurement estimate from the filter.

Range intervals $[z_1', z_2']$ and $[z_1, z_1') \cup (z_2', z_2]$ respectively define the measurement-model "fitting" ranges inside and outside the MVR (Fig. 4.2). In order to assimilate the thermodynamic information of the SBL, outer boundaries z_1 and z_2 are assessed synergetically from MWR estimates of SBLH (see Sect. 5.2.2).

State-vector model - The state-vector model essentially describes the temporal projection of the state-vector at each successive time t_k through the recursive equation,

$$\mathbf{x}_{k+1} = \mathbf{\Phi}_k \mathbf{x}_k + \mathbf{w}_k, \tag{5.16}$$

where $\mathbf{\Phi}$ is the transition state matrix (4×4) and $\mathbf{w}_k$ is the state-noise vector with covariance matrix $\mathbf{Q}_k = E\left[\mathbf{w}_k \mathbf{w}_k^T\right]$. A simple Gauss-Markov model, with $\mathbf{\Phi} = \mathbf{I}$ ($\mathbf{I}$ is the identity matrix), can be set as the transition matrix.

The Kalman filtering recursive loop requires three inputs related to the state-vector model: (i) an initial guess of the state-vector, $\hat{\mathbf{x}}_0^- = [z_{SBL,0}, b_0, B_0, d_0]^T$, (ii) an estimate of the initial *a priori* covariance matrix, $\mathbf{P}_0^- = E\left[\mathbf{e}_0^- \mathbf{e}_0^{-T}\right]$ where $\mathbf{e}^- = \mathbf{x}_0 - \hat{\mathbf{x}}_0^-$ is the *a priori* error, and (iii) an estimate of the state-noise covariance matrix, $\mathbf{Q}_k = [w_k w_k^T]$.

The initial *a priori* error covariance matrix, $\mathbf{P}_0^-$, and state-noise covariance matrix, $\mathbf{Q}_k$, can be set as static diagonal covariance matrices of the form, $\mathbf{P}_0^- = diag\left[\sigma_{e,z_{SBL}}^2, \sigma_{e,b}^2, \sigma_{e,B}^2, \sigma_{e,d}^2\right]$ and $\mathbf{Q}_k = Q = diag\left[\sigma_{z_{SBL}}^2, \sigma_b^2, \sigma_B^2, \sigma_d^2\right]$ where σ_X and $\sigma_{e,X}$, $X = (z_{SBL}, b, B, d)$, are the standard deviations of the state-vector parameters and of the *a priori* error on the initial guess, respectively. Subindex "e" stands for "error". These formulations for matrices $\mathbf{P}_0^-$ and $\mathbf{Q}_k$ are simple enough and conveniently model all the case examples (SBL or nocturnal) analyzed in Sect. 5.2.4. Moreover, σ_X and $\sigma_{e,X}$ are represented as proportional to the initial guess $\hat{\mathbf{x}}_0^-$ via factors μ_Q and μ_P, respectively. Therefore,

$$\begin{aligned} \left(\sigma_{e,z_{SBL}}, \sigma_{e,b}, \sigma_{e,B}, \sigma_{e,d}\right) &= \mu_P \left(z_{SBL,0}, b_0, B_0, d_0\right), \\ \left(\sigma_{z_{SBL}}, \sigma_b, \sigma_B, \sigma_d\right) &= \mu_Q \left(z_{SBL,0}, b_0, B_0, d_0\right) \end{aligned} \tag{5.17}$$

or simply $\mathbf{Q}_0 = \text{diag}\left[\left(\mu_Q \hat{\mathbf{x}}_0^-\right)^2\right]$ and $\mathbf{P}_0^- = \left[\text{diag}\left(\mu_P \hat{\mathbf{x}}_0^-\right)^2\right]$. The scaling factors μ_Q and μ_P are user-defined parameters. For example, setting μ_Q and μ_P as 0.1 means the margin of uncertainty associated to $\hat{\mathbf{x}}_0^-$ is 10% and the change in $\hat{\mathbf{x}}_k$ from time instant k to $k+1$ is expected to be within 10% of the values of $\hat{\mathbf{x}}_k$ at time k.

Observation-noise modelling - The observation noise, v_k, is modelled by the noise covariance matrix, $\mathbf{R}_k = E\left[\mathbf{v}_k \mathbf{v}_k^T\right]$, where $E[.]$ is the expectancy or ensemble operator and $\mathbf{v}_k$ is the N-component vector associated to heights, $z_i, i = 1, \ldots, N$. This matrix, $\mathbf{R}_k$, informs the filter about the quality of the observables, $\mathbf{z}_k$, which is a crucial input to the filter in order to assimilate the information conveyed by each new observable at each time step t_k.

One difficulty in the estimation of noise covariance matrix is the need of an ensemble of measurements. In off-line processing applications this difficulty can easily be circumvented by accessing at each time t_k a time window comprising past and future measurements, $\mathbf{z}_k$, from the recorded data with stationary statistics. In an on-line processor this implies an estimation delay equal to the time length of the "future" measurements accessed. In this work we resort to offline processing and stationary statistics. The hypothesis of stationary statistics is a realistic one in stable boundary-layer estimation since in the absence of any mixing process the aerosols tend to remain still aloft for longer periods and hence, the backscatter signal remains approximately constant with time. Therefore, temporal variations on the vertical profiles of $V_{\hat{\beta}}(z)$ on shorter time-scales (e.g., 2 min) provide an estimate of the noise covariance matrix. Formally,

$$\hat{\mathbf{R}}_k = diag\left[\sigma_n^2(z_1), \ldots, \sigma_n^2(z_N)\right]_{t_k} \tag{5.18}$$

with

$$\sigma_n^2(z_i)\big|_{t_k} = V\left[\mathbf{z}_{i,k}\right]\big|_{I_k}, \quad I_k = \left[t_{k-M}, \ldots, t_k, \ldots, t_{k+M}\right], \tag{5.19}$$

where $\mathbf{z}_{i,k}$ is the i-th component of the measurement vector, $\mathbf{z}_k$, at time t_k, which according to Eq. 5.3 represents the estimated backscatter variance at height z_i, that is, $z_{i,k} = \hat{V}_\beta(z_i)$. In Eq. 5.19 above, I_k is the time interval defining the ensemble time window. For example, assuming ceilometer data with 15-s temporal resolution, a time ensemble of 8 records translates into a 2-min stationary time window (as is the case used here).

Nonlinear Least Squares Approach (NLSQ). - Alternative to the EKF, a non-adaptive NLSQ solution is also considered *Moré* [1977]. In the non-adaptive approach, the atmospheric state-vector, $\mathbf{x}_k$, is estimated at each time t_k by using only the present-time measurement, $\mathbf{z}_k$, therefore, disregarding past information. For each lidar measurement, $\mathbf{z}_k$, at time, t_k, the NLSQ solution for the model parameters is found by minimizing the quadratic norm of the error function between the observation vector, $\mathbf{z}_k$, and the model output, $\hat{\mathbf{z}}_k = h\left(\hat{\mathbf{x}}_k^{LSQ}\right)$,

$$\epsilon\left(\mathbf{x}_\mathbf{k}^\mathbf{LSQ}\right) = \mathbf{z}_k - h\left(\hat{\mathbf{x}}_k^{LSQ}\right), \tag{5.20}$$

with respect to the state vector, $\mathbf{x}_k$. That is,

$$\min\left\{\left\|\epsilon\left(\mathbf{x}_k^{LSQ}\right)\right\|^2\right\}\Bigg|_{\mathbf{x}_k=\left[z_{SBL,k}, b_k, B_k, d_k\right]} . \tag{5.21}$$

5.2.2 Coarse SBLH estimation from MWR data

In order to assimilate the thermodynamic information about SBL into the EKF formulation (Sect. 5.2.1), potential temperature retrieved from the brightness temperature measured by the MWR is used for coarse SBLH estimates. Under stable conditions, the potential temperature increases until at a height where neutral conditions are met with a constant potential temperature. The transition from the SBL to the RL is typically rather smooth and thus a clear boundary between the two regions is challenging to define. Here, it is pertinent to mention that the top of the SBL is slightly higher than the surface-based temperature inversion which becomes evident in a potential temperature profile as the region where its slope is almost zero. The SBLH is therefore defined as the height where the temperature lapse-rate is adiabatic signifying neutral condition ($\frac{\partial \bar{\theta}}{\partial z} = 0$, see inset in Fig. 4.10) *Stull* [1988]; *Bradley et al.* [1993]; *Collaud Coen et al.* [2014].

The uncertainty associated to the MWR-derived SBLH estimate results from (i) the measurement uncertainty of the brightness-temperature and (ii) the ill-posed retrieval problem. Therefore typical instrument uncertainty is included in the development of the retrieval algorithm that is used to convert brightness temperatures into temperature profiles. Here a statistical retrieval algorithm trained on a long-term data set of representative atmospheric profiles following the procedure outlined by *Crewell and Löhnert* [2007] and *Löhnert and Maier* [2012] is employed. By testing the performance of the algorithm on a synthetic test data set the altitude dependent uncertainty $\epsilon(z)$ can be derived which varies between 0.44 K on the ground and 1.20 K at 2 km. The increase in $\epsilon(z)$ with height is a consequence of the low degrees of freedom in the measurement data *Löhnert and Maier* [2012]) and reflects that the true vertical resolution of the retrieved potential temperature profiles is coarser than the discretization grid selected -a subjective choice from the user's side.

To estimate the SBLH uncertainty, $\Delta z_{MWR,meas}$, associated to the retrieved potential-temperature profile, $\theta_{MWR}(z)$ (Fig. 4.10), we apply the SBLH-model-fitting procedure described above, not only on $\theta_{MWR}(z)$ but also to the upper and lower error-bound profile for the potential temperature $\theta_{MWR}(z) \pm \epsilon(z)$, in order to estimate the impact on Fig. 5.4a).

The discretization grid of Tab. 5.1, which has been used to retrieve the temperature data for this work, follows this resolution-decreasing behaviour with height and it is, therefore, proportional to the real resolution of the data albeit the true exact values are not known. Here, for simplicity, $\Delta z_{MWR,res}$, has roughly been approximated by the discretization step of Tab. 5.1 at the estimated SBLH.

After the perturbational procedure and taking into account the uncertainty due to the low vertical resolution, the upper and lower bounds of the estimated SBLH can be written as

$$\hat{h}^{u,l}_{MWR} = \hat{h}^{fit}_{MWR} \pm \Delta z_{MWR}, \tag{5.22}$$

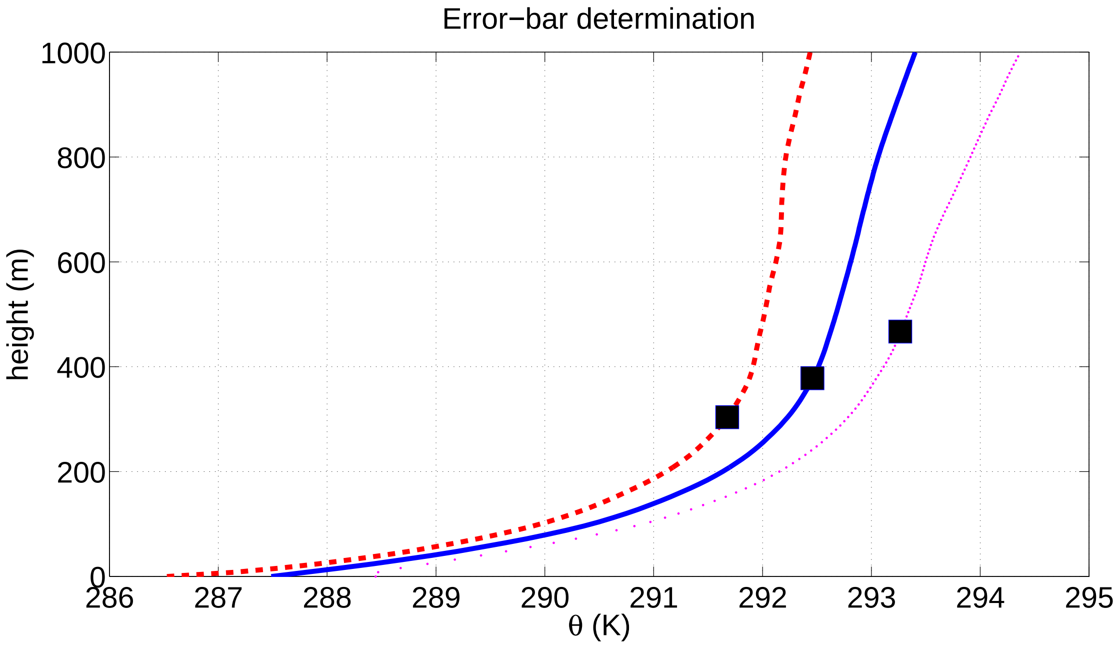

(a)

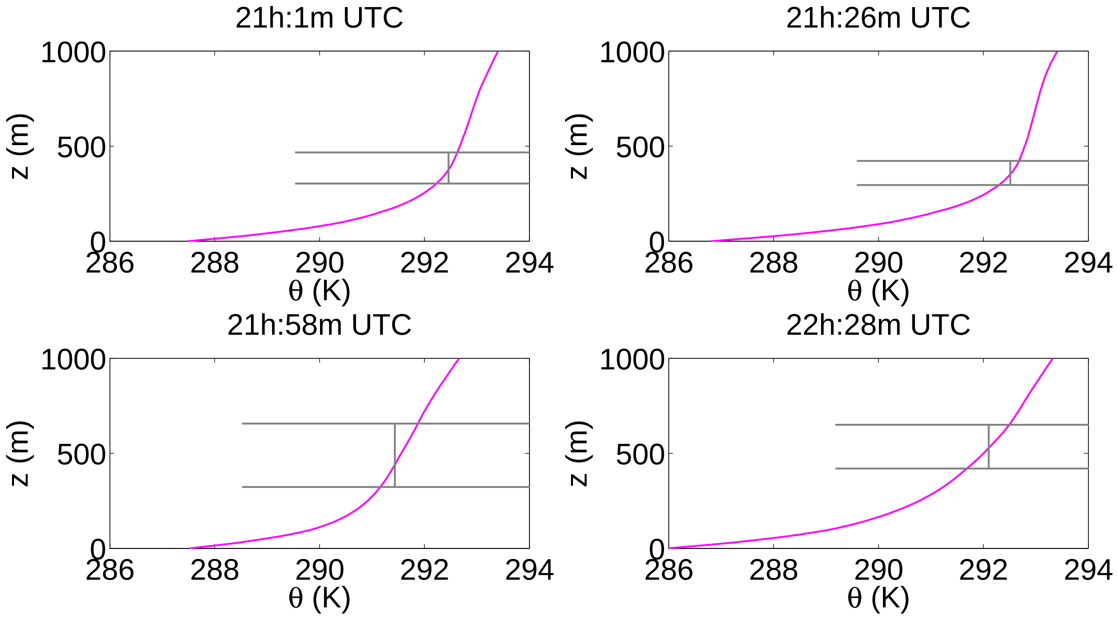

(b)

Figure 5.4: MWR signal-processing. (a) Potential-temperature perturbed-error profiles, $\theta_{MWR}(z) + \epsilon(z)$ (upper error bound, dashed red), $\theta_{MWR}(z)$ (nominal profile, solid blue here and blue crosses in Fig. 4.10), and $\theta_{MWR}(z) - \epsilon(z)$ (lower error bound, dotted red), used to estimate the errorbars associated to the MWR-retrieved potential temperature profile, $\theta_{MWR}(z)$. (b) Time-snapshots of MWR-retrieved potential temperature profiles with uncertainty due to measurements errors, (Eq. 5.22) at four time-instants from 24.04.2013, 21:00-22:30:00 UTC.

Table 5.1: Discretization of vertical temperature retrieval grid upto 1 [km].

height [m]	discretization step [m]
$0 \leq z \leq 250$	50
$250 < z \leq 700$	75
$700 < z \leq 1000$	100

Table 5.2: Statistics relating the thermodynamic SBLH determined from MWR-retrieved potential temperature and MVRs.

-	total count	percentage
Total 30-min bins	488	100
Only one MVR inside MWR error-bar	264	54.1
Two MVRs inside MWR error-bar	26	5.3
No MVR inside MWR error-bar	62	12.7
MVRs do not exist	136	27.9

where superscript “u” and “l” stand for “upper” and “lower” error bounds, respectively, and $|\Delta z_{MWR}| = |\Delta z_{MWR,res}| + |\Delta z_{MWR,meas}|$ is the estimated error including the height discretization uncertainty.

Fig. 5.4b shows four potential temperature profiles with a time-spacing of 30-min for the time interval 21:00-22:30 UTC from real measurements. For each profile the error-bar is based on the $\Delta z_{MWR,meas}$ meaning the actual error-bars will be even bigger when $\Delta z_{MWR,res}$ is taken into account for each profile. The error-bars thus define the EKF fitting ranges in the form of coarse SBLH estimates.

5.2.3 SBLH estimation from synergetic lidar-MWR data

In order to study how the SBLH height range given by the MWR-retrieved potential temperature is related to MVRs within the variance profile of the lidar backcatter data a statistical assessment was performed (Tab. 5.2). Over the study period (15.04.2013-14.05.2013) 488 30-min averaged variance profiles with corresponding MWR observations exist during nighttime, i.e. between 20:00 and 06:00. By counting the number of MVRs within the uncertainty range defined by the MWR error-bar, $\Delta z_{MWR}(z)$, it is evidenced that in almost 54% of cases a single MVR falls within the MWR error bar. For 26% of cases two MVRs lie within the MWR error-bar. No MVR was present inside the MWR error-bar for about 12% and MVRs did not exist for about 28% of cases.

When a single MVR falls within the MWR error-bar, which is the case for 54% of cases, it becomes straightforward to determine a fine estimate of the SBLH without the need to perform further processing. However, the situation gets complicated when more than one MVRs lie within the MWR error-bar or no MVR lies in the MWR error-bar or MVRs do not exist at all. In such cases, previous time estimates of SBLH can be utilized to come-up with an SBLH estimate for the present time. The Kalman filter provides a convenient framework for such kind of estimation problems where already small fluctuations (the MVRs) must adaptively be estimated and time track under random environments (i.e., the vertical profile of the variance evolving with time as a random process) and where information from previous time records must be assimilated. In the following a formulation, to determine the EKF fitting ranges, for the synergy between the MWR coarse estimate of the SBLH and the width of MVR from the previous time instant is presented.

At each time instant, t_k, estimation range boundaries $z_{1,k}$, $z^{'}_{1,k}$, $z^{'}_{2,k}$ and $z_{2,k}$ (Sect. 5.2.1 and Fig. 4.2) are determined by using a combination of the MWR SBLH estimates as well as the shape of the minimum-variance region from the previous time step, t_{k-1}. The following adaptive search boundaries are proposed

$$\begin{cases} z_{1,k} = \hat{h}^{l}_{MWR,k} \\ z^{'}_{1,k} = \hat{z}_{SBL,k-1} - \Delta h^{l}_{k} \\ z^{'}_{2,k} = \hat{z}_{SBL,k-1} + \Delta h^{u}_{k} \\ z_{2,k} = \hat{h}^{u}_{MWR,k}. \end{cases} \tag{5.23}$$

In Eq. 5.23 the MWR coarse SBLH search interval (refer to Fig. 4.2) is defined as

$$I_{MWR,k} = \left[\hat{h}^{l}_{MWR,k}, \hat{h}^{u}_{MWR,k}\right], \tag{5.24}$$

and z_{SBL} is the *fine* SBLH estimated from the EKF/NLSQ, and hence, the solution of the estimation problem.

Besides, the time-resolution of the MWR is lower than that of the ceilometer (a factor of 10 in this case), which means that $I_{MWR,k}$ changes every 10 ceilometer time records. Therefore, to match the time-stamps and to obtain a one-to-one correspondance, $I_{MWR,k}$ are interpolated according to the ceilometer time-stamps. In Eq. 5.23 the MVR-search range, $\left[z^{'}_{1,k}, z^{'}_{2,k}\right]$, is estimated from the SBLH estimate at previous-step plus/minus an incremental height $\Delta h^{u}_{k}/\Delta h^{l}_{k}$, respectively, which define the upper ("u") and lower ("l") MVR search bounds. In order to comply with the constitutive relation, $z^{'}_{1} > z_1$ and $z_2 > z^{'}_{2}$ depicted in Fig. 4.2, the upper and lower search bounds $\left[z^{'}_{1,k}, z^{'}_{2,k}\right]$ are computed at the 1σ width of the MVR (parameter b in Eq. 4.1) and constrained by the maximum allowable upper/lower heights $b^{l/u}_{max}$ (consequence of the geometry of Fig. 4.2). Formally,

$$\begin{aligned} \Delta h^{l}_{k} &= \max\left(b_{k-1}, b^{l}_{max}\right), \\ \Delta h^{u}_{k} &= \max\left(b_{k-1}, b^{u}_{max}\right), \end{aligned} \tag{5.25}$$

where

$$\begin{aligned} b^{l}_{max} &= \hat{z}_{SBL,k-1} - h^{l}_{MWR}, \\ b^{u}_{max} &= h^{u}_{MWR} - \hat{z}_{SBL,k-1}. \end{aligned} \tag{5.26}$$

In Eq. 5.26 above $b^{l/u}_{max}$ define the maximum distance (i.e., height in Fig. 4.2) from the estimated SBLH, $\hat{z}_{SBL}$, to the lower search bound, h^{l}_{MWR}, and the maximum distance from the upper search bound, h^{u}_{MWR}, to the estimated SBLH, $\hat{z}_{SBL}$. A pictorial representation of Eq. 5.25 and Eq. 5.26 variables is given in Fig. 4.2.

The recursive scheme of Eq. 5.23 thus allows to conveniently merge thermodynamic information about the SBL from the MWR-derived potential temperature with information about aerosol stratification provided by the lidar. Thus, whereas the MWR plays two important roles: 1) providing the correct aerosol layer attribution, and 2) defining coarse estimation search ranges ($z_{1,k}$ and $z_{2,k}$), the lidar provides a highly-resolved estimate of the SBLH corresponding to the center of the aerosol layer identified by the thermodynamic stability information from the MWR.

5.2.4 Results and discussions

Measurements from CT25K ceilometer and HATPRO MWR are used to estimate the SBLH under different atmospheric scenarios. First, the algorithm is applied to night-time data from 24.04.2013 (Fig. 5.1), i.e. a clear-sky day with classical boundary layer. Second, the performance is evaluated for a two hour case study from 29.04.2013 with a weakly stable nocturnal boundary layer and low aerosol amount. SBLH estimates from the EKF and NLSQ estimates are compared to assess their different performance.

24.04.2013 - At midnight the temperature profile (Fig. 5.1) reveals stable conditions. Together with the high aerosol backscatter signal in the SBL that reaches heights up to 600 [m] (Fig. 5.5a) this indicates a well developed stable boundary layer between mid-night and sunrise (around 4:30 UTC). Both EKF and NLSQ estimate SBLH between 400 and 600 [m] with good agreement among each other though EKF SBLH estimates are much smoother due the assimilation of the information from past estimates.

The benefit of EKF becomes more pronounced when the period past sunset (around 19:30) is considered from 21:00-24:00 UTC. As the surface of the Earth becomes gradually cooler, convection ceases and atmospheric stability increases affecting successively higher altitudes. Initially aerosol is not accumulated in the SBL and the backscatter return from the RL is still significant when compared to SBL. This is in contrast to the previous period between midnight and early morning when aerosol had accumulated in the SLBH during the course of the night and the backscatter signal in the RL was lower. Thus, Fig. 5.5b shows that although there is a higher aerosol backscatter signal from the lower heights, a

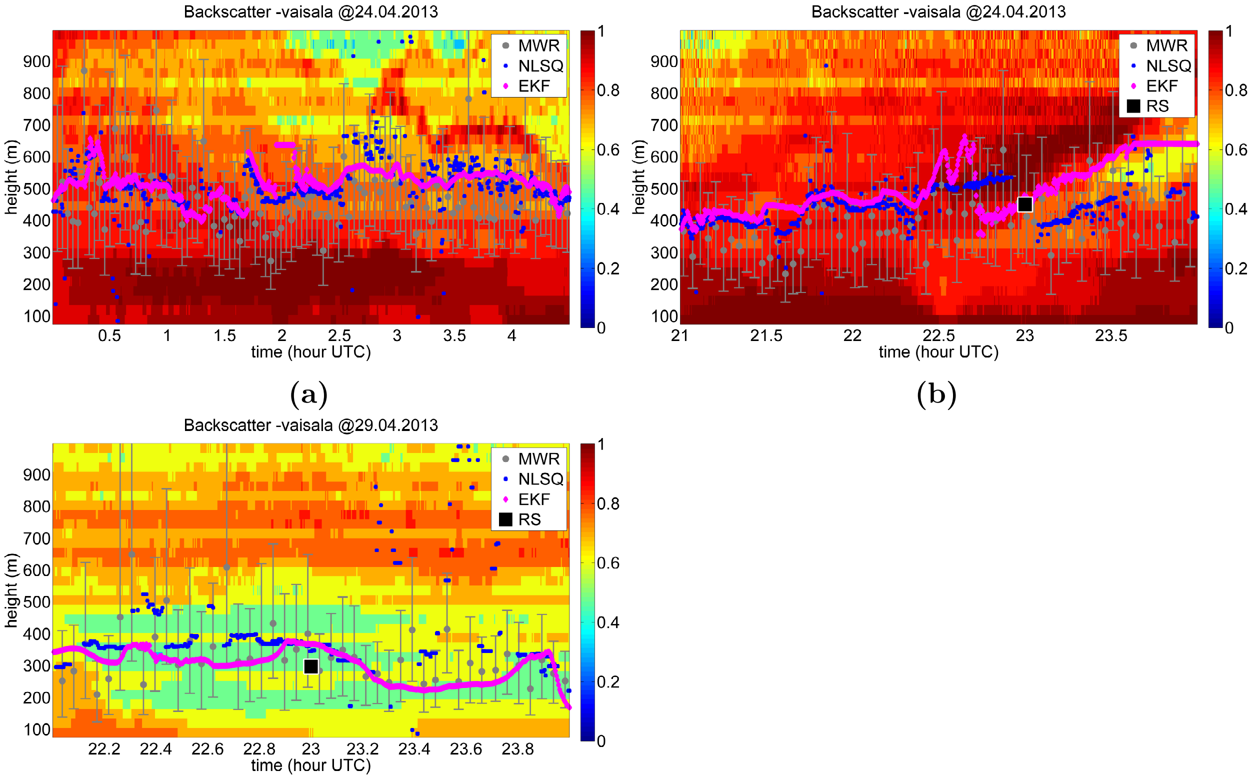

(a)

(b)

(c)

Figure 5.5: Test cases based on data from HOPE campaign at Jülich, Germany. (a) Colorplot of the ceilometer backscattered signal for 24.04.2013, 00:00-04:30 UTC measurements along with SBLH estimates from the EKF and the NLSQ approaches. (b) Colorplot of the ceilometer backscattered signal for 24.04.2013, 21:00-24:00 UTC measurements along with SBLH estimates from the EKF and the NLSQ. SBLH estimate from the radiosonde (black square) launched at 23:00 is also shown. (c) Colorplot of the ceilometer backscattered signal for 29.04.2013, 22:00-24:00 UTC measurements along with SBLH estimates from the EKF and the NLSQ. (All panels) MWR-EKF search ranges $[z_{1,k}, z_{2,k}]$ (Eq. 5.23 and Fig. 4.2) are plotted as gray vertical bars.

considerable amount of aerosols are still trapped in the RL. Fig. 5.5b also compares the SBLH estimates obtained from the synergetic lidar-MWR approach of Sect. 5.2.3 from EKF and NLSQ estimators. Comparison between EKF and NLSQ SBLH estimates shows that the NLSQ fails most of the time. This is due to the non-adaptive behaviour of the NLSQ estimator which causes that when it is confronted with different MVRs within the "coarse search" boundaries marked by the MWR, the NLSQ can not disambiguate which one to choose. In these situations, the NLSQ just provides the least-squares-error (LSQ) solution averaged over all the MVRs in the estimation range. In contrast, the EKF conveniently provides a reasonable solution averaged under a criterion of minimum MSE over time due to its assimilation of past temporal information (covariance). Furthermore, good agreement with the radiosonde at 23:00 is evident.

29.04.2013 - The period between 22:00-24:00 UTC provides a more challenging case from the signal-processing point of view in which the variance (an already small quantity as mentioned in Sect. 4.1.1) must be estimated from the backscatter returns (the signal component) in response to an atmospheric scene nearly depleted of aerosols (weakly stable nocturnal boundary layer). Thus, Fig. 5.5c shows that aerosols in the lower height, where usually a stable boundary layer is developed by this time of the day, provide much less backscatter signal as compared to higher heights belonging to the residual layer (such kind of situations usually prevail when thermal emission from the Earth surface is slow or there is a cloud cover trapping the surface heat in the atmosphere or a cleaner airmass is advected due to synoptic conditions at the location of measurements). In the case of Fig. 5.5c the spatial variance of the backscatter signal (estimated via the approximation of (Eq. 5.3) becomes a weak "tracking" indicator of the SBLH because the variance is in fact estimated from signal samples approaching zero (i.e., the backscatter returns in a SBL virtually depleted of aerosols) and the existence -and correct detection- of MVRs is inherently linked to the stratification of aerosols. Therefore, this is a "complex" estimation problem characterized with very low SNRs, where the role of the MWR becomes even more critical and where SBLH estimates largely benefit from "a priori" information coming from potential temperature data. Obviously, NLSQ estimator (non adaptive) fails almost at all the times. However, the EKF still provides reasonably good SBLH estimates thanks to the assimilation of MWR and past temporal information.

In total, 226 radiosondes were launched during the HOPE campaign. However, the majority of radiosondes (≈75%) were launched during daytime mixed-layer conditions. In reality, in most of the days, one radiosonde was launched at 23:00 UTC and during the so-called intensive observations periods (IOPs 15.04, 18.04, 20.04, 24.04, 25.04, 29.04, 02.05, 04.05, 05.05, and 18.05) several radiosondes were launched during night and early morning times, as well. Thus, along with the majority of radiosondes at 23:00 UTC, a few ones at 21:00, 03:00, 05:00, 07:00 and 09:00 UTC are also available for SBL studies. Due to synoptic conditions, such as wind shear or residual convection from the daytime, on some days (e.g., 19.04, 01.05, 16.05, 21.05) the SBL did not form at these times and hence, these cases have been excluded. As a result, only 56 radiosondes become available for such comparative study. SBLH from all these radiosonde launches, available for SBL study, was calculated and it has yielded a mean SBLH of 424 [m] with an error standard deviation of ±150 [m]. When this SBLH radiosonde-estimate is compared with the study cases presented in Fig. 5.5, it is clear that the estimated SBLH almost always falls within the radiosonde-estimated height interval (274-574 [m]), as expected.

Main limitations of the technique presented in this work encompass both instrumental and environmental limitations: (i) Concerning *instrumental limitations*, the partial overlap of the lidar (also known as laser-telescope cross-over function), which is the case for bi-axial lidar systems, distorts the attenuated backscatter profile at low heights. Therefore, the technique only works for SBL heights which are above the range of full overlap of the system. Since the CT25k is a mono-axial system with its first range gate starting at around 60 m, this instrumental limitation does not arise in this work. (ii) Concerning *environmental conditions*, it must be said that typically, the SBL height is not more than one km *Stull* [1988], which means that the technique presented here will, almost always, be of application along the first km of the vertical lidar profile. Yet, the existence of stable atmospheric conditions is always a pre-requisite since the stratification of aerosols occurs only under SBL. In fact, aerosol load will ultimately condition the quality of filter convergence since aerosols are needed as tracers of the atmospheric phenomenon under study. Though this is still a matter of research, comparatively, the EKF has successfully estimated the SBLH in the study case of Fig. 6c (low aerosol load) with a contrast backscatter level in the SBL as low as 0.3-0.6 a.u. (heights interval 274-574 m) as compared to a free-troposphere level of almost 0 a.u. at 2 km. In the study case of Fig. 6b (high aerosol load, nocturnal case) the backscatter level lies between 0.7-1.0 a.u. In terms of thermodynamic stability detected by the MWR, elevated inversions are a challenge for detection.

5.3 Conclusions

An adaptive solution based on synergetic use of data from a lidar-ceilometer and a MWR has been presented. Vertical variance of the attenuated backscatter signal from a (Vaisala CT25K) ceilometer has been used as an indicator of the aerosol stratification in the nocturnal stable boundary layer. Minimum variance regions within the vertical variance profiles have been modelled by an inverted Gaussian-like function and model parameters including the sought-after SBLH have adaptively been estimated by using an EKF. Coarse SBLH estimates from MWR-retrieved potential temperature observations have been assimilated for aerosol layer disambiguation and to incorporate information about the thermodynamic stability of atmosphere.

Physical/signal-processing steps can be summarized as follows: First, the vertical variance of the ceilometer backscatter signal is estimated by using a moving-average filter (150 m rectangular window) as de-noising step. The correct filter window length is obtained by monitoring statistical properties of residual instrumental noise. By this means, MVRs, which are indicative of the stratification of aerosol layers in the nocturnal stable boundary-layer, are evidenced in the vertical moving variance profiles of the denoised backscatter signal. The existence of MVRs and their correlation with the SBL has been further investigated by processing one month data from HOPE campaign. After screening for clouds and rain, the vertical variance calculated and averaged for 30-min in time and 200 [m] in height bins. Counting the MVRs falling inside the error-bar defined by MWR, it was observed that for about 54% of cases a single MVR and for about 5% of cases two MVRs were present inside the MWR error-bar. Whereas, no MVRs lied inside MWR error-bar for 13% of cases, the MVRs did not exist at all for about 28% of cases.

MVRs are modelled by using an inverted Gaussian-like function with the SBLH as key parameter of the state-vector model. The state vector is adaptively estimated by using an EKF whose search boundaries are defined from the MWR "coarse" SBLH estimates and the 1σ width of the time-adaptive Gaussian model.

The synergetic approach has been applied to measurements from the HOPE campaign at Jülich, Germany. Three atmospheric scenarios have been presented: 1) An early morning scenario of SBL with deep stratification of aerosols and thermodynamic stability in the atmosphere; 2) An evening case where the SBL just starts developing from the Earth surface; 3) And a complex case with shallow stratification of aerosols in the atmosphere. Results from these three cases have shown that the proposed synergetic approach performs well for the different time intervals of the day as well as under different "nocturnal" atmospheric conditions.

Future work of this prototype algorithm is to involve long-term measurement data as well as more complex atmospheric scenarios whereby the nocturnal boundary layer is intermittently turbulent. More sensitive ceilometer instruments such as the CL31 and CL51 can provide better information about the aerosols stratification and could reveal fine structures in the SBL. Moreover, better processing of the MWR data for SBLH estimates with lower uncertainty could provide better results for complex cases. The ultimate goal of this preliminary study is to develop a synergetic retrieval algorithm for full diurnal cycle of the ABLH over the course of the day.

Chapter 6

Large-eddy simulation: A perspective for understanding the atmospheric boundary layer

This short chapter presents a preliminary study on the use of Large Eddy Simulation (LES) model for understanding the Atmospheric Boundary Layer (ABL). As an example case, direct retrieval of mixing-layer height from LES-simulated brightness temperature is presented.

The contents of this Chapter are part of the results presented at MicroRad, 2016 *Saeed et al.* [2016a].

6.1 Introduction

LES provides a convenient tool to study the capabilities and the performance of algorithms without instrumental shortcomings as it provides all meteorological variables with high spatial resolution in a physically consistent manner. In order to simulate a realistic atmospheric scenario the LES model - in this case, the Dutch Atmospheric Large-Eddy Simulation (DALES) *Heus* [2010]; *Neggers et al.* [2012] - is driven by meteorological analysis from a numerical weather forecast model. DALES is based on the LES code of Nieuwstadt and Brost (1986) and has been specifically adapted to study the physics of the ABL, that includes the CBL and SBL as well as the cloudy ABL.

For this study case, DALES was initialized for 24.04.2013 at 00.00 UTC for Jülich, Germany, and run for 24 [h] with a spatial resolution of 40 [m] and outputs every 30 [min]. Since it is a clear-sky day with an idealised development of ABL, thus a convenient choice for testing ABLH estimation algorithms. Because DALES does not explicitly include aerosol, two passive tracers, Tracer-1 and Tracer-2 were introduced as proxies.

At the start of the simulation Tracer-1 is set to a concentration value of 1 [kg/kg], defined as kg of "aerosols" per kg of air, in the RL, which in this simulation case was about 1 [km] of height. Above one 1 [km], (free troposphere), Tracer-1 is initially set to zero. In the course of the simulation, tracer concentration in the FT increases due to the detrainment at the top of the boundary-layer. Tracer-2 describes the emission of aerosols at the surface that are subsequently mixed into the atmosphere due to the surface flux. The two tracers are combined (first scaling them to the same magnitude ranges and then adding) to simulate the aerosols behavior within the boundary-layer over the course of a day. In this way the aerosol mixing ratio, m_{aer} [kg/kg], in the atmosphere is given at each altitude and time step.

The LES-derived total-backscatter coefficient, β, is computed by using the approximation,

$$\beta = a \cdot m_{aer} \cdot f(RH), \tag{6.1}$$

where "a" is a scaling factor to match the magnitude of the LES-simulated total backscatter corresponding to the lidar measurement and f(RH) is a factor depending upon the relative humidity, RH, with the relation

$$f = \left[1 - \frac{RH}{100}\right]^{-0.2}. \tag{6.2}$$

Fig. 6.1 compares the measured backscatter (Fig. 6.1a) and the measured potential temperature (Fig. 6.1c) corresponding to the development of the ABL on 24.04.2013 with the simulated backscatter (Fig. 6.1b) and the potential temperature (Fig. 6.1d) time-height structure over the full diurnal course. Because this day was characterized by weak synoptic forcing and nearly no clouds, ABL development is close to the idealized cases described in Chap. 1, Sect. 1.2. Since the LES simulation was started at midnight and the stable boundary layer prevailed until about an hour past sunrise, the aerosol mixing process did not start until about 06:00 UTC when the convection became significant and the convective ML developed. This can well be seen by the neutral conditions, i.e., vertically constant potential temperature. Around sunset (18:30 UTC) mixing recedes and thus aerosol stratification occurs. The extent of aerosol stratification in the SBL is directly linked to the amount of thermal stability in the boundary-layer. The observed backscatter and potential temperature agree well with the LES, nicely showing the same morphological development of the ABLH.

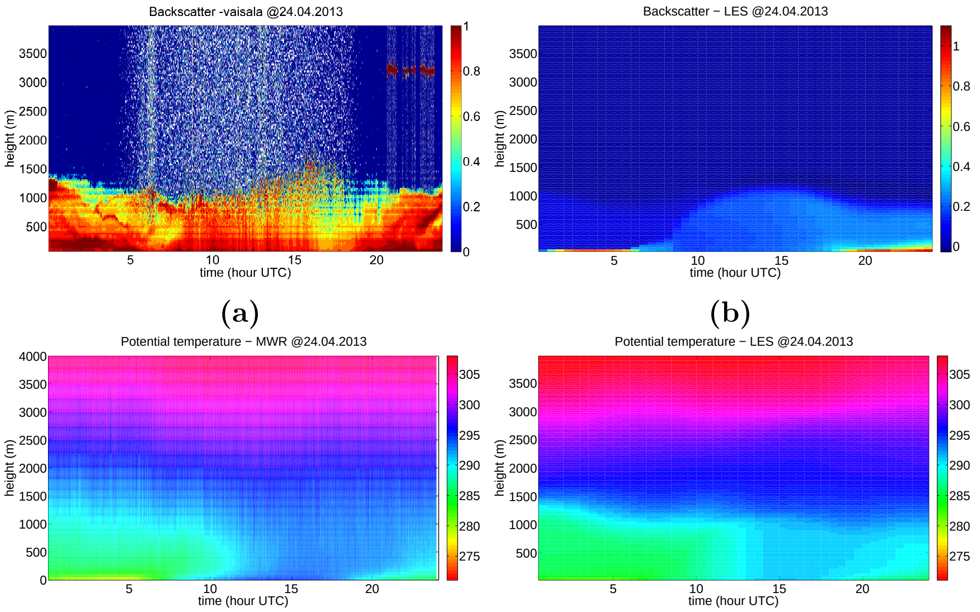

(a) (b)

(c) (d)

Figure 6.1: Comparison between measured and LES-simulated aerosol backscatter and potential temperature data from 24.04.2013, Jülich, Germany. (a) Colorplot of the backscatter profiles measured by the Vaisala CT25k ceilometer. (b) Colorplot of the LES-simulated atmospheric backscatter. (c) Colorplot from the MWR-retrieved potential temperature data. (d) Colorplot showing LES-simulated potential temperature.

6.2 Direct retrieval of the MLH from simulated brightness temperature

In the following, a method for direct retrieval of the MLH from brightness temperature measurements, and without the need to perform a temperature retrieval first, is presented.

As a proof of concept, the retrieved MLH is compared with the MLH obtained from the inverted potential temperature by using the "truth" brightness temperatures, hence allowing to study the impact of retrieval errors on the MLH estimates. Towards this end, the algorithm compares "truth" brightness temperatures to algorithm-generated ones by using an OEM.

The processing steps of Fig. 6.2 are considered:

"Truth" brightness temperatures, which emulate the real atmosphere, are generated by using the DALES model as a test-bed. LES-generated vertical profiles of the atmospheric temperature, pressure, and water-vapor are first input to a forward model, thus, simulating brightness temperatures, $T_b^{LES}(\nu, \Phi)$, where ν is the frequency of measurement and Φ is the elevation angle.

Algorithm-generated brightness temperatures, T_b^{PARAM}, are obtained from a "state vector", x (i.e., the unknown to be solved) parametrizing model temperature along with known pressure and humidity profiles followed by a forward model. The state-vector $x = [z_{MLH}, T_0, \Delta z_{EZ}]$

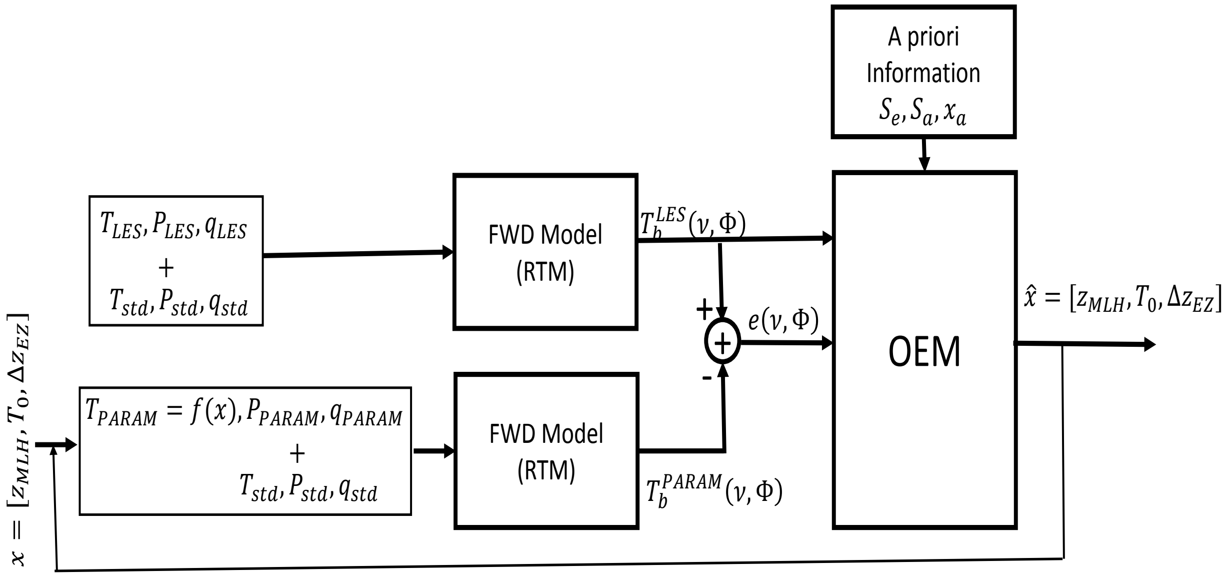

Figure 6.2: Block diagram of the proposed direct MLH-retrieval scheme. Starting from left-hand side, T stands for temperature, P for pressure, q for absolute humidity. Subindex "LES" stands for Large Eddy Simulated variable, "PARAM" stands for parametrized variable, and "std" stands for standard atmosphere. $T_b(\nu, \Phi)$ is the brightness temperature at frequency ν and elevation angle Φ. $e(\nu, \Phi)$ is the brightness-temperature error. In the block "A priori", S_e stands for measurement error covariance matrix, S_a stands for state-vector covariance matrix, and x_a stands for the initial guess on the state-vector. Finally, $x = [z_{MLH}, T_0, \Delta z_{EZ}]$ is the state-vector with z_{MLH} the MLH, T_0 the surface temperature, and Δz_{EZ} the EZ width.

is parametrized by three components: z_{MLH} is the MLH, T_0 is the surface temperature, and Δz_{EZ} is EZ width. The key parameter of the "state vector" is the MLH. This parametrization of the input temperature profile effectively allows to reduce the DoF of the retrieval problem. The algorithm converges under an OEM criterion that provides the maximum likely-hood estimate of MLH using Bayesian approach.

Since the MLH is the key component of the state-vector being solved, the proposed algorithm does not need to carry out the classic two-step procedure in which: (i) physical temperature profiles are inverted from brightness temperatures and, (ii) the MLH is estimated from the retrieved temperature profiles (parcel method). As a result, the proposed algorithm is free from brightness-to-physical temperature retrieval errors associated to classic MLH-estimation methods relying on step (i). The proposed approach is expected to provide MLH estimates with better accuracy and low uncertainty.

6.2.1 Problem formulation

In Chap. 3, Sect. 3.3.1, it was discussed that there are two main sources of uncertainty on MLH estimates from MWR-retrieved potential temperature: (i) the instrumental uncertainty due to the *brightness-temperature measurements*, Δz_{T_b}, and (ii) the uncertainty due to the *coarse vertical resolution* of the retrieved potential temperature profiles, Δz_{res}.

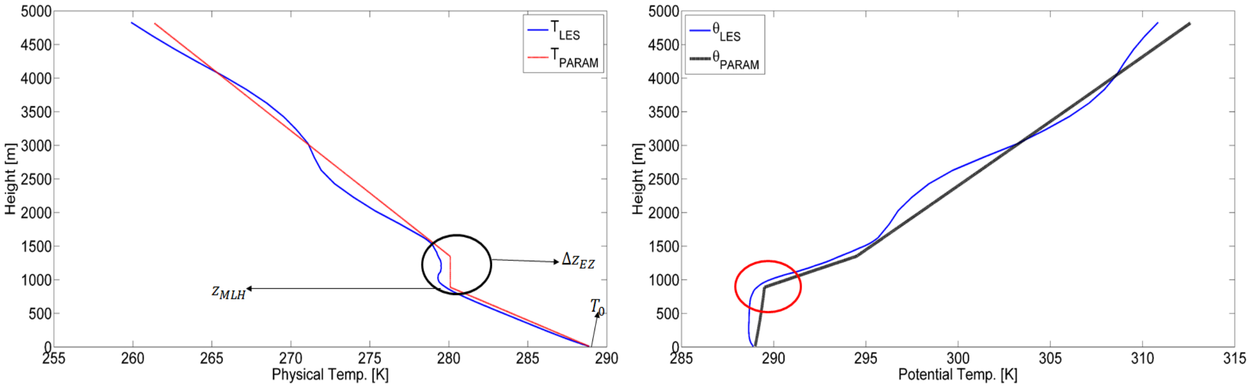

(a) **(b)**

Figure 6.3: Comparison between LES-simulated and parametrized temperature profiles, 10:50 UTC, 24.04.2013, Jülich, Germany. (a) Temperature profiles. (b) Potential temperature profiles.

There is no way to avoid (i). Therefore, in order to test our method without the influence of instrumental measurement errors, LES-simulated data is used. By generating simulated profiles of the atmospheric variables of interest, namely, temperature, pressure, and humidity. DALES provides a virtual laboratory to test algorithms without the shortcomings of instruments. Moreover, the impact of retrieval errors on the estimated MLH can also be studied, since the input reference is available.

In order to tackle (ii), a scheme for direct retrieval of MLH without the need to perform temperature retrieval first is proposed.

Parametrization of the temperature profile. - In order to reduce the DoF of the MLH retrieval problem, the atmospheric temperature profile is parametrized in terms of the MLH, z_{MLH}, the surface temperature at ground level, T_0, and the width of the EZ at the top of the ML, Δz_{EZ}, as follows

$$T_{PARAM}(z) = \begin{cases} T_0 - a_{ML} \cdot z, & z \leq z_{MLH} \\ T_{MLH}, & z_{MLH} \leq z \leq (z_{MLH} + \Delta z_{EZ}) \\ T_{MLH} - a_{FT} \cdot z, & (z_{MLH} + \Delta z_{EZ}) \leq z \leq z_{max}, \end{cases} \tag{6.3}$$

where a_{ML} is the temperature lapse-rate in the ML, T_{MLH} is the temperature at the top of the ML, a_{FT} is the FT temperature gradient, and z_{max} is the maximum height for T_{PARAM}.

Fig. 6.3 shows a comparison between the LES-simulated and the parametrized physical and potential temperature profiles. As it can be noticed in Fig. 6.3a the physical temperature profile has been parametrized by the three parameters which include the mixing-layer height, z_{MLH}, the surface temperature, T_0, and the width of EZ, Δz_{EZ}. The parametrized temperature profile fits well with the LES-simulated temperature profile. Fig. 6.3b shows the LES-simulated and parametrized potential temperature profiles corresponding to the physical temperature profile of Fig. 6.3a.

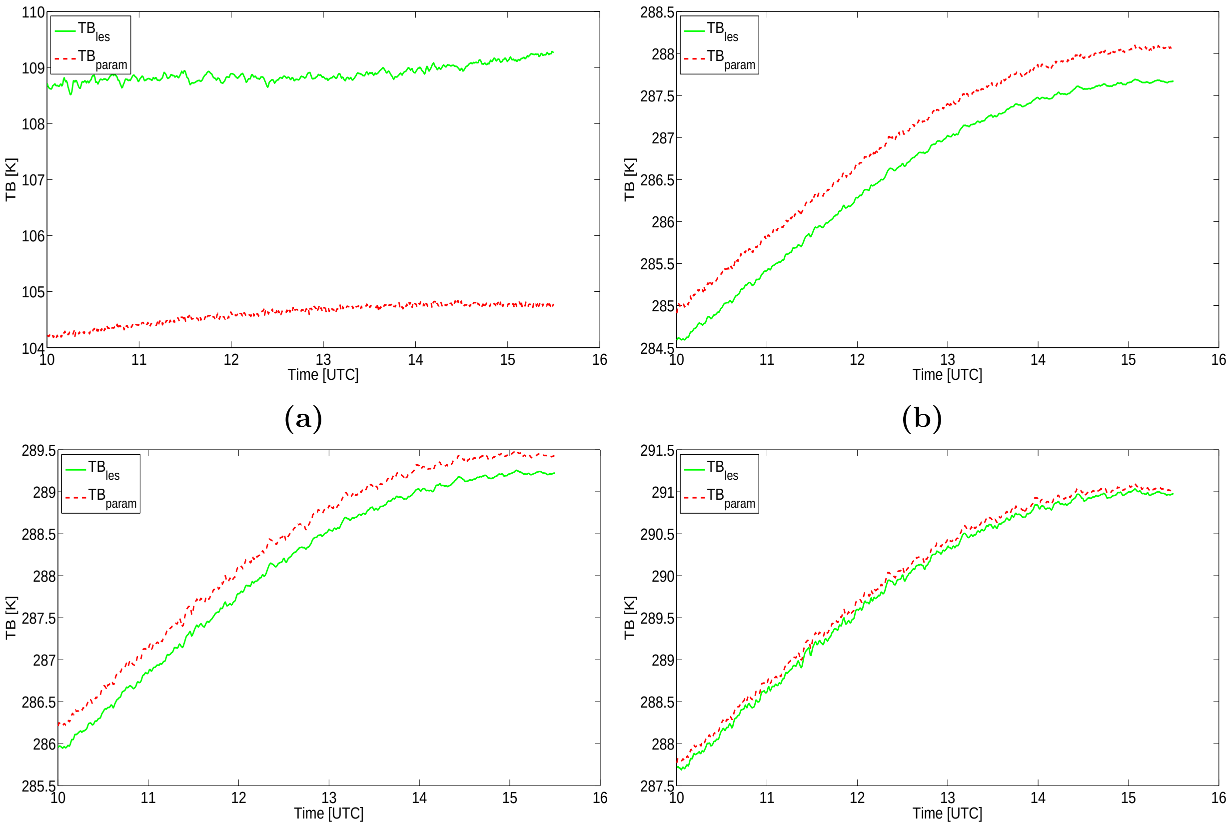

(a) **(b)** **(c)** **(d)**

Figure 6.4: Comparison between LES-simulated and parametrized brightness temperature measurements at different frequencies and elevations, 10:50 UTC, 24.04.2013, Jülich, Germany. (a) Frequency: 51.26 [GHz], elevation: 90 [deg]. (b) Frequency: 58 [GHz], elevation: 90 [deg]. (c) Frequency: 54.94 [GHz], elevation: 10.2 [deg]. (d) Frequency: 58 [GHz], elevation: 5.4 [deg].

Optimal estimation method for state-vector estimation: - The OEM used is a Bayesian solution to the parameter estimation problem given a set of noisy measurements, where the noise is assumed to be Gaussian *Rodger* [2000]. The iterative solution for the OEM is given by

$$x_{k+1} = x_k + \left(K_k^T S_e^{-1} K_k\right)^{-1} \left[K_k^T S_e^{-1} (y - y_k) + S_a^{-1} (x_a - x_k)\right], \tag{6.4}$$

where $x_k = [z_{MLH}, T_0, \Delta z_{EZ}]$ is the state-vector, y denotes brightness measurements, x_a is the *a priori* state-vector, S_e is the measurement covariance matrix, S_a is the state-vector covariance matrix, K_k is the Jacobean of measurements with respect to the state-vector, y_k and x_k are the past brightness measurements and state-vector, and k is the time index.

6.2.2 Results and discussion

Comparison of actual and estimated measurements. - The OEM provides optimal estimates of the state-vector parameters at each time instant. As a first test of the performance of the proposed approach, brightness temperatures obtained by the LES-simulated atmosphere,

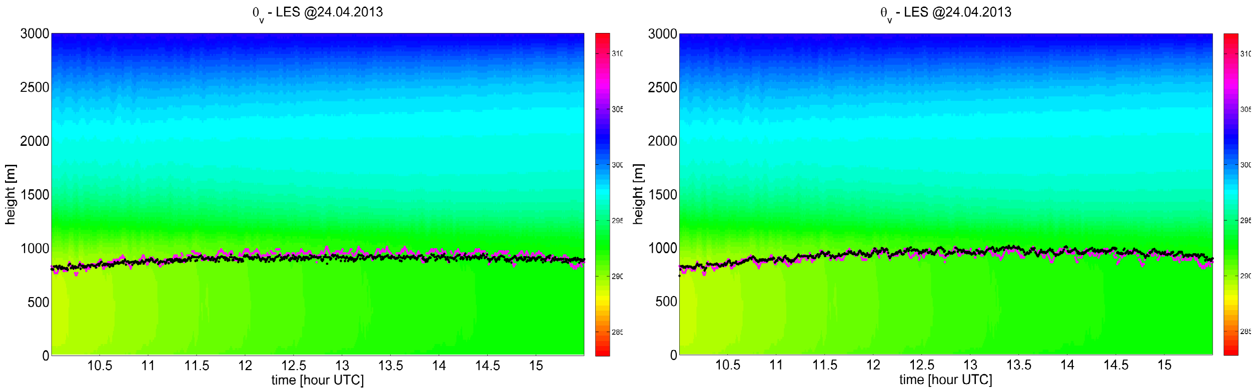

(a) (b)

Figure 6.5: MLH from the parcel method (magenta trace) and the direct-retrieval method (black trace) by using: (a) MWR zenith measurements, and (b) MWR elevation measurements.

T_b^{LES}, and brightness temperatures obtained by the estimated state-vector, T_b^{PARAM}, are compared at the different frequencies and elevation angles of the MWR channels (Fig. 6.4):

- ν = **51.26 [GHz],** Φ = **90 [deg]**: This is the most transparent channel and hence, extends high up in the atmosphere. As a result, the effect of parametric approximation becomes significant enough resulting in more than 4 [K] of difference, $e(\nu, \Phi) \geq 4$[K] (Fig. 6.4a).

- ν = **58 [GHz],** Φ = **90 [deg]**: As the measurement frequency becomes closer to the center of the O_2 band (60 [GHz]), the difference between LES-based brightness temperature measurements and parametric brightness temperature measurements becomes lower (Fig. 6.4b).

- ν = **54.94 [GHz],** Φ = **10.2 [deg]**: The difference between LES-brightness temperatures and the parametric model atmosphere decreases with lower elevation angles as the extent of atmosphere contributing to the brightness measurements comes from lower heights (Fig. 6.4c).

- ν = **54.94 [GHz],** Φ = **5.4 [deg]**: Finally, the most opaque channel with the highest frequency and the lowest elevation angle results in the minimum difference between LES and parametric-based brightness temperature measurements (Fig. 6.4d).

Comparison between reference (LES) and estimated MLH estimates. - MLH estimates obtained from the parcel method and the direct-retrieval method are presented and compared using zenith-only and elevation (including zenith) measurements (Fig. 6.5). Fig. 6.5a shows qualitative comparison between the MLH estimates obtained from the LES-simulated temperature via the parcel method and the direct-retrieval method using zenith-only MWR measurements. Fig. 6.5b shows the same as Fig. 6.5a but with measurement from elevation angles included. A good agreement is evident. In order to get more in-depth analysis and

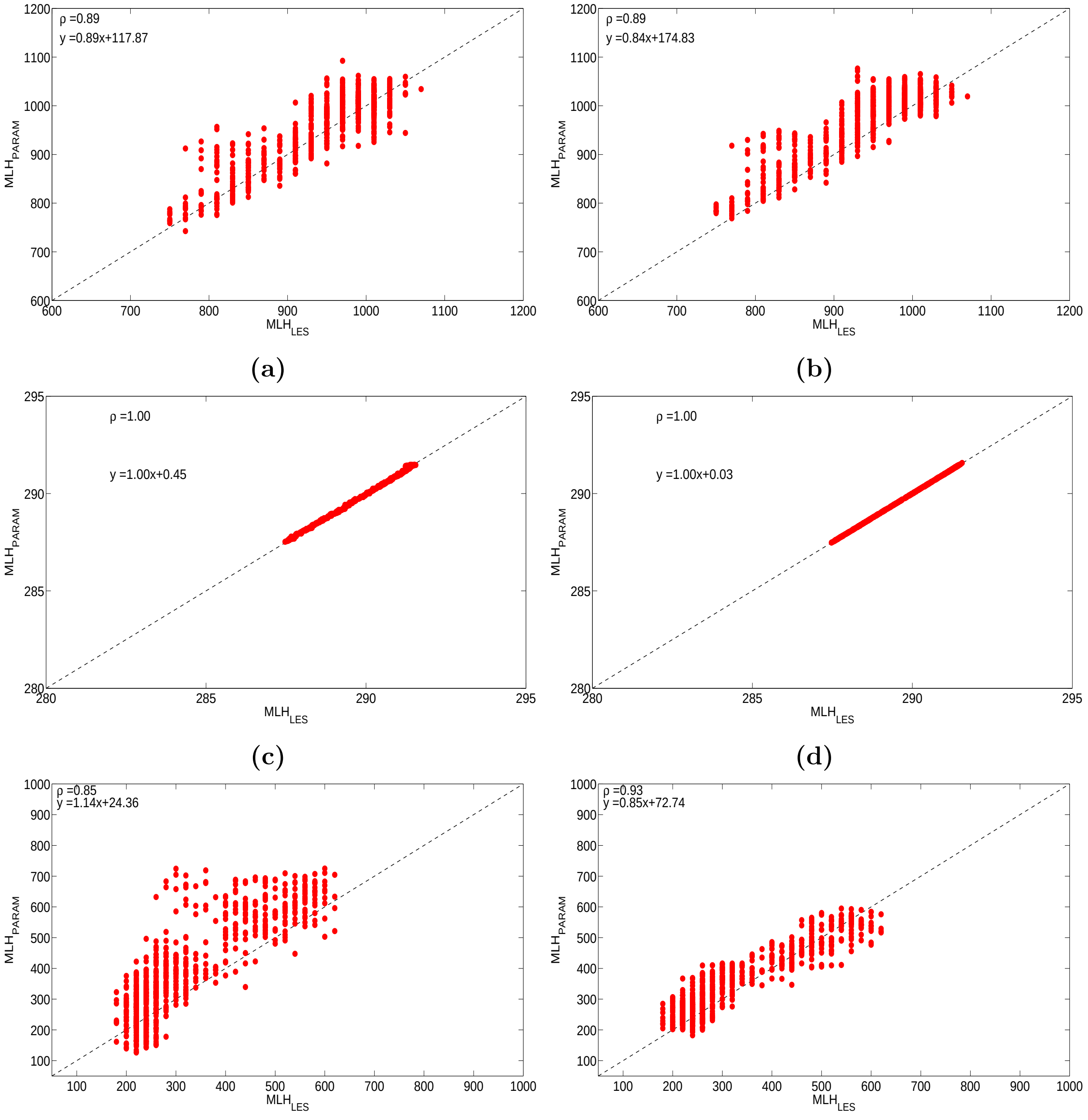

(a) (b)

(c) (d)

(e) (f)

Figure 6.6: Scatter plots of MLH (z_{MLH}), surface temperature (T_0), and width of entrainment zone (Δz_{EZ}). (a) z_{MLH} using zenith measurements only. (b) z_{MLH} using 27 elevation measurements (7 zenith, and 20 elevation). (c) T_0 using zenith measurements only. (d) T_0 using elevation measurements. (e) Δz_{EZ} using zenith measurements only. (f) Δz_{EZ} using elevation measurements.

quantitative results, Fig. 6.6 shows scatter plots of MLH (Figs. 6.6a, 6.6b), surface temperature (Figs. 6.6c, 6.6d), and width of the EZ (Figs. 6.6e, 6.6f) estimated from LES-simulated temperature data as well as from the direct-retrieval method.

Impact of retrieval temperature on MLH estimates. - Finally, in order to study the impact of temperature-retrieval errors on MLH estimates, LES-simulated profiles of physical and potential temperature (T_{LES} and θ_{LES}, respectively) are compared against the retrieved-temperature and retrieved-potential temperature profiles obtained from the simulated measurements.

Fig. 6.7a shows that the retrieved temperature profile ($T_{RET,LES}$ and $\theta_{RET,LES}$, respectively) is a smoothed version of the real atmosphere, consequently, missing the correct inversion-related information on temperature inversion. This is due to instrumental limitations as well as physical ones coming from the low DoF in the measurements. The impact of this smoothing effect is clearly seen in terms of under-estimation of MLH in Fig. 6.7b.

6.3 Conclusions

A method for MLH retrieval directly from MWR brightness-temperature measurements has been presented, thus alleviating the need for retrieval of temperature profiles as an intermediate step. The physical temperature profile has been parametrized in terms of three state-vector parameters including the MLH, and thus reducing the DoF of the problem. The absence of temperature retrieval errors has resulted in low-uncertainties on the estimated MLH. Information from elevation measurements has improved the MLH retrieval.

In future, validation on long-term simulated and measurements data under different atmospheric conditions from HOPE campaign will be carried out. Use of *a priori* information from other instruments such as the backscatter and the Doppler lidar is expected to improve the results. The method is well suited for operational retrieval of the MLH.

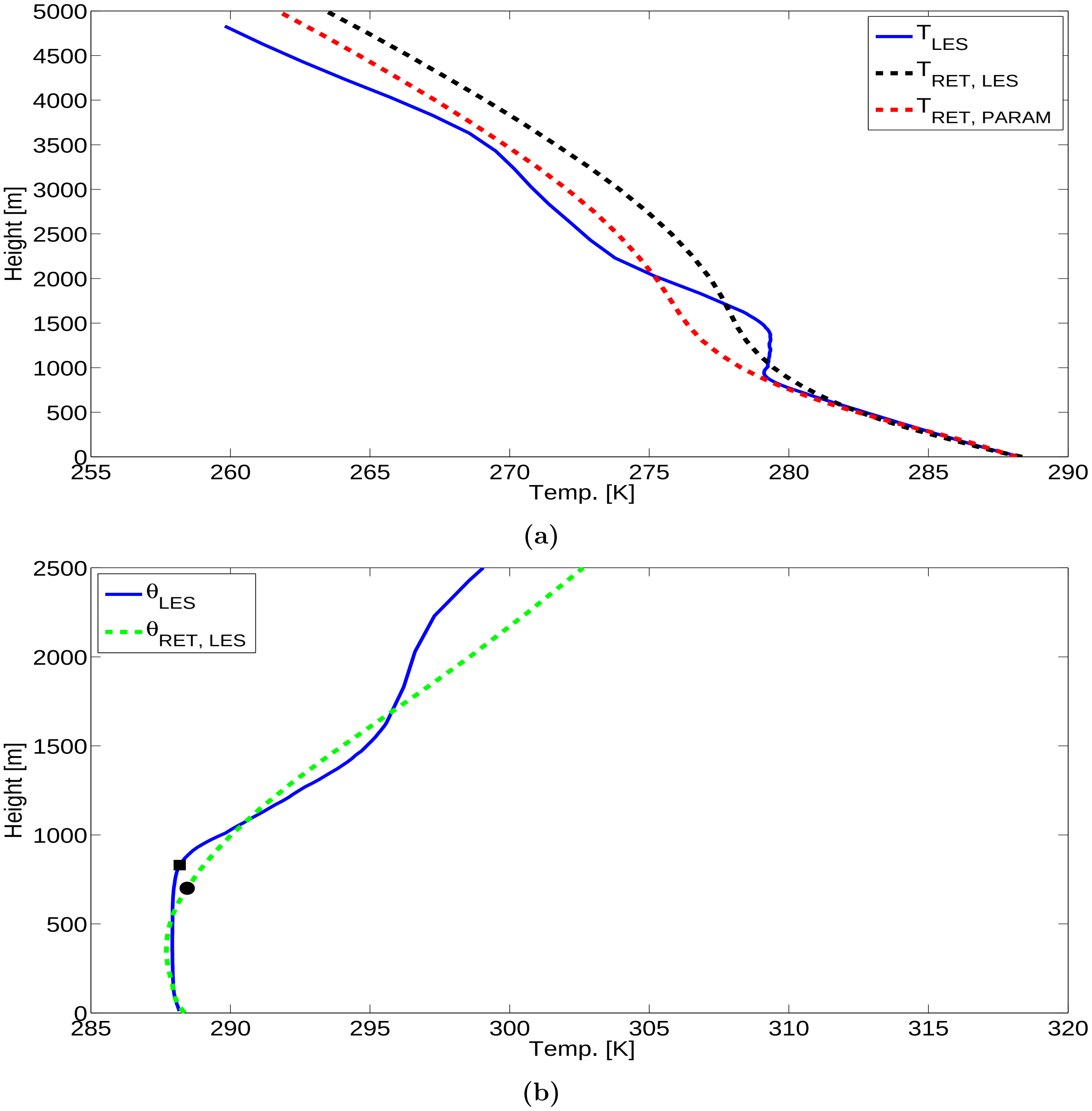

Figure 6.7: Comparison between LES-simulated, LES-retrieved, and parametric-retrieved profiles of physical temperature and potential temperature. (a) Physical-temperature profiles. T_{LES} is the LES "truth" temperature, $T_{RET,LES}$ is the LES-retrieved temperature. $T_{RET,PARAMm}$ is the parametrized-retrieved temperature. (b) θ_{LES} is the LES "truth" potential temperature. $\theta_{RET,LES}$ is the LES-retrieved potential temperature. The solid black square indicates the "true" MLH from LES. The solid black circle indicates the LES-retrieved MLH.

Chapter 7

Conclusions

This chapter summarizes concluding remarks and future lines of work.

7.1 Conclusions

On development of a synergetic method for MLH estimation from combined lidar and MWR measurements (obj. 1). - Two commonly used methods for MLH estimation, the EKF from backscatter lidar signals and the parcel method from MWR-retrieved potential-temperature measurements, have been analysed in terms of their capabilities and uncertainties.

In the lidar case, since the EKF assimilates measurement errors via the measurement covariance matrix, it already provides *a posteriori* errors on the estimated state-vector and hence, the uncertainty on the MLH being estimated.

In the MWR case, the uncertainty on the MLH due to measurement and retrieval errors has been analysed by using the error superposition principle. Uncertainty due to *measurement errors* has been estimated by applying the error-propagation method and simulated measurement values from the literature. *Retrieval errors* have been approximated by the vertical resolution of the temperature profile along the height grid.

MLH from the two methods (lidar and MWR one) along with their uncertainties have been compared against the reference MLH estimated from RSs and Doppler wind lidar. On one hand, it has been shown that, though the EKF performes well in well-mixed atmospheric conditions, it lacks physical consistency under certain atmospheric conditions especially associated to the morning and evening transition of the boundary-layer. On the other hand, the MWR provides physically consistent estimates of the MLH albeit with much higher uncertainty. Therefore, it has been concluded that a synergy of the methods can provide highly-resolved and physically consistent estimates of the MLH.

In this context, a synergetic MLH method has been presented. It works by fitting an erf-like transition model function to the ML-to-FT section of the range-corrected backscatter lidar signal. The start and end ranges of this “search” section where the EKF fits the erf-model function are defined by the MWR estimates of MLH along with associated uncertainties. This new approach, which exploits the synergy between the two instruments, has enabled to detect and track the MLH without loss of the original vertical and temporal resolutions. Test cases combining data from a co-located ceilometer and a MWR have been presented. Doppler wind lidar along with radiosonde data (whenever available) has been used to assess the quality of the synergetic MLH estimates.

On non-synergetic SBLH estimation (obj. 2a). - Aerosol stratification under stable boundary-layer conditions has been successsfully related to the variance of the backscatter lidar signal. MVRs within temporal and spatial variance profiles have been shown to be key indicator of the presence of aerosol layers (fanning) in the atmosphere. A simplistic SBLH method consisting of the identification of the variance minima (in this Ph.D., it is called "threshold minima method") has been presented and applied to two test cases representative of different atmospheric conditions. It has been found that MVRs only exist under stable conditions in the boundary layer. The quality of SBLH estimates can largely be improved by an advanced adaptive estimation method such as the EKF.

The potentialities of EKF for the estimation SBLH have been shown. Thus, the height-resolved temporal variance profile of the lidar data has been used as the observables (or inputs) to the EKF along with an inverted Gaussian-like model for MVRs. The filter has been initialized by the SBLH estimate from a RS and it has been applied to Vaisala CT25K ceilometer data. Results have been compared with SBLH estimates from a collocated MWR and a good degree of agreement has been observed.

Finally, a method for the estimation of the SBLH from potential temperature profiles retrieved from MWR data has been presented. The method uses physically idealized models of the SBL temperature profile available in the literature. There are five models which include stable-mixed, mixed-linear, linear, polynomial and exponential. For a given temperature profile these five models have been fitted using the NLSQ approach. The best fitting model came up to be the exponential because it has given the mMSE.

Synergetic SBLH estimation (obj. 2b). - A synergetic approach for the estimation of SBLH using lidar and MWR data has been developed. Vertical variance of the backscatter signal from a ceilometer has been used as proxy of aerosols stratification in the nocturnal SBL. This hypothesis has been supported by a statistical analysis over one month of observations from HOPE campaign. Thermodynamic information from the MWR-derived potential temperature has been incorporated as coarse estimate of the SBLH. Data from the two instruments has been adaptively assimilated by using an EKF.

A first test of the algorithm has been performed by applying it to collocated Vaisala CT25K ceilometer and HATPRO MWR data. The method has successfully been applied to two test cases, one with a typical boundary layer development and another with complex nocturnal weakly stable boundary layer. The application of the synergetic algorithm to both atmospheric scenarios has revealed the superior performance of the EKF as compared to a NLSQ estimation, especially in non-ideal conditions.

On feasibility study on the usage of LES data for MLH estimation (obj. 3). - In this very prospective objective, LES has shown to be a promising tool for understanding the ABL. Comparison between LES-simulated and measured data has revealed good qualitative agreement in terms of both the magnitudes of the physical quantities (temperature, and backscatter) involved as well as the development of ABLH. Finally, as study case, a new method for *direct retrieval* of the MLH from simulated brightness measurements has been presented. Preliminary results indicate the potentiality of the method for operational use from MWR brightness temperature measurements.

7.2 Future lines

For in-depth understanding of the relative merits of the algorithms presented in this Ph.D. thesis, instrument simulators are to be combined with LES in order to follow boundary-layer development over the full diurnal cycle.

Using synthetic backscatter lidar profiles and brightness temperatures will allow further optimization of the algorithms to continuously derive the ABLH.

Validation and comparison between long-term simulated and measured data should be an essential step to ascertain the reliability and performance of the methods presented so far under different atmospheric conditions.

Finally, extensions of the methods for data from other sources such the radar, satellite-borne instruments, etc. is expected.

Appendix A

List of Publications

A.1 Journals

4. **Saeed, U.**, Rocadenbosch, F., “Variance processing for stable boundary-layer height estimation using backscatter lidar data: A discussion,” *IEEE Transactions on Geoscience and Remote Sensing.* (under prep.).

3. **Saeed, U.**, Rocadenbosch, F., “On the need of a synergetic mixing-layer height retrieval method using backscatter lidar returns and microwave-radiometer temperature observations,” *IEEE Transactions on Geoscience and Remote Sensing.* (Submitted, Feb. 2016).

2. **Saeed, U.**, Rocadenbosch, F., Crewell, S., “Adaptive Estimation of the Stable-Boundary-Layer Height Using Combined Lidar and Microwave Radiometer Observations,” *IEEE Transactions on Geoscience and Remote Sensing.* (Accepted with minor review).

1. Lange, D., Tiana-Alsina, J., **Saeed, U.**, Tomás, S., Rocadenbosch, F., “Atmospheric Boundary-Layer height monitoring using a Kalman filter and backscatter lidar,” *IEEE Transactions on Geoscience and Remote Sensing,* 52(8), 4717-4728 (2014).

A.2 International Conferences

9. **Saeed, U.**, Löhnert, U., Heus, T., Neggers, R., Rocadenbosch, F., and Crewell, S., “On the need of a direct retrieval method for mixing-layer height using simulated brightness temperature measurements,” *18th International Symposium for the Advancement of Boundary-Layer Remote Sensing (ISARS),* Varna, Bulgaria (2016). (Accepted).

8. **Saeed, U.**, Barragán, R., and Rocadenbosch, F., “Enhanced signal-to-noise ratio estimation for tropospheric lidar channels,” *EGU General Assembly 2016,* Vienna, Austria (2016).

7. **Saeed, U.**, Löhnert, U., Heus, T., Neggers, R., Rocadenbosch, F., and Crewell, S., "Can we retrieve mixing-layer height directly from the brightness temperature measurements?," *14th Specialist Meeting on Microwave Radiometry and Remote Sensing of the Environment (MicroRad 2016),* Helsinki, Finland (2016).

6. **Saeed, U.**, and Rocadenbosch, F., "Uncertainty on atmospheric boundary-layer height estimation due to measurement errors in the ground-based lidar and microwave radiometer data," *IEEE Young Professionals Conference,* Barcelona, Spain (2015).

5. **Saeed, U.**, Rocadenbosch, F., and Crewell, S., "Performance test of the synergetic use of simulated lidar and microwave radiometer observations for mixing-layer height detection," *Proc. of SPIE,* Toulouse, France (2015).

4. **Saeed, U.**, and Rocadenbosch, F., "Exploiting microwave radiometer-derived temperature profile structure for stable boundary-layer height estimation," *Proc. of SPIE,* Toulouse, France (2015).

3. **Saeed, U.**, Rocadenbosch, F., and Crewell, S., "Synergetic use of lidar and microwave radiometer observations for boundary-layer height detection," *Proc. of IEEE International Geoscience and Remote Sensing Symposium (IGARSS),* Milan, Italy (2015).

2. **Saeed, U.**, Rocadenbosch, F., and Crewell, S., "Adaptive estimation of the stable boundary-layer height using backscatter lidar data and a Kalman filter," *Proc. of IEEE International Geoscience and Remote Sensing Symposium (IGARSS),* Milan, Italy (2015).

1. **Saeed, U.**, Tiana-Alsina, J., Rocadenbosch, F., and Crewell, S., "Atmospheric boundary layer height estimation using combined microwave radiometer and lidar data," *The World Weather Open Science Conference (WWOSC),* Montreal, Canada, 16-21 August (2014)

Appendix B

Detailed derivative developments for Eq. 2.19

B.1 Direct contribution from ith layer, T_{B2}

First, consider the direct contribution with respect to changes in temperature only, in layer i

$$\begin{aligned}\frac{\partial T_{B2}}{\partial T} &= \frac{\partial}{\partial T}\left(\kappa(0,r)\int_{r}^{r+\Delta r} T(u)\alpha(u)\kappa(r,u)du\right), \\ &= \kappa(0,r)\int_{r}^{r+\Delta r} \alpha(u)\kappa(r,u)du. \end{aligned} \tag{B.1}$$

Second, the contribution due to changes in absorption coefficient, which is directly influenced by the changes in temperature, $\frac{\partial T_{B2}}{\partial \alpha}\frac{\partial \alpha}{\partial T}$, is given by

$$\frac{\partial T_{B2}}{\partial \alpha} = \kappa(0,r)\int_{r}^{r+\Delta r} T(u)\left[\kappa(r,u) + \alpha(u)\frac{\partial \kappa(r,u)}{\partial \alpha}\right]du, \tag{B.2}$$

where $\frac{\partial \kappa(r,u)}{\partial \alpha} = -\kappa(r,u)(u-r)$. Therefore,

$$\frac{\partial T_{B2}}{\partial \alpha} = \kappa(0,r)\int_{r}^{r+\Delta r} T(u)\left[\kappa(r,u) + \alpha(u)\kappa(r,u)(r-u)\right]du, \tag{B.3}$$

For the limiting case, $\Delta r \to 0$, $\Phi = r - u \to 0$, Eq. B.1 tends to

$$\frac{\partial T_{B2}}{\partial T} = \kappa(0,r)\alpha(r)\kappa(r,r)dr = \kappa(0,r)\alpha(r)dr, \tag{B.4}$$

and Eq. B.3 tends to

$$\frac{\partial T_{B2}}{\partial \alpha} = \kappa(0,r)T(r)dr. \tag{B.5}$$

By using Eq. B.4, and Eq. B.5, the total contribution directly from the ith layer then becomes

$$\begin{aligned}\frac{\partial T_{B2}}{\partial T} &= \frac{\partial T_{B2}}{\partial T} + \frac{\partial T_{B2}}{\partial \alpha}\frac{\partial \alpha}{\partial T}, \\ &= \left[\kappa(0,r)\alpha(r) + \kappa(0,r)T(r)\frac{\partial \alpha(r)}{\partial T}\right] dr. \end{aligned} \tag{B.6}$$

B.2 Contribution through the transmissivity term, $\kappa(0, r+\Delta r)$, in T_{B3}

The term for T_{B3} can be represented as

$$T_{B3} = \kappa(0, r+\Delta r) \int_{r+\Delta r}^{\infty} T(u)\alpha(u)\kappa(r+\Delta r, u)du, \tag{B.7}$$

and using the fact that $\frac{\partial T_{B3}}{\partial T} = \frac{\partial T_{B3}}{\partial \alpha}\frac{\partial \alpha}{\partial T}$ and that $\kappa(0, r+\Delta r) = \kappa(0,r)\kappa(r, r+\Delta r)$ in what follows:

Since only the term $\kappa(r, r+\Delta r)$ is affected by changes in ith layer

$$\frac{\partial T_{B3}}{\partial \alpha} = \frac{\partial T_{B3}}{\partial \kappa(r, r+\Delta r)}\frac{\partial \kappa(r, r+\Delta r)}{\partial \alpha}, \tag{B.8}$$

where

$$\frac{\partial T_{B3}}{\partial \kappa(r, r+\Delta r)} = \kappa(0,r) \int_{r+\Delta r}^{\infty} T(u)\alpha(u)\kappa(r+\Delta r, u)du, \tag{B.9}$$

and

$$\frac{\partial \kappa(r, r+\Delta r)}{\partial \alpha} = -\kappa(r, r+\Delta r)\Delta r. \tag{B.10}$$

Substituting Eq. B.9 and Eq. B.10 in Eq. B.8 and taking the limit $\Delta r \to 0$,

$$\begin{aligned}\frac{\partial T_{B3}}{\partial \alpha} &= \left[\kappa(0,r)\int_{r}^{\infty} T(u)\alpha(u)\kappa(r,u)du\right] \cdot \left[-(dr)\right] = \\ &= -\kappa(0,r)\left[\int_{r}^{\infty} T(u)\alpha(u)\kappa(r,u)du\right] dr. \end{aligned} \tag{B.11}$$

Total contribution from T_{B3} then becomes

$$\frac{\partial T_{B3}}{\partial T} = \frac{\partial T_{B3}}{\partial \alpha}\frac{\partial \alpha}{\partial T} = -\kappa(0,r)\left(\frac{\partial \alpha}{\partial T}\right)\left[\int_r^{\infty} T(u)\alpha(u)\kappa(r,u)du\right] dr. \tag{B.12}$$

B.3 Contribution through the background term , T_{B0}

The background term can be rewritten as

$$\begin{aligned} T_{B0} &= T_{BG}\kappa(0,\infty) = \\ &= T_{BG}\kappa(0,r)\kappa(r,r+\Delta r)\kappa(r+\Delta r,\infty). \end{aligned} \tag{B.13}$$

By taking the derivative with respect to changes in temperature in the ith layer,

$$\frac{\partial T_{B0}}{\partial T} = \frac{\partial T_{B0}}{\partial \alpha}\frac{\partial \alpha}{\partial T}. \tag{B.14}$$

The derivative $\frac{\partial T_{B0}}{\partial \alpha}$ is calculated from the term which is directly affected from the temperature changes in the ith layer at $(r, r+\Delta r)$,

$$\begin{aligned} \frac{\partial T_{B0}}{\partial \alpha} &= \frac{\partial}{\partial \alpha}\left[T_{BG}\kappa(0,r)\kappa(r+\Delta r,\infty)\kappa(r,r+\Delta r)\right], \\ &= T_{BG}\kappa(0,r)\kappa(r+\Delta r,\infty)\frac{\partial \kappa(r,r+\Delta r)}{\partial \alpha}, \end{aligned} \tag{B.15}$$

where $\frac{\partial \kappa(r,u)}{\partial \alpha} = -\kappa(r,u)(r-u)$ with $u = r+\Delta r$. Therefore, by substituting Eq. B.15 into Eq. B.14,

$$\begin{aligned} \frac{\partial T_{B0}}{\partial \alpha} &= T_{BG}\kappa(0,r)\kappa(r+\Delta r,\infty)\kappa(r,r+\Delta r)\Delta r \xrightarrow{\Delta r \to 0} \\ &\longrightarrow -T_{BG}\kappa(0,\infty)dr. \end{aligned} \tag{B.16}$$

B.4 Total contribution from the ith layer

The response of T_B with respect to perturbations in temperature in ith layer can be calculated by summing up the contributions from the above three terms, i.e., Eq. B.6, Eq. B.12, and Eq. B.16,

$$\begin{aligned}
d^2T_B(r) &= \left[\left(\frac{\partial T_{B,2}}{\partial T} + \frac{\partial T_{B,2}}{\partial \alpha}\frac{\partial \alpha}{\partial T}\right) + \left(\frac{\partial T_{B,3}}{\partial \alpha}\frac{\partial \alpha}{\partial T}\right) + \left(\frac{\partial T_{B,0}}{\partial \alpha}\frac{\partial \alpha}{\partial T}\right)\right] dT(r), \\
&= \Bigg[\kappa(0,r)\alpha(r) + \kappa(0,r)T(r)\frac{\partial \alpha(r)}{\partial T} - \kappa(0,\infty)T_{BG}\frac{\partial \alpha}{\partial T} - \\
&\kappa(0,r)\frac{\partial \alpha}{\partial T}\int_r^\infty T(u)\alpha(u)\kappa(r,u)du\Bigg] dT(r)dr. \qquad \text{(B.17)}
\end{aligned}$$

References

Angevine, W., Transitional, entraining, cloudy, and coastal boundary layers, *Acta Geophysica*, *56*(1), 2–20, 2008. 40

Angevine, W., H. Baltink, and F. Bosveld, Observations of the morning transition of the convective boundary layer, *Boundary-Layer Meteorology*, *101*(2), 209–227–, 2001. 40

Angevine, W. M., C. W. Hare, J. E.and Fairall, D. E. Wolfe, R. J. Hill, W. A. Brewer, and A. B. White, Structure and formation of the highly stable marine boundary layer over the Gulf of Maine, *Journal Of Geophysical Research*, *111*(D23S22), 1–13, doi: doi: 10.1029/2006JD007465, 2006. 69, 72, 90

Askne, J. I. H., and E. R. Westwater, A review of ground-based remote sensing of temperature and moisture by passive microwave radiometers, *IEEE Transactions on Geoscience and Remote Sensing*, *GE-24*, 340–352, 1986. 15, 31

Banks, R. F., S. Crewell, S. Henkel, and J. M. Baldasano, Training network for young atmospheric researchers, *Eos Transactions American Geophysical Union*, *97*, doi: 10.1029/2016EO045899, 2016. 2

Barlow, R., *Statistics: A Guide to the Use of Statistical Methods in The Physical Sciences*, chap. 4, Errors, pp. 48–67, Edited by F. Mandl, R. Ellison, and D. Sandiford, Wiley, Chichester, England, 1989a. 53, 57

Barlow, R., *Estimation, in Statistics: A Guide to the Use of Statistical Methods in The Physical Sciences*, Wiley, Chichester, England, chap. 5, pp. 68–95, 1989b. 93

Basili, P., P. Ciotti, and D. Solimini, Inversion of ground-based radiometric data by Kalman filtering, *Radio Science*, *16*, 83–91, 1981. 32

Basili, P., S. Bonafoni, P. Ciotti, F. S. Marzano, G. d'Auria, and N. Pierdicca, Retrieving atmospheric temperature profiles by microwave radiometry using a priori information on atmospheric spatial-temporal evolution, *IEEE Transactions on Geoscience and Remote Sensing*, *39*, 1896–1905, 2001. 32

Batchvarova, E., X. Cai, S.-E. Gryning, and D. Steyn, Modelling internal boundary-layer development in a region with a complex coastline, *Boundary-Layer Meteorology*, *90*(1), 1–20, doi: 10.1023/A:1001751219627, 1999. 40

Beer, A., Determination of the absorption of red light in colored liquids, *Annals of Physics*, *86*, 78–88, doi: doi:10.1002/andp.18521620505, 1852. 17

Boers, R., and E. W. Eloranta, Lidar measurements of the atmospheric entrainment zone and the potential temperature jump across the top of the mixed layer, *Bound.-Layer Meteor.*, *34*, 357–375, 1986. 51

Bradley, R. S., F. T. Keimig, and H. F. Diaz, Recent changes in the North American Arctic boundary layer in winter, *J. Geophys. Res.*, *98*(D5), 8851–8858, 1993. 72, 100

Brown, R. G., and P. Y. C. Hwang, *Introduction to Random Signals and Applied Kalman Filtering*, chap. 2, Mathematical Description of Random Signals, pp. 72–127, John Wiley & Sons, Inc., 1997. 78

Cadeddu, M. P., V. H. Payne, S. A. Clough, K. Cady-Pereira, and J. C. Liljegren, Effect of the oxygen line-parameter modeling on temperature and humidity retrievals from ground-based microwave radiometers, *IEEE Transactions on Geoscience and Remote Sensing*, *45*, 2216–2223, 2007. 26, 38

Chan, P. W., The use of neural network retrieval for thermodynamic profiles of a ground-based microwave radiometer, in *The 11th Specialist Meeting on Microwave Radiometry and Remote Sensing of the Environment, Washington, DC, USA*, 2010. 32

Chandrasekhar, S., *Radioactive Transfer*, The International Series of Monographs on Physics, Oxford, At the Clarendon Press, 1950. 14

Chang, A., Microwave remote sensing of atmospheric parameters: Modelling and retrieval, *Journal of Photogrammetry and Remote Sensing*, *6*, 1–20, 2001. 29, 30

Churnside, J. H., T. A. Stermitz, and J. A. Schroeder, Temperature profiling with neural network inversion of microwave radiometer data, *Journal of Atmospheric and Oceanic Technology*, *11*, 105ÂŰ109, 1994. 32

Cimini, D., T. J. Hewison, L. Martin, J. Güldner, C. Gaffard, and F. S. Marzano, Temperature and humidity profile retrievals from ground-based microwave radiometers during tuc, *Meteorologische Zeitschrift*, *15*(1), 45–56, doi: 10.1127/0941-2948/2006/0099, 2006. 32

Cimini, D., F. S. Marzano, and G. Visconti (Eds.), *Integrated Ground-Based Observing Systems*, chap. I-3, Principles of Aerosol LIDAR Systems, pp. 59–88, Springer-Verlag Berlin Heidelberg, 2010a. 16

Cimini, D., E. R. Westwater, and A. J. Gasiewski, Temperature and humidity profiling in the arctic using ground-based millimeter-wave radiometry and 1DVAR, *IEEE Transactions on Geoscience and Remote Sensing*, *48*, 1381–1388, 2010b. 31

Cimini, D., E. Campos, R. Ware, S. Albers, G. Giuliani, J. Oreamuno, S. E. Koch, S. Cober, and E. R. Westwater, Temperature and humidity profiling in the arctic using ground-based millimeter-wave radiometry and 1DVAR, *IEEE Transactions on Geoscience and Remote Sensing*, *49*, 4959–4969, 2011. 31

Cimini, D., F. De Angelis, J.-C. Dupont, S. Pal, and M. Haeffelin, Mixing layer height retrievals by multichannel microwave radiometer observations, *Atmospheric Measurement Techniques*, *6*, 4971–4998, 2013. 32, 49

Clough, S., M. Shephard, E. Mlawer, J. Delamere, M. Iacono, K. Cady-Pereira, S. Boukabara, and P. Brown, Atmospheric radiative transfer modeling: a summary of the AER codes, *Journal of Quantitative Spectroscopy and Radiative Transfer*, *91*, 233–244, 2004. 26

Cohn, S. A., and W. M. Angevine, Boundary layer height and entrainment zone thickness measured by lidars and wind-profiling radars, *Journal of Applied Meteorology*, *39*(8), 1233–1247, doi: 10.1175/1520-0450(2000)039<1233:BLHAEZ>2.0.CO;2, 2000. 42, 47

Collaud Coen, M., C. Praz, A. Haefele, D. Ruffieux, P. Kaufmann, and B. Calpini, Determination and climatology of the planetary boundary layer height above the Swiss plateau by in situ and remote sensing measurements as well as by the COSMO-2 model, *Atmos. Chem. Phys.*, *14*(23), 13,205–13,221, 2014. 46, 72, 84, 90, 100

Collis, R., and P. Russell, *Laser Monitoring of the Atmosphere*, chap. 12, Lidar Measurement of Particles and Gases by Elastic Backscattering and Differential Absorption, pp. 71–102, Edited by E.D. Hinkley, Springer-Verlag, New York, 1976. 17, 19

Crewell, S., and U. Löhnert, Accuracy of cloud liquid water path from ground-based microwave radiometry - Part I: Sensor accuracy and synergy, *Radio Sci.*, *38*(3), 7–1–7–11, 2003. 50

Crewell, S., and U. Löhnert, Accuracy of boundary layer temperature profiles retrieved with multifrequency multiangle microwave radiometry, *IEEE Transactions on Geoscience and Remote Sensing*, *45*, 2195–2201, 2007. 31, 32, 51, 55, 90, 100

Crewell, S., H. Czekala, U. Löhnert, T. Rose, C. Simmer, R. Zimmermann, and R. Zimmermann, Microwave radiometer for cloud carthography: A 22-channel ground-based microwave radiometer for atmospheric research, *Radio Science*, *36*, 621–638, 2001. 15, 32, 38

Cuxart, J., A. Holtslag, R. Beare, E. Bazile, A. Beljaars, A. Cheng, L. Conangla, M. Ek, F. Freedman, R. Hamdi, A. Kerstein, H. Kitagawa, G. Lenderink, D. Lewellen, J. Mailhot, T. Mauritsen, V. Perov, G. Schayes, G.-J. Steeneveld, G. Svensson, P. Taylor, W. Weng, S. Wunsch, and K.-M. Xu, Single-column model intercomparison for a stably stratified atmospheric boundary layer, *Boundary-Layer Meteorology*, *118*(2), 273–303, doi: 10.1007/s10546-005-3780-1, 2006. 70

Emeis, S., *Surface-based Remote Sensing of the Atmospheric Boundary Layer*, 978-90-481-9339-4, Springer, 2010. 3, 13, 17

Emeis, S., K. Schäfer, and C. Münkel, Surface-based remote sensing of the mixing-layer height: a review, *Meteorol Z*, *17*, 621–630, 2008. 14

Endlich, R., F. Ludwig, and E. Uthe, An automatic method for determining the mixing depth from lidar observations, *Atmospheric Environment*, *13*, 1051–1056, 1967. 51

Eresmaa, N., A. Karppinen, S. M. Joffre, J. Räsänen, and H. Talvitie, Mixing height determination by ceilometer, *Atmos. Chem. Phys*, *6*, 1485–1493, 2006. 20, 89, 90

Eriksson, P., S. Buehler, C. Davis, C. Emde, and O. Lemke, Arts, the atmospheric radiative transfer simulator, version 2, *Journal of Quantitative Spectroscopy and Radiative Transfer*, *112*, 1551–1558, 2011. 26

Fisher, B., and D. Thomson, Harmonization in the preprocessing of meteorological data for atmospheric dispersion models, *Final Report COST710*, COST Action 710, 1998. 47

Flamant, C., J. Pelon, P. H. Flamant, and P. Durand, Lidar determination of the entrainment zone thickness at the top of the unstable marine atmospheric boundary-layer, *Bound.-Layer Meteor.*, *83*, 247–284, 1997. 42, 51

Frate, F. D., and G. Schiavon, A combined natural orthogonal functions/neural network technique for the radiometric estimation of atmospheric profiles, *Radio Science*, *33*, 405–410, 1998. 32

Garratt, J., *The atmospheric boundary layer*, Cambridge university press, 1992. 46

Giuseppe, F., A. Riccio, L. Caporaso, G. Bonafé, G. Gobbi, and F. Angelini, Automatic detection of atmospheric boundary layer height using ceilometer backscatter data assisted by a boundary layer model, *Quarterly Journal of the Royal Meteorological Society*, *138*, 649–663, 2012. 90

Güldner, J., and D. Spänkuch, Remote sensing of the thermodynamic state of the atmospheric boundary layer by ground-based microwave radiometry, *Journal of Atmospheric and Oceanic Technology*, *18*, 925–933, 2001. 31, 32

Haeffelin, M., F. Angelini, Y. Morille, G. Martucci, S. Frey, G. Gobbi, S. Lolli, C. O'Dowd, L. Sauvage, I. Xueref-Rémy, B. Wastine, and D. Feist, Evaluation of mixing-height retrievals from automatic profiling lidars and ceilometers in view of future integrated networks in Europe, *Boundary-Layer Meteorology*, *143*, 49–75, 2012. 14, 47, 49, 89, 90

Haij, M. d., W. Wauben, and H. Baltink, Continuous mixing layer height determination using the LD-40 ceilometer: a feasibility study, *Technical report*, Royal Netherlands Meteorological Institute (KNMI), 2007. 90

Han, Y., and E. R. Westwater, Applications of Kalman filtering to derive water vapor profiles from raman lidar and microwave radiometers, *Journal of Atmospheric and Oceanic Technology*, *14*, 480–487, 1997. 32

Han, Y., and E. R. Westwater, Analysis and improvement of tipping calibration for ground-based microwave radiometers, *IEEE Transactions on Geoscience and Remote Sensing*, *38*, 1260–1276, 2000. 38

Hanna, G., J. Roumeliotis, and A. Kucera, Collocation and fredholm integral equations of the first kind, *Journal of Inequalities in Pure and Applied Mathematics*, *6*, 1–8, 2005. 23

Hennemuth, B., and A. Lammert, Determination of the atmospheric boundary layer height from radiosonde and lidar backscatter, *Boundary-Layer Meteorology*, *120*, 181–200, 2006. 41, 90

Heus, T., Formulation of the Dutch Atmospheric Large-Eddy Simulation (DALES) and overview of its applications, *Geoscientific Model Development*, *3*(2), 415–444, 2010. 109

Hewison, T., 1D-VAR retrieval of temperature and humidity profiles from a ground-based microwave radiometer, *IEEE Transactions on Geoscience and Remote Sensing*, *45*, 2163–2168, 2007. 31

Hewison, T. J., Profiling temperature and humidity by ground-based microwave radiometers, *Phd thesis*, Department of Meteorology, University of Reading, 2006. xv, 14, 26, 31, 38

Hewison, T. J., and C. Gaffard, Combining data from ground-based microwave radiometers and other instruments in temperature and humidity profile retrieval, in *TECO-2006 - WMO Technical Conference on Meteorological and Environmental Instruments and Methods of Observation*, 2006. 31

Hoff, R., R. Hardesty, F. Carr, T. Weckwerth, S. Koch, A. Benedetti, S. Crewell, D. Cimini, D. Turner, W. Feltz, B. Demoz, V. Wulfmeyer, D. Sisterson, T. Ackerman, F. Fabry, and K. Knupp, Thermodynamic profiling technologies workshop report, *Tech. rep.*, National Science Foundation and the National Weather Service, 2012. 46

Hogg, D. C., M. T. Decker, F. O. Guiraud, K. B. Earnshaw, D. A. Merritt, K. P. Moran, W. B. Sweezy, R. G. Strauch, E. R. Westwater, and C. G. Little, An automatic profiler of the temperature, wind and humidity in the troposphere, *Climate and Applied Meteorology*, *22*, 807–831, 1983. 31

Holzworth, G., Estimates of mean maximum mixing depths in the contiguous United States, *Monthly Weather Review*, *92*, 235–242, 1964. 44, 47, 49, 53

Hooper, W. P., and E. W. Eloranta, Lidar measurements of wind in the planetary boundaryndary layer: The method, accuracy and results from joint measurements with radiosonde and Kytoon, *J. Climate Appl. Meteor.*, *25*, 990–100, 1986. 42, 47, 51, 90

Hyun, Y.-K., K.-E. Kim, and K.-J. Ha, A comparison of methods to estimate the height of stable boundary layer over a temperate grassland, *Agricultural and Forest Meteorology*, *132*(2005), 132–142, 2005. 69, 90

Illingworth, A., D. Ruffieux, D. Cimini, U. Löhnert, M. Haffelin, and V. Lehmann, Final report, *Tech. rep.*, COST Action ES0702 EG-CLIMET, doi: 10.12898/ES0702FR, 2013. 22, 46

Janssen, M. A., *Atmospheric Remote Sensing by Microwave Radiometry*, John Wiley & Sons, Third Avenue, New York, NY, 1993. xv, 14, 15, 21, 23, 25, 26, 27, 29, 30, 35, 38

Jenoptik, Jenoptik CHM 15k NIMBUS, *Technical specifications*, Jenoptik, 2013. xix, 9

Jeričević, A., and B. Grisogono, The critical bulk Richardson number in urban areas: verification and application in a numerical weather prediction model, *Tellus A*, *58*, 19–27, 2006. 46, 47

Kadygrov, E. N., and D. R. Pick, The potential for temperature retrieval from an angular-scanning single-channel microwave radiometer and some comparisons with in situ observations., *Meteorological Applications*, *5*, 393–404, 1998. 30

Kumar, D., Concept design, analysis, and integration of the new UPC multispectral lidar system, Doctoral thesis, Thesis advisor: Dr. F. Rocadenbosch, Universitat Politècnica de Catalunya (UPC), 2012. 3, 15

Lange, D., Lidar and s-band radar profiling of the atmosphere: Adaptive processing for boundary-layer monitoring, optical-parameter error estimation, and application cases, Doctoral thesis, Thesis advisor: Dr. F. Rocadenbosch, Universitat Politècnica de Catalunya (UPC), 2014. 3, 15, 17, 42, 43

Lange, D., J. Tiana-Alsina, U. Saeed, S. Tomás, and F. Rocadenbosch, Atmospheric-boundary-layer height monitoring using a Kalman filter and backscatter lidar returns, *IEEE Transactions on Geoscience and Remote Sensing*, *52*(8), 4717–4728, doi: 10.1109/TGRS.2013.2284110, 2014. 4, 14, 20, 32, 40, 42, 44, 47, 49, 50, 52

Lange, D., F. Rocadenbosch, J. Tiana-Alsina, and S. Frasier, Atmospheric boundary-layer-height estimation using a Kalman filter and a frequency-modulated continuous-wave radar returns, *IEEE Transactions on Geoscience and Remote Sensing*, *53*(6), 3338–3349, doi: 10.1109/TGRS.2014.2374233, 2015. 52

Ledsham, W. H., and D. H. Staelin, An extended Kalman-Bucy filter for atmospheric temperature profile retrieval with a passive microwave sounder, *American Meteorological Society*, *17*, 1023–1033, 1978. 32

Lenoble, J., M. I. Mishchenko, and M. Herman, *Aerosol Remote Sensing*, chap. 2, Absorption and scattering by molecules and particles, pp. 13–51, Springer-Verlag Berlin Heidelberg, 2013. 17

Liebe, H., MPM - an atmospheric millimeter-wave propagation model, *International Journal of Infrared and Millimeter Waves*, *10*, 631–650, 1989. 26

Liebe, H. J., G. A. Hufford, and M. G. Cotton, Propagation modeling of moist air and suspended water/ice particles at frequencies below 1000 GHz, in *AGARD, Atmospheric Propagation Effects Through Natural and Man-Made Obscurants for Visible to MM-Wave Radiation*, vol. 3, pp. 1–11, 1993. 26

Liljegren, J. C., S. A. Boukabara, K. Cady-Pereira, and S. A. Clough, The effect of the half-width of the 22-GHz water vapor line on retrievals of temperature and water vapor profiles with a twelve-channel microwave radiometer, *Special Issue of the IEEE Transactions on Geoscience and Remote Sesing*, *X*, 1–5, 2004. 31

Liu, S., and X. Liang, Observed diurnal cycle climatology of planetary boundary layer height, *J. Climate*, *23*, 5790–5809, 2010. 72

Löhnert, U., and S. Crewell, Accuracy of cloud liquid water path from ground-based microwave radiometry - Part I: Dependency on cloud model statistics and precipitation, *Radio Science*, *38*, 6.1–6.11, doi: DOI:10.1029/2002RS002654, 2003. 50

Löhnert, U., and O. Maier, Operational profiling of temperature using ground-based microwave radiometry at Payerne: Prospects and challenges, *Atmos. Meas. Tech.*, *5*(5), 1121–1134, 2012. 10, 32, 51, 55, 100

Löhnert, U., S. Crewell, and C. Simmer, An integrated approach toward retrieving physically consistent profiles of temperature, humidity, and cloud liquid water, *Applied Meteorology*, *43*, 1295–1307, 2004. 31

Löhnert, U., S. Crewell, O. Krasnov, E. O'Connor, and H. Russchenberg, Advances in continuously profiling the thermodynamic state of the boundary layer: Integration of measurements and methods, *Atmospheric and Oceanic Technologies*, *25*, 1251–1266, 2008. 31

Löhnert, U., D. Turner, and S. Crewell, Ground-based temperature and humidity profiling using spectral infrared and microwave observations. Part I: Simulated retrieval performance in clear-sky conditions, *Applied Meteorology and Climatology*, *48*, 1017–1032, 2009. 31, 32, 55

Löhnert, U., J. H. Schween, C. Acquistapace, K. Ebell, M. Maahn, M. Barrera-Verdejo, A. Hirsikko, B. Bohn, A. Knaps, E. O'Connor, C. Simmer, A. Wahner, and S. Crewell, JOYCE: Jülich Observatory for Cloud Evolution, *Bull. Amer. Meteor. Soc.*, *96*(7), 1157–1174, doi: 10.1175/BAMS-D-14-00105.1, 2015. 7, 8, 11

Martucci, G., V. Mitev, R. Matthey, and M. Srivastava, Remote-controlled automatic backscatter lidar for PBL and troposphere measurements: description and first results, in *Proc. SPIE, Remote Sensing of Clouds and the Atmosphere VIII*, vol. 5235, pp. 661–672, 2004. 41, 47

Maschwitz, G., U. Löhnert, S. Crewell, T. Rose, and D. D. Turner, Investigation of ground-based microwave radiometer calibration techniques at 530 hpa, *Atmospheric Measurement Techniques Discussions*, *6*, 989–1032, 2013. 38

Mattioli, V., E. Fionda, P. Ciotti, S. Crewell, U. Löhnert, D. Cimini, and F. Marzano, Handbook of measurements, *Report Ref321994003*, COST, 2013. 21, 23

McGarragh, G., X radiative transfer model, `http://reef.atmos.colostate.edu/~gregm/xrtm/doc/xrtm.pdf`, 2012. 26

Measure, E. M., Y. P. Yee, and J. M. Balding, Inverting radiometric measurements with a neural network, in *AGARD Conference Proceedings: Remote Sensing of the Propagation Environment (SEE N92-22790 13-46)*, vol. 502, pp. 30–1–30–6, 1992. 32

Measures, R. M., *Laser Remote Sensing: Fundamentals and Applications*, chap. 7, Laser-Remote Sensor Equations, pp. 237–280, Krieger, Malabar, FL USA, 1992. 20, 50

Melfi, S. H., J. D. Spinhirne, S.-H. Chou, and S. P. Palm, Lidar observations of vertically organized convection in the planetary boundary layer over the ocean, *J. Climate Appl. Meteor.*, *24*, 806–821, 1985. 40, 47, 51, 60

Menut, L., C. Flamant, J. Pelon, and P. H. Flamant, Urban boundary-layer height determination from lidar measurements over the paris area, *Appl. Opt.*, *38*, 945–954, 1999. 42, 51

Meunier, V., U. Löhnert, P. Kollias, and S. Crewell, Biases caused by the instrument bandwidth and beam width on simulated brightness temperature measurements from scanning microwave radiometers, *Atmospheric Measurement Techniques*, *6*, 1171–1187, 2013. 38

Moré, J. J., The levenberg-marquardt algorithm: Implementation and theory, *Numerical Analysis*, pp. 105–116, lecture Notes in Mathematics. Berlin, Germany: Springer-Verlag, 1977. 99

Morille, Y., M. Haeffelin, P. Drobinski, and J. Pelon, Strat: An automated algorithm to retrieve the vertical structure of the atmosphere from single-channel lidar data, *J. Atmos. Oceanic Technol.*, *24*(5), 761–775, doi: 10.1175/JTECH2008.1, 2007. 42, 47

Muenkel, C., S. Emeis, W. J. Mueller, and K. P. Schaefer, Aerosol concentration measurements with a lidar ceilometer: results of a one year measuring campaign, in *SPIE, Remote Sensing of Clouds and the Atmosphere VIII,*, vol. 5235, pp. 486–496, doi: 10.1117/12.511104, 2004. 15

Münkel, C., N. Eresmaa, J. Räsänen, and A. Karppinen, Retrieval of mixing height and dust concentration with lidar ceilometer, *Boundary-Layer Meteorology*, *124*(1), 117–128, 2007. 16, 17, 20, 90, 91

Neggers, R. A. J., A. P. Siebesma, and T. Heus, Continuous single-column model evaluation at a permanent meteorological supersite, *Amer. Meteor. Soc.*, *93*, 1389ÂŰ1400, 2012. 109

Nyquist, H., Thermal agitation of electric charge in conductors, *Physical Review*, *32*, 110–113, 1928a. 35

Nyquist, J. B., Thermal agitation of electricity in conductors, *Physical Review*, *32*, 97–109, 1928b. 35

Pandolfi, M., G. Martucci, X. Querol, A. Alastuey, F. Wilsenack, S. Frey, C. D. O'Dowd, and M. Dall'Osto, Continuous atmospheric boundary layer observations in the coastal urban area of Barcelona during SAPUSS, *Atmospheric Chemistry and Physics*, *13*, 4983–4996, 2013. 14, 20

Pearson, G., F. Davies, and C. Collier, Remote sensing of the tropical rain forest boundary layer using pulsed doppler lidar, *Atmos. Chem. Phys.*, *10*(13), 5891–5901, 2010. 11

Pearson, G. N., and C. G. Collier, A pulsed coherent CO2 lidar for boundary-layer meteorology, *Quarterly Journal of the Royal Meteorological Society*, *125*(559), 2703–2721, doi: 10.1002/qj.49712555918, 1999. 11

Planck, M., and M. Masius, *The Theory of Heat Radiation*, P. Blakiston's Son & Co., Philadelphia, 1012 Walnut Street, 1914. 14

Praz, C., Automatic planetary boundary layer detection : validation of various detection instruments and methods, comparison with the forecast model cosmo-2 and one-year climatology, *Internship report*, MeteoSwiss-EPFL, 2013. 47

Qiang, Z., and W. Sheng, A study of the atmospheric boundary layer structure during a clear day in the arid region of Northwest China, *Acta Meteor. Sinica*, *23*(3), 327–337, 2009. 69

Reba, M., Data processing and inversion interfacing the UPC elastic-raman lidar system, Doctoral thesis, Advisor: F. Rocadenbosch, Universitat Politècnica de Catalunya (UPC), 2010. 3

Rocadenbosch, F., A. Comerón, and D. Pineda, Assessment of lidar inversion errors for homogeneous atmospheres, *Appl. Opt.*, *37*(12), 2199–2206, doi: 10.1364/AO.37.002199, 1998a. 53

Rocadenbosch, F., G. Vázquez, and A. Comerón, Adaptive filter solution for processing lidar returns: Optical parameter estimation, *Applied Optics*, *37*, 7019–7034, 1998b. 32, 52

Rocadenbosch, F., C. Soriano, A. Comerón, and J. Baldasano, Lidar inversion of atmospheric backscatter and extinction-to-backscatter ratios by use of a Kalman filter., *Applied Optics*, *38*, 3175–3189, 1999. 32, 50, 52

Rocadenbosch, F., S. Frasier, D. Kumar, D. Vega, E. Gregorio, and M. Sicard, Backscatter error bounds for the elastic lidar two-component inversion algorithm, *IEEE Transactions on Geoscience and Remote Sensing*, pp. 4791–4803, 2012. 57

Rodger, C. D., *Inverse Methods for Atmospheric Sounding: Theory and Practice*, World Scientific Publishing Co. Pte. Ltd., 2000. 26, 31, 114

Rose, T., S. Crewell, U. Löhnert, and C. Simmer, A network suitable microwave radiometer for operational monitoring of the cloudy atmosphere, *Atmospheric Research*, *75*, 183–200, 2005. 4, 8

Rosenkranz, P. W., Water vapor microwave continuum absorption: A comparison of measurements and models, *Radio Science*, *33*, 919–928, 1998. 26

RPG, Technical instrument manual, `http://www.radiometer-physics.de/rpg/html/docs/RPG_MWR_STD_Technical_Manual.pdf`, 2011. xv, xix, 11, 33, 34

Rybicki, G. B., and A. P. Lightman, *Radiative Processes in Astrophysics*, Wiley-VCH, 2004. 14

Saeed, U., and F. Rocadenbosch, Exploiting the structure of MWR-derived temperature profile for stable boundary-layer height estimation, in *Proc. SPIE*, vol. 9640 (16), pp. 1–8, 2015. 69

Saeed, U., and F. Rocadenbosch, On the need of a synergetic mixing-layer height retrieval method using backscatter lidar returns and microwave-radiometer temperature observations, *IEEE Transactions on Geoscience and Remote Sensing.*, under review (submitted, Feb. 2016), 2016a. 49

Saeed, U., and F. Rocadenbosch, Variance processing for stable boundary-layer height estimation using backscatter lidar data: A discussion, *IEEE Transactions on Geoscience and Remote Sensing.*, in preparation, 2016b. 69

Saeed, U., F. Rocadenbosch, and S. Crewell, Adaptive estimation of the stable boundary-layer height using backscatter lidar data and a Kalman filter, in *Proc. IEEE International Geoscience and Remote Sensing Symposium (IGARSS)*, pp. 3591 – 3594, Milan (Italy), (Accepted), 2015a. 69

Saeed, U., F. Rocadenbosch, and S. Crewell, Performance test of the synergetic use of simulated lidar and microwave radiometer observations for mixing-layer height detection, in *Proc. SPIE*, vol. 9640 (08), pp. 1–10, 2015b. 49

Saeed, U., U. Löhnert, T. Heus, R. Neggers, F. Rocadenbosch, and S. Crewell, Can we retrieve mixing-layer height directly from the brightness temperature measurements?, in *14th Specialist Meeting on Microwave Radiometry and Remote Sensing of the Environment (MicroRad)*, 2016a. 109

Saeed, U., F. Rocadenbosch, and S. Crewell, Adaptive estimation of the stable-boundary-layer height using combined lidar and microwave radiometer observations, *IEEE Transactions on Geoscience and Remote Sensing.*, 2016b. 89

Schneebeli, M., and C. Mätzler, A calibration scheme for microwave radiometers using tipping curves and kalman filtering, *IEEE Transactions on Geoscience and Remote Sensing*, *47*, 4201–4209, 2009. 38

Schween, J. H., A. Hirsikko, U. Löhnert, and S. Crewell, Mixing-layer height retrieval with ceilometer and doppler lidar: from case studies to long-term assessment, *Atmos. Meas. Tech.*, *7*(11), 3685–3704, 2014. 7, 8, 11, 15, 64

Seibert, P., F. Beyrich, S.-E. Gryning, S. Joffre, A. Rasmussen, and P. Tercier, Review and intercomparison of operational methods for the determination of the mixing height, *Atmospheric Environment*, *34*, 1352–2310, 2000. 13, 39, 40, 46

Seidel, D., Y. Zhang, A. Beljaars, J.-C. Golaz, A. Jacobson, and B. Medeiros, Climatology of the planetary boundary layer over the continental United States and Europe, *Journal Of Geophysical Research*, *117*(D17106), 1–15, 2012. 70

Solheim, F., J. Godwin, E. Westwater, Y. Han, S. Keihm, K. Marsh, and R. Ware, Radiometric profiling of temperature, water vapor and cloud liquid water using various inversion methods, *Radio Science*, *33*, 393–404, 1998. 29, 32

Stähli, O., A. Murk, N. Kämpfer, C. Mätzler, and P. Eriksson, Microwave radiometer to retrieve temperature profiles from the surface to the stratopause, *Atmospheric Measurement Techniques*, *6*, 2477–2494, 2013. 31

Steeneveld, G. J., B. J. H. Van de Wiel, and A. A. M. Holtslag, Modelling the evolution of the nocturnal boundary layer for three different nights in cases-99, in *In Proceedings of 16th Symposium on Boundary Layers and Turbulence*, 2004. 69

Steinke, S., S. Eikenberg, U. Löhnert, G. Dick, D. Klocke, P. Di Girolamo, and S. Crewell, Assessment of small-scale integrated water vapour variability during HOPE, *Atmos. Chem. Phys.*, *15*(5), 2675–2692, 2015. 11

Steyn, D. G., M. Baldi, and R. M. Hoff, The detection of mixed layer depth and entrainment zone thickness from lidar backscatter profiles, *J. Atmos. Oceanic Technol.*, *16*(7), 953–959, doi: 10.1175/1520-0426, 1999. 42

Stull, R. B., *An Introduction to Boundary Layer Meteorology*, chap. 12, Stable Boundary Layer, pp. 499–543, Springer Netherlands, 1988. xvi, 3, 13, 14, 39, 46, 69, 72, 73, 82, 84, 90, 100, 107

Szintai, B., Improving the turbulence coupling between high resolution numerical weather prediction models and lagrangian particle dispersion models, *Phd thesis*, Swiss Federal Institute of Technology, 2010. 47

Tan, H., J. Mao, H. Chen, P. W. Chan, D. Wu, F. Li, and T. Deng, A study of a retrieval method for temperature and humidity profiles from microwave radiometer observations based on principal component analysis and stepwise regression, *Journal of Atmospheric and Oceanic Technology*, *28*, 378–389, 2010. 32

Troitsky, A., K. Gajkovich, V. Gromov, E. Kadygrov, and A. Kosov, Thermal sounding of the atmospheric boundary layer in the oxygen absorption band center at 60 GHz, *IEEE Transactions on Geoscience and Remote Sensing*, *31*, 116–120, 1993. 32

Trokhimovski, Y., E. Westwater, Y. Han, and V. Leuski, Air and sea surface temperature measurements using a 60-GHz microwave rotating radiometer, *IEEE Transactions on Geoscience and Remote Sensing*, *36*, 3–15, 1998. 32

Turner, C. S., Johnson-nyquist noise, *Tech. Rep. V1.5*, Wireless Systems Engineering, Inc., 2007. 35

Ulaby, F. T., R. K. Moore, and A. K. Fung, *Microwave Remote Sensing: Active and Passive*, vol. 1, Addison-Wesley Publishing Company, The Artech House Remote Sensing Library, 1981. xv, 14, 15, 21, 22, 35

Ulaby, F. T., R. K. Moore, and A. K. Fung, *Microwave Remote Sensing: Active and Passive*, vol. 1, Addison-Wesley Publishing Company, The Artech House Remote Sensing Library, 1986. xv, 25, 26, 27, 28, 29, 30

Velez-Reyes, M., Atmospheric retrievals using regularization methods, in *IEEE International Geoscience and Remote Sensing Symposium Proceedings*, vol. 3, pp. 1403–1407, 1998. 29

Wallace, J. M., and P. V. Hobbs, *Atmospheric Science: An Introductory Survey*, Elsevier, 2006. 53

Wang, Z., X. Cao, L. Zhang, J. Notholt, B. Zhou, R. Liu, and B. Zhang, Lidar measurement of planetary boundary layer height and comparison with microwave profiling radiometer observation, *Atmospheric Measurement Techniques*, *5*, 1965–1972, 2012. 64

Ware, R., R. Carpenter, J. Güldner, J. Liljegren, T. Nehrkorn, F. Solheim, and F. Vandenberghe, A multichannel radiometric profiler of temperature, humidity, and cloud liquid, *Radio Science*, *38*, 1–13, 2003. 32

Westwater, E. R., and N. C. Grody, Combined surface- and satellite-based microwave temperature profile retrieval, *J. Appl. Meteor.*, *19*(12), 1438–1444, doi: 10.1175/1520-0450(1980)019<1438:CSASBM>2.0.CO;2, 1980. 28

Westwater, E. R., Y. Han, V. G. Irisov, V. Leuskiy, E. N. Kadygrov, and S. A. Viazankin, Remote sensing of boundary layer temperature profiles by a scanning 5-mm microwave radiometer and RASS: Comparison experiments, *Journal of Atmospheric and Oceanic Technology*, *16*, 805–818, 1999. 32

Wiegner, M., and A. Geiß, Aerosol profiling with the jenoptik ceilometer chm15kx, *Atmos. Meas. Tech.*, *5*(8), 1953–1964, 2012. 15